UNIVERSITÉ PARIS XIII - SORBONNE PARIS NORD

École Doctorale Sciences, Technologies, Santé Galilée

UNIVERSITÉ SIDI MOHAMED BEN ABDELLAH

Centres d'Études Doctorales Sciences et Technologies

Étude théorique et numérique des écoulements de Bingham

THÈSE DE DOCTORAT

présentée par

Wassim Aboussi

Laboratoire Analyse, Géométrie et Applications

Laboratoire Analyse Mathématique et Applications

pour l'obtention du grade de

DOCTEUR EN MATHÉMATIQUES APPLIQUÉES

Soutenue le 26 juin 2024 devant le jury d'examen composé de :

Fatima Ezzaki	PES, Université Sidi Mohamed Ben Abdellah	Présidente
Rémi Abgrall	PES, Université de Zurich	Rapporteur
François Bouchut	DR, CNRS & Université Gustave Eiffel	Rapporteur
Hassania Hamzaoui	PES, Université Sidi Mohamed Ben Abdellah	Rapportrice
Ahmed Aberqi	PH, Université Sidi Mohamed Ben Abdellah	Examinateur/Co-encadrant
Claire Chainais-Hillairet	PES, Université Lille 1	Examinatrice
Fayssal Benkhaldoun	PES, Université Sorbonne Paris Nord	Directeur de thèse
Jaouad Bennouna	PES, Université Sidi Mohamed Ben Abdellah	Directeur de thèse
Imad Kissami	PA, Université Mohammed VI Polytechnique	Invité/Co-encadrant
Emmanuel Audusse	PH, Université Sorbonne Paris Nord	Invité
Mohammed Boubekeur	IR, CNRS & Université Sorbonne Paris Nord	Invité

À l'âme de mon ami Soufiane Sadouioui
À ma famille

Remerciements

Je tiens à exprimer ma plus profonde gratitude à mes directeurs de thèse, Fayssal Benkhaldoun et Jaouad Bennouna. Leurs précieux conseils, leurs commentaires constructifs et leur soutien permanent ont été essentiels à la réussite de cette belle aventure, amorcée pendant mon stage de master. Alors que la pandémie de COVID-19 occupait tous les esprits, Fayssal et moi avons trouvé refuge sur Discord, plongés dans des discussions passionnées sur les mathématiques et les méthodes numériques. La confiance et les suggestions de Jaouad ont grandement influencé le développement de cette thèse. Je présente également mes remerciements à Imad Kissami, Ahmed Aberqi et Abdallah Bradji pour leur expertise, leurs conseils et orientations.

Je remercie sincèrement Rémi Abgrall, François Bouchut et Hassania Hamzaoui qui m'ont honoré en acceptant de rapporter cette thèse. Mes remerciements vont également à Fatima Ezzaki, Claire Chainais-Hillairet, Emmanuel Audusse et Mohammed Boubekeur pour avoir accepté d'examiner ma thèse.

J'ai eu le plaisir de travailler au LAGA et je tiens à remercier tous les membres du laboratoire, en particulier nos chères gestionnaires Yolande, Nathalie, Leila et Monia. Je remercie également Gilles et notre humble directeur, Grégory. Un grand merci aux doctorants et post-docs du laboratoire pour les moments enrichissants, les discussions inspirantes et les innombrables pauses café. Un remerciement spécial aux doctorants avec qui j'ai partagé le bureau A307, pour leur compagnie agréable et pour avoir toujours pris soin de nos plantes. N'oubliez pas de les arroser chaque lundi !

Je remercie mes amis de longue date: A. Anass, Mohamed, Soufian, H. Ayoub, B. Ayoub, Tarik, C. Anas et Issam. Je remercie également Samir, Geneviève, Aziz, Ibrahim, Ghizlan, Romain et Asmae pour leur soutien.

Dans un élan sincère d'amour et de reconnaissance, je souhaite exprimer toute ma gratitude envers ma mère Farida et mon père Hamid. Même si j'écrivais des milliers de pages, je ne pourrais jamais pleinement exprimer mes sentiments. Je vous remercie du fond du cœur pour tout ce que vous avez fait pour moi. À ma tante Karima, je suis profondément reconnaissant pour son soutien constant. À mes frères Morad, Fouad, Ilyass et Mohamed et ma sœur Iman, je suis rempli d'une immense gratitude pour les liens familiaux solides que nous partageons.

Enfin, je remercie tous les joueurs du Rif Epinay Club pour les bons matchs de football.

Résumé

Dans cette thèse, nous proposons une analyse mathématique et numérique des écoulements viscoplastiques, avec une attention particulière portée aux fluides de Bingham. Les fluides de Bingham, un type de fluide viscoplastique, se comportent comme des solides à faible contrainte et comme des fluides non linéaires au-delà d'un seuil de cisaillement.

Le premier résultat de cette thèse concerne l'analyse mathématique de l'équation de Navier-Stokes Bingham. Nous avons établi l'existence et l'unicité d'une solution faible. Dans ce travail, nous proposons de construire une solution faible en utilisant un fluide de bi-viscosité comme approximation. En particulier, nous avons prouvé que le tenseur de bi-viscosité converge faiblement vers le tenseur de Bingham.

Sur le plan numérique, cette thèse propose une méthode de volumes finis efficace pour la simulation des écoulements viscoplastiques. Dans un premier lieu, une méthode de volumes finis caractéristiques (FVC) pour les systèmes hyperboliques unidimensionnels a été introduite. Cette méthode est étendue aux problèmes bidimensionnels sur un millage hybride non structuré. FVC intègre un contrôleur de la diffusion numérique qui permet de mieux capturer les différents phénomènes physiques. Le dernier travail de la thèse concerne la simulation d'écoulements de Bingham compressibles sur un maillage hybride non structuré. Un algorithme de splitting est proposé, intégrant la méthode FVC pour un contrôleur de diffusion numérique afin de simuler avec précision les équations de Bingham compressibles.

Dans l'ensemble, cette thèse représente une avancée significative dans l'analyse et la simulation des fluides viscoplastiques, offrant des aperçus précieux et des approches numériques innovantes pour relever les défis complexes de la dynamique des fluides viscoplastiques.

Mots clés

fluide non-Newtonien incompressible, approximation des fluides non Newtoniens, solution faible, systèmes de Navier-Stokes, fluide de Bingham, existence de solutions, équations d'Euler compressibles, méthode des caractéristiques, méthode des volumes finis, lois de conservation, équations de Navier Stokes compressibles, fluides de Bingham compressibles, couches limites, plaque plane, diffusion numérique.

Abstract

In this thesis, we propose a mathematical and numerical analysis of viscoplastic flows, with a particular focus on Bingham fluids. Bingham fluids, a type of viscoplastic fluid, behave like solids at low stress and like nonlinear fluids above yield stress.

The first work of this thesis is focused on the mathematical analysis of the Navier-Stokes Bingham equation. We have established the existence and uniqueness of a weak solution. In this work, we propose to build a weak solution using a bi-viscosity fluid as an approximation. In particular, we proved that the bi-viscosity tensor converges weakly to the Bingham tensor.

This thesis proposes an efficient finite volume method for simulating viscoplastic flows. Firstly, a Finite Volume Characteristic (FVC) method for one-dimensional hyperbolic systems is introduced. This method is extended to two-dimensional problems on an unstructured hybrid mesh. FVC integrates a numerical diffusion controller to better capture the various physical phenomena. The final work of the thesis concerns the simulation of compressible Bingham flows on an unstructured hybrid mesh. A splitting algorithm is proposed, integrating the FVC method for a numerical diffusion controller to accurately simulate compressible Bingham equations.

Overall, this thesis represents a significant advance in viscoplastic fluid analysis and simulation, offering valuable insights and innovative numerical approaches to the complex challenges of viscoplastic fluid dynamics.

Keywords

Incompressible Bingham fluid, Non-Newtonian fluid approximation, weak solution, Navier-Stokes equation, Bingham viscoplastic, existence of solutions, Compressible Euler equations, Method of characteristics, Finite volume method, Conservation laws, Compressible Navier Stokes equations, Weak compressible Bingham flows, Boundary layers, Flat plate, Numerical diffusion.

Contents

Chapter 1

Introduction

Contents

1.1 Motivation

Every morning, as we wake up to a well-established routine, we experience non-Newtonian fluids without even realizing it. When we squeeze the toothpaste tube, we find that the toothpaste stays rigid inside, acting almost like a solid, but as soon as we apply enough pressure, the toothpaste becomes more fluid and flows easily onto our toothbrush. As we prepare our breakfast, we notice that the texture of our yogurt changes depending on how we stir it. On our way to work, we pass a construction site where we see workers handling concrete, realizing how difficult it is to pour it evenly. When we try to pour ketchup on our hamburger, we notice how it first remains motionless in the bottle, sometimes requiring vigorous shaking to start flowing, and then flows slowly once set in motion. Every interaction throughout the day, whether conscious or unconscious, is marked by the subtle but significant characteristics of so-called non-Newtonian fluids, which are truly omnipresent in our daily lives. All these everyday experiments highlight the properties of non-Newtonian fluids, an area that this thesis aims to explore.

Non-Newtonian fluids are fluids whose viscosity, a measure of their resistance to flow, changes in response to applied stress or shear rate. Unlike Newtonian fluids, which have a constant viscosity no matter what force is applied. The flow behavior of non-Newtonian fluids is complicated and is impacted by various parameters, including shear rate and shear stress. This behavior is studied by Rheology, a physical discipline that analyses how materials flow and deform in response to different applied forces. In many industrial and geophysical domains, an understanding of the Rheology of non-Newtonian fluids is crucial for optimizing manufacturing processes and designing advanced uses in sectors like petroleum engineering and medicine. For additional information on the Rheology and the non-Newtonian models, see [23, 39, 43].

This complicated behavior is converted into a mathematical complexity that results in stress-strain laws, such as the Carreau-Yasuda, Bingham, power law, Cross, Casson, Herschel-Bulkley, etc. Among the various classes of non-Newtonian materials, those exhibiting viscoplastic properties are particularly interesting by their ability to strain only if the stress rate exceeds a minimum value. Many industrial processes involve viscoplastic fluid: mud, cement slurries, emulsions, foams, etc. The most commonly used model to account for this particular behavior is the Bingham model [20]. Eugene Bingham, a professor at Lafayette College, gave the first one-dimensional mathematical law for fluid behaves like a solid at low stresses and like a non-linear fluid above a yield stress τ_y. Later, Prager [54, 55] showed a generalized tensor formulation for multidimensional flows.

1.2 Mathematical models

In the eighteenth century, modern mathematical hydrodynamics was born. In 1750, Euler expressed the belief that the mechanics of continuous media could be treated by applying Newton's law to the infinitely small elements that make up the continuous medium. In 1755, Euler wrote a paper entitled *Principes généraux du mouvement des fluides* , in which he developed equations to describe the behavior of fluids. These equations, known as Euler's equations, apply Newton's law to fluid elements under the influence of external forces and the pressure of neighboring elements. In Euler's equations, the internal forces are described only in terms of pressure. However, since the other elements of the fluids have different velocities, an additional force (friction) is applied to the fluid element in directions tangential to the faces

(viscosity). It was Navier who proposed equations, known as the Navier-Stokes equations, to correct this limitation by taking viscosity into account in the context of fluid dynamics.
Fluid mechanics is based on two types of laws: conservation laws, which describe how certain physical quantities such as mass, momentum, and energy are conserved in the system, and constitutive laws, which describe macroscopic phenomena.

1.2.1 Conservation laws

Conservation of mass

This law implies that mass can neither be created nor destroyed, although it can be rearranged in space or the entities associated with it can change form. This principle, also termed the law of conservation of mass or mass conservation principle, finds expression in the mathematical form of the continuity equation:

$$\partial_t \rho + \nabla \cdot (\rho \mathbf{u}) = 0, \tag{1.1}$$

here, ρ represents the density, $\mathbf{u}$ denotes the velocity vector field.

Conservation of momentum

The law of conservation of momentum results from the direct application of Newton's law: the time rate of change of the momentum in a volume V is equal to the total force acting on the volume V. It can be mathematically expressed as:

$$\partial_t(\rho \mathbf{u}) + \nabla \cdot (\rho \mathbf{u} \otimes \mathbf{u}) + \boldsymbol{\nabla} p = \nabla \cdot \tau + \rho f, \tag{1.2}$$

where p is the pressure, τ is the stress tensor, and f represents external forces.

Conservation of energy

The time rate of change of total energy is equal to the work done, per unit time, by all the forces acting on the volume plus the influx of energy per unit time into the volume. It can be mathematically expressed as:

$$\partial_t(\rho E) + \nabla \cdot ((\rho E + p)\mathbf{u}) - \nabla \cdot (\tau \mathbf{u}) + \nabla \cdot Q = \rho \mathbf{u} \cdot f, \tag{1.3}$$

where E represents the total energy and $\mathbf{Q}$ is the energy flow.

1.2.2 Navier-Stokes equation

Equations (1.1), (1.2) and (1.3) form the Navier-Stokes system. The stress tensor and pressure in these equations, which present the internal forces, are given by the equation of state and Reological law respectively. Some physical hypotheses can lead to other equations which describe certain flows.

Inviscid fluid

A first physical simplification can be made by neglecting the viscosity, conduction of the heat, and external forces. This simplification led us to the Euler equations

$$\begin{cases} \partial_t \rho + \nabla \cdot (\rho \mathbf{u}) = 0, \\ \partial_t (\rho \mathbf{u}) + \nabla \cdot (\rho \mathbf{u} \otimes \mathbf{u}) + \boldsymbol{\nabla} p = 0, \\ \partial_t (\rho E) + \nabla \cdot (\mathbf{u}(\rho E + p)) = 0\cdot \end{cases} \tag{1.4}$$

For an ideal gas, the energy of the system is related to these unknowns with the following equation of state

$$\rho E = \frac{1}{2}\rho |\mathbf{u}|^2 + \frac{p}{(\gamma - 1)}, \tag{1.5}$$

with γ is the ratio of specific heat.

Newtonian fluid

As mentioned earlier in this introduction, Newtonian fluids are characterized by a linear relationship between stress and strain, which implies a constant viscosity μ. Moreover, if we neglect the external forces, we find the Newtonian Navier Stokes equation

$$\begin{cases} \partial_t \rho + \nabla \cdot (\rho \mathbf{u}) = 0, \\ \partial_t (\rho \mathbf{u}) + \nabla \cdot (\rho \mathbf{u} \otimes \mathbf{u}) + \boldsymbol{\nabla} p - \nabla \cdot \tau = 0, \\ \partial_t (\rho E) + \nabla \cdot ((\rho E + p)\mathbf{u}) - \nabla \cdot (\tau \mathbf{u}) + \nabla \cdot Q = 0\cdot \end{cases} \tag{1.6}$$

where the Newtonian viscous stress tensor τ is given by

$$\tau = \mu \left(\nabla \mathbf{u} + \nabla \mathbf{u}^t \right) - \frac{2}{3}\mu (\nabla \cdot \mathbf{u}) \mathbf{I}\cdot \tag{1.7}$$

As the inviscid flow, the pressure is given by an equation of state.

Incompressible fluid

When the fluid is incompressible, the material derivative of the density is equal to zero, therefore

$$\partial_t \rho + \mathbf{u} \cdot \nabla \cdot \rho = 0, \tag{1.8}$$

then, the law of conservation mass become $\nabla \cdot \mathbf{u} = 0$. Moreover, assuming that the flow is isothermal, the energy conservation equation becomes redundant and the Navier stokes equation for an incompressible isothermal flow is given by

$$\begin{cases} \nabla \cdot \mathbf{u} = 0, \\ \partial_t (\rho \mathbf{u}) + \nabla \cdot (\rho \mathbf{u} \otimes \mathbf{u}) + \boldsymbol{\nabla} p = \nabla \cdot \tau + \rho f, \end{cases} \tag{1.9}$$

Barotropic fluid

A fluid in which the pressure is a function only of the density, i.e., $p = p(\rho)$, is called a barotropic fluid and we have the following Navier-Stokes equation

$$\begin{cases} \partial_t \rho + \nabla \cdot (\rho \mathbf{u}) = 0, \\ \partial_t(\rho \mathbf{u}) + \nabla \cdot (\rho \mathbf{u} \otimes \mathbf{u}) + \boldsymbol{\nabla} p - \nabla \cdot \tau(D\mathbf{u}) = \rho f, \end{cases} \tag{1.10}$$

1.2.3 Viscoplastic fluids

Viscoplastic fluid flows constitute a significant area within the realm of non-Newtonian fluid mechanics. This is because a notable portion of fluid flows, whether in natural or industrial settings, are observed to display yield stress. The first one-dimensional model that describes the stress-strain relationship, i.e. the relationship between the stress tensor and the strain rate, was proposed by Bingham [20]

$$\begin{cases} \tau = \left(2\mu + \dfrac{\tau_y}{|\dot{\gamma}|}\right)\dot{\gamma} & \text{if } \dot{\gamma} \neq 0, \\ |\tau| \leq \tau_y & \text{if } \dot{\gamma} = 0\cdot \end{cases} \tag{1.11}$$

where $\dot{\gamma}$ is the shear rate tenser and μ is the plastic viscosity. Prage [55] proposed a generalization of this law in the multi-dimensional case:

$$\begin{cases} \tau = \left(2\mu + \dfrac{\tau_y}{|Du|}\right) Du & \text{if } Du \neq 0, \\ |\tau| \leq \tau_y & \text{if } Du = 0, \end{cases} \tag{1.12}$$

which can be written as follows:

$$\begin{cases} \tau = \left(2\mu + \dfrac{\tau_y}{|\ Du\ |}\right) Du & \text{if } |\tau| > \tau_y, \\ Du = 0 & \text{if } |\tau| \leq \tau_y, \end{cases} \tag{1.13}$$

where Du is the strain tensor defined as $Du = \frac{1}{2}(\nabla u + \nabla u^t)$. In the real world, it is rare for fluids to conform strictly to Bingham law, even if they display a stress threshold. To extend this model, we can use the Herschel–Bulkley model, which includes the shear-thinning property of the plastic viscosity

$$\begin{cases} \tau = \left(2\mu_0 |Du|^{n-1} + \dfrac{\tau_y}{|Du|}\right) Du & \text{if } Du \neq 0, \\ |\tau| \leq \tau_y & \text{if } Du = 0\cdot \end{cases} \tag{1.14}$$

where $n \in [0, 2]$ stands for the shear-thinning coefficient and μ_0 is the plastic viscosity at zero shear rate. Another simple two-parameter model which implicitly exhibits shear expansion

behavior is the Casson model which can be expressed as follows:

$$\begin{cases} \tau = \left(2\mu + 2\sqrt{\tau_y \mu}|Du|^{-1/2} + \dfrac{\tau_y}{|Du|}\right) Du & \text{if } Du \neq 0, \\ |\tau| \leq \tau_y & \text{if } Du = 0\cdot \end{cases} \tag{1.15}$$

Other generalizations of the Bingham tensor, taking into account factors such as compressibility, temperature, and time dependence, are presented in [23]. Although Bingham law is not always adhered to in practice, it offers a valuable understanding of the behavior of many viscoplastic fluids. Therefore, in this thesis, we focus on examining Bingham fluids.

1.3 Analytical aspects

From the moment Euler proposed his model of fluid dynamics, he recognized that his equations would present a significant theoretical challenge and would lead to the emergence of a new mathematical discipline.

"... Cependant tout ce que la Théorie des Fluides renferme est contenu dans ces deux équations, de sorte que ce ne sont pas les principes de Méchanique qui nous manquent dans la poursuite de ces recherches, mais uniquement l'Analyse, qui n'est pas encore assés cultivée, pour ce dessein ..." [1]

Euler could certainly not have known that the existence of solutions to the Navier-Stokes equation would become one of the major mathematical questions of the 21st century.

The mathematical analysis of the incompressible Newtonian Navier Stokes equations is one of the leading research topics that attract the attention of researchers because of the many open questions around this system. A rigorous mathematical existence theory for Newtonian and non-Newtonian fluids can be found in [21, 56, 34, 33, 22].
The Navier Stokes Bingham problem cannot be studied directly because the stress tensor is not explicit below the yield stress τ_y and it is a discontinuous operator. Duvaut and Lions [28] exclude the stress tensor by switching to a variational inequality for the velocity field to overcome these difficulties. Concurrently, Basov and Shelukhin [13, 17] offered an alternative strategy, demonstrating the existence of weak solutions by employing the Bercovier and Engelman model as an approximation for the Bingham fluid.

The first result of this thesis is a proof of the existence of a weak solution for the two-dimensional Navier-Stokes Bingham problem (1.9)-(1.15). The proof of this result is based on the approximation of Bingham fluid using a bi-viscosity fluid, in particular, we proved that the bi-viscosity tensor converges weakly to the Bingham tensor. The idea of this approximation is to consider the Bingham fluid when it behaves like a solid as a highly viscous Newtonian fluid, by involving a second artificial viscosity which becomes infinity when the rate of deformation tends towards zero.

[1] "... Everything that is held within the Theory of Fluids is contained in those two equations, so that it is not the principles of Mechanics that are lacking for the continuation of our research, but only the Analysis, which is still not developed enough for that purpose ..." [34]

1.4 Numerical aspects

The Navier-Stokes equation not only poses analytical challenges but also presents considerable numerical difficulties. Despite these challenges, Computational Fluid Dynamics (CFD) has become an essential tool in a multitude of applications and areas of research. This field is developing at a rapid rate thanks to our technological advances. Among the methods that have significantly contributed to the advancement of the CFD domain is the finite volume method (FVM), which is suitable for the numerical simulation of conservation laws. FVM is widely used in fluid mechanics, heat and mass transfer, and other fields [69, 32, 65]. The Finite Volume Characteristic (FVC) scheme is a FVM that has proved its effectiveness [7, 11, 15, 71, 16]. FVC integrates the characteristics method into the reconstruction of the numerical flow.

Numerical diffusion is a prevalent issue in numerical methods, arising from the processes of spatial and temporal discretization and the resolution schemes employed. Although difficult to avoid, research is underway to minimize diffusion and improve the quality of numerical simulations. Numerous studies and approaches have been carried out to reduce dissipation, see for example [50, 40]. Another factor that characterizes numerical schemes is their cost. A method that significantly reduces numerical diffusion but is prohibitively expensive becomes impractical for widespread use. Consequently, the quest is to devise efficient techniques that reduce numerical diffusion without incurring excessive costs.

This thesis introduces a novel strategy aimed at diminishing numerical diffusion. Chapter 3, outlines a method that is accurate, fast, and conservative method for one-dimensional hyperbolic systems [5]. This approach is simple to implement, has no entropy defect as seen in the numerical tests, and avoids solving Riemann problems. The proposed method has been tested on the Euler equation (1.4); the results show a high accuracy of our method and, more specifically, its ability to capture contact discontinuities. Then, we proposed, in chapter 4, an extension of this approach to the two-dimensional Euler equation (1.4) and Compressible Navier-Stokes equation (1.6) on unstructured hybrid mesh [4]. The results demonstrate that the proposed approach is effective in controlling numerical diffusion and capturing the shock and the boundary layer.

After validating our FVC solver for Newtonian flows in chapters 3 and 4, our next step, and the main objective of this thesis, is to apply this method to compressible Bingham flows. Numerical simulation of compressible Non-Newtonian flows is of great industrial importance, enabling us to model the restarting of pipes carrying viscoplastic fluids [25, 44] as well as the investigation of compressed Bingham fluids in closed pipes [52]. A recent study by Mackay and Phillips [48] investigated the influence of compressibility, viscoelasticity, and thermal effects on the characteristics of a Bingham flow. One-dimensional models have many applications in industries, particularly in transmission pipelines where length is more important than diameter. This simplified approach allows us to better understand and optimize system performance by focusing on a single axis, making computation and prediction easier. For this reason, the one-dimensional model has been carefully treated in chapter 5, where we propose a novel semi-implicit finite volume approach for the one-dimensional Bingham flow 1.10. Numerical results show, using an accuracy test, that FVC is fast and highly accurate. This was followed by a study of the plug zone in the context of weakly compressible two-dimensional Bingham laminar flows. Numerical results illustrate the solid-liquid behavior and the stress-strain relationship that define Bingham fluids. This result represents a significant advance in the simulation of viscoplastic fluids, with a new tool that integrates precision and computational efficiency.

This approach could lead to an application that accurately simulates the complex behavior of compressible and weakly compressible viscoplastic fluids in industrial and geophysical settings.

1.5 Organization of this thesis and contributions

The thesis consists of six chapters, each dedicated to exploring various aspects, ensuring a comprehensive examination of the subject matter. The chapters 5, 3, and a short version of chapter 4 have already been published ([1, 5, 4]) and the final result of this thesis, chapter 5, will soon be submitted for publication.

Chapter 2: Homogeneous incompressible Bingham viscoplastic as a limit of bi-viscosity fluids

In this chapter, the existence of a weak solution for homogeneous incompressible Bingham fluid is investigated. The Rheology of such a fluid is defined by a yield stress τ_y and a discontinuous stress-strain law. This non-Newtonian fluid behaves like a solid at low stresses and like a non-linear fluid above the yield stress. In this work we propose to build a weak solution for Navier stokes Bingham equations using a bi-viscosity fluid as an approximation, in particular, we proved that the bi-viscosity tensor converges weakly to the Bingham tensor. This choice allowed us to show the existence of solutions for a given data $f \in L^2(0, T; V')$.

Chapter 3: A highly efficient finite volume method with a diffusion control parameter for hyperbolic problems

This chapter proposes a highly accurate, fast, and conservative method for hyperbolic systems using the finite volume approach. This innovative scheme constructs the intermediate states at the interfaces of the control volume using the method of characteristics. The approach is simple to implement, has no entropy defect as seen in the numerical tests, and avoids solving Riemann problems. A diffusion control parameter is introduced to increase the accuracy of the scheme. Numerical examples are presented for the one-dimensional Euler equation for an ideal gas. The results demonstrate the method's ability to capture contact discontinuity and shock wave profiles with high accuracy and low cost, as well as its robustness.

Chapter 4: A finite volume scheme with a diffusion control parameter on unstructured hybrid mesh: application to two-dimensional Navier Stokes problem

This chapter presents a new approach to controlling the numerical diffusion in the finite volume characteristic (FVC) scheme. The approach is a generalization of an existing one-dimensional method, and it employs the backward method of characteristics to create interface states. The approach was assessed using two-dimensional Navier-Stokes equations on unstructured hybrid meshes. The results demonstrate that the proposed approach is effective in controlling numerical diffusion and capturing the shock and the boundary layer.

Chapter 5: A finite volume method with a diffusion control parameter for compressible Bingham flows

The final part of this thesis focuses on the numerical simulation of an isothermal compressible Bingham flow, highlighting the effectiveness of the FVC with the diffusion control parameter. In the one-dimensional scenario, we use a semi-implicit method, and for the two-dimensional

case, we extend the FVC/diamond strategy proposed in the previous chapter for Newtonian flows to the case of Bingham flows. The numerical results demonstrate the effectiveness of the FVC method for the one-dimensional case, as well as its capability to simulate the plug zones in the context of weakly compressible two-dimensional Bingham laminar flows.

Chapter 6: Conclusion and outlooks

The conclusion section of this thesis summarizes the key findings and contributions of the research. Additionally, it delves into various potential avenues for future research.

Chapter 2

Homogeneous incompressible Bingham viscoplastic as a limit of bi-viscosity fluids

Contents

Abstract

In this chapter, the existence of a weak solution for homogeneous incompressible Bingham fluid is investigated. The rheology of such a fluid is defined by a yield stress τ_y and a discontinuous stress-strain law. This non-Newtonian fluid behaves like a solid at low stresses and like a non-linear fluid above the yield stress. In this work we propose to build a weak solution for Navier stokes Bingham equations using a bi-viscosity fluid as an approximation, in particular, we proved that the bi-viscosity tensor converges weakly to the Bingham tensor. This choice allowed us to show the existence of solutions for a given data $f \in L^2(0,T;V')$.

2.1 Introduction

As well known, the motion of a homogeneous incompressible fluid is governed by the Navier-Stokes system, which describes the balance of mass and momentum. The classical form of this equation is restricted to fluids whose stress-strain relationship is linear. This category of fluids is called Newtonian fluids. They have a simple molecular structure, e.g., water, air, and alcohol. The mathematical analysis of the Newtonian Navier Stokes equations are one of the leading research topics that attract the attention of researchers because of the many open questions around this system (see [21, 56, 34, 33]).

To study more complex fluids, such as molten plastics, synthetic fibres, biological fluids, paints, and greases, etc., it is necessary to consider a generalized Navier Stokes system that models the behavior of fluids whose viscosity depends on the rate of deformation (i.e., non-Newtonian fluids). This complex behavior is translated into a mathematical complexity which gives rise to complex stress-strain laws, such as the Carreau-Yasuda, Bingham, power law, Cross, Casson, Herschel-Bulkley, etc., for more details on the rheology and the non-Newtonian models, consult [23, 39, 43]. A rigorous mathematical existence theory for non-Newtonian fluids can be found in [22]. Among the various classes of non-Newtonian materials, those exhibiting viscoplastic properties are particularly interesting by their ability to strain only if the stress rate exceeds a minimum value. Many industrial processes involve viscoplastic fluid: mud, cement slurries, emulsions, foams, etc... The most commonly used model to account for this particular behavior is the Bingham model [20]. Eugene Bingham gave the initial mathematical expression in 1922 for one-dimensional flows. Later, Prager [54, 55] showed a generalized tensor formulation for multidimensional flows. From an analytical and numerical viewpoint, we cannot directly study the Navier Stokes Bingham problem since the stress tensor is unexplicit below the yield stress, moreover is a discontinuous operator (which prevents the use of [27]). Duvaut and Lions [28] exclude the stress tensor by passing to a variational inequality for the velocity field to overcome these difficulties. Another solution was proposed by Basov and Shelukhin [13], they proved the existence of weak solutions of the nonhomogeneous incompressible equation by using the Bercovier and Engelman model [17] as an approximation of the Bingham fluid. In [61], Shelukhin used the same approach but with a different approximate tensor.

Our work is based on the approximation of the Bingham tensor by the bi-viscosity tensor, which can be used for numerical simulation (see [18, 23, 38, 6]). Other regularization choices are possible, such as the Papanastasiou model [53] or the algebraic model proposed by Allouche et al. [9]. The reasons behind our choice is that the bi-viscosity operator is coercive, growing, monotonic and continuous, which are the conditions of an existence theorem given by [27]. The idea is to construct a sequence of approximate solutions using the bi-viscosity regularization and the theorem 1 [27], then pass to the limit to prove the existence of a weak solution.

In section 2.2, we give the setting of the problem and the functional spaces, then we present our theorem and we give some remarks about the weak formulation. The proof is shared over three sections; the first step is provided in section 2.3, where we propose an approximate problem and obtain a sequence of approximate solutions. The aim of section 2.4 is to prove various compactness results on the approximate solutions. Section 2.5 is devoted to passing to the limit in the approximate problem; in particular, we prove that the bi-viscosity tensor converges weakly to the Bingham tensor. In the last section, we prove the uniqueness of solutions.

2.2 Setting of the problem and main result

Let Ω be a smooth domain in $\mathbb{R}^2$ with Lipschitz boundary and Ω_T the open set $\Omega \times (0,T)$, where $T > 0$ is the final time.
We consider an unsteady flow of incompressible Bingham fluid in 2D which is governed by the following Navier-Stokes system

$$\begin{cases} \partial_t u + (u \cdot \nabla)u - \nabla \cdot (\tau(Du)) + \nabla p = f & \text{in } \Omega_T, \\ \nabla \cdot u = 0 & \text{in } \Omega_T. \end{cases} \tag{2.1}$$

Here, u is the velocity vector, p is the pressure, and τ is the stress tensor where the strain tensor (shear tensor) is defined as

$$Du = \frac{1}{2}(\nabla u + \nabla u^t),$$

and $f : \Omega_T \to \mathbb{R}^2$ represents the external forces (such as gravity). The system (2.1) is equipped with the following initial condition

$$u(\cdot, 0) = u_0 \qquad \text{in } \Omega, \tag{2.2}$$

and the homogeneous Dirichlet boundary condition

$$u = 0 \qquad \text{on } \partial\Omega \times (0,T). \tag{2.3}$$

The Bingham stress–strain constitutive law is defined as

$$\begin{cases} \tau(Du) = \left(2\mu + \frac{\tau_y}{|Du|}\right) Du & \text{if } |\tau| > \tau_y, \\ Du = 0 & \text{if } |\tau| \le \tau_y. \end{cases} \tag{2.4}$$

Here, μ is the viscosity, τ_y is the yield stress and $|A|^2 = A : A$, where the inner product is defined as $A : B = \sum_{i,j} A_{ij} B_{ij}$. The Bingham tensor can be written as follows:

$$\begin{cases} \tau(Du) = \left(2\mu + \frac{\tau_y}{|Du|}\right) Du & \text{if } Du \neq 0, \\ |\tau| \le \tau_y & \text{if } Du = 0. \end{cases} \tag{2.5}$$

Let us choose some spaces. Let X be a Banach space, for each $1 \le p < \infty$, we defined the following function spaces :

$$H = \left\{ v \in L^2(\Omega),\, \nabla \cdot v = 0, \quad v \cdot n \mid_{\partial\Omega} = 0 \right\},$$

$$V = \left\{ v \in H_0^1(\Omega),\ \ \nabla \cdot v = 0 \right\}.$$

These two spaces are Hilbert spaces equipped with the scalar products respectively induced by those of $L^2(\Omega,\mathbb{R}^2)$ and of $H_0^1(\Omega,\mathbb{R}^2)$, i.e

$$\|v\|_H^2 = \int_\Omega |v|^2 dx \qquad \text{and} \qquad \|v\|_V^2 = \int_\Omega |\nabla v|^2 dx,$$

We also use the following Bochner spaces:

$$L^p(0,T;X) = \left\{ v \text{ measurable from (0,T) into } X,\ \|v\|^p_{L^p(0,T;X)} < \infty \right\},$$

$$L^\infty(0,T;X) = \left\{ v \text{ measurable from (0,T) into } X,\ \|v\|_{L^\infty(0,T;X)} < \infty \right\},$$

where $\|v\|^p_{L^p(0,T;X)} = \displaystyle\int_0^T \|v\|_X^p$ and $\|v\|_{L^\infty(0,T;X)} = \underset{t\in(0,T)}{\text{supess}}\|v\|_X$.

The space $E_{2,2}(V) = \left\{ v \in L^2(0,T;V),\ \partial_t v \in L^2(0,T;V') \right\}$, is a Banach space equipped with the norm

$$\|v\|_{E_{2,2}} = \|v\|_{L^2(0,T,V)} + \|\partial_t v\|_{L^2(0,T,V')}.$$

Where V' is the topological dual of V, and we denote by $\langle\cdot,\cdot\rangle$ the duality bracket between V and V'.

As in [27], we call $(u,\tau(Du)) \in E_{2,2}\times L^2(\Omega_T)$ a weak solution of the problem (2.1)-(2.4), if u satisfies (2.2) and for all $\varphi \in L^2(0,T;V)$ we have

$$\int_0^T \langle \partial_t u, \varphi\rangle + \int_{\Omega_T} \tau(Du) : D\varphi \ + \int_{\Omega_T} (u\cdot\nabla)u\cdot\varphi \ = \int_0^T \langle f,\varphi\rangle \ . \tag{2.6}$$

A similar formulation is given in [21], for the Navier Stokes equation in 2D.

The main result of this work is the following theorem.

Theorem 1. *Assume that $f \in L^2(0,T;V')$ and $u_0 \in H$, then the Navier Stokes equation for a Bingham fluid (2.1)-(2.4), has a weak solution such that*

$$u \in L^2(0,T;V)\cap L^\infty(0,T;H), \quad \partial_t u \in L^2(0,T;V'), \quad \tau(Du)\in L^2(\Omega_T).$$

Remarks. *1. Theorem 1, ensure the existence of a classical weak solution $(u,p)\in E_{2,2}\times \mathcal{D}'(\Omega_T)$, for the system (2.1)-(2.4). Indeed, if we define the distribution $T = \partial_t u + (u\cdot\nabla)u - \nabla\cdot(\tau(Du)) - f$, according to (2.6), we can take $\varphi \in \{\mathcal{D}(\Omega_T), \nabla\cdot\varphi = 0\}$, and we have $\langle T,\varphi\rangle = 0$. On the other hand, the De Rham theorem[1] [26, p. 114] ensures the existence of a primitive of any distribution that cancels on all test functions with null divergence (see [21, th. IV.2.5]). Then, we obtain the existence of $p\in\mathcal{D}'(\Omega_T)$*

[1] A constructive proof of the theorem is given by Simon in [62].

where $T = -\nabla p$, which implies the existence of functions (u, p) solution of (2.1)-(2.4) in $\mathcal{D}'(\Omega_T)$.

2. *We note that this weak formulation is different from the one proposed in [61], where f must belong to $L^2(\Omega_T)$, but in our case, f belongs to $L^2(0, T, V')$.*

3. *The Lions-Magenes theorem [21], implies that the weak solution u is continuous from $[0, T]$ into H.*

2.3 Approximate solutions

In this section, we will build an approximate problem by regularizing the Bingham tensor (2.4), with another operator that approximates the physical behavior of Bingham fluids and has some analytical properties. The regularizing tensor is given by the bi-viscosity model :

$$\tau_m(A) = \begin{cases} 2m\mu A & \text{if } |A| \leq \gamma_m, \\ \left(2\mu + \frac{\tau_y}{|A|}\right) A & \text{if } |A| > \gamma_m. \end{cases} \tag{2.7}$$

Where $A \in \mathbb{M}^{2\times 2}$ and $\gamma_m = \dfrac{\tau_y}{2\mu(m-1)}$, $m \geq 2$. The idea of this approximation is to consider the Bingham fluid when $|\tau| \leq \tau_y$ (which is practically solid) as a highly viscous Newtonian fluid, by involving a second artificial viscosity $\mu_m = m\mu$. Therefore, the equation (2.8) can be viewed as an approximation of (2.6).

Theorem 2. *Assume that $f \in L^2(0, T; V')$ and $u_0 \in H$, then the approximate problem (2.1)-(2.3), (2.7), has at least a solution $u_m \in E_{2,2}$ in the following sense :*

$$\int_0^T \langle \partial_t u_m, \varphi \rangle + \int_{\Omega_T} \tau_m(Du_m) : D\varphi + \int_{\Omega_T} (u_m \cdot \nabla) u_m \cdot \varphi = \int_0^T \langle f, \varphi \rangle, \tag{2.8}$$

for all $\varphi \in L^2(0, T; V)$. Moreover, u_m is continuous from $[0, T]$ into H.

Proof. This result is an application of theorem 1, proved by Dreyfuss and Hungerbühler in [27], in other words, we will check the hypotheses (NS0)-(NS2) given in [27].

Clearly, τ_m satisfies (NS0) since it is a continuous function, which justifies the choice of γ_m. It is easy to prove that $\tau_m(A) : A \geq 2\mu|A|^2$ and that $|\tau_m(A)| \leq \tau_y + 2\mu|A|$, so τ_m satisfied the growth and the coercive hypotheses (NS1).
To prove the strict monotonicity of τ_m, i.e. $(\tau_m(A) - \tau_m(B)) : (A - B) > 0$,
$\forall A \neq B \in \mathbb{M}^{2\times 2}$, we distinguish three cases:
Case 1: if $|A| \leq \gamma_m$, $|B| \leq \gamma_m$ and $A \neq B$, then

$$(\tau_m(A) - \tau_m(B)) : (A - B) = 2m\mu|A - B|^2 > 0. \tag{2.9}$$

Case 2: if $|A| > \gamma_m$, $|B| > \gamma_m$ and $A \neq B$ so

$$\begin{aligned}(\tau_m(A) - \tau_m(B)) : (A - B) &= \left(\left(\frac{\tau_y}{|A|} + 2\mu\right) A - \left(\frac{\tau_y}{|B|} + 2\mu\right) B\right) : (A - B) \\ &= 2\mu|A - B|^2 + \tau_y|A| + \tau_y|B| - \left(\frac{\tau_y}{|A|} + \frac{\tau_y}{|B|}\right) A : B\cdot\end{aligned}$$

By using the Cauchy–Schwarz inequality, we obtain

$$\begin{aligned}(\tau_m(A) - \tau_m(B)) : (A - B) \geq\ & 2\mu|A - B|^2 + \tau_y|A| + \tau_y|B| \\ & - \left(\frac{\tau_y}{|A|} + \frac{\tau_y}{|B|}\right)|A||B|,\end{aligned}$$

and we find

$$(\tau_m(A) - \tau_m(B)) : (A - B) \geq 2\mu|A - B|^2 > 0\cdot \tag{2.10}$$

Case 3: if $|A| > \gamma_m$ and $|B| \leq \gamma_m$, so

$$\begin{aligned}(\tau_m(A) - \tau_m(B)) : (A - B) &= \left(\left(2\mu + \frac{\tau_y}{|A|}\right) A - 2m\mu B\right) : (A - B) \\ &= \left(\left(2m\mu + \frac{\tau_y}{|A|}\right) A - 2m\mu B - 2\mu(m-1)A\right) : (A - B) \\ &= 2m\mu|A - B|^2 + \left(\frac{\tau_y}{|A|} - 2\mu(m-1)\right) A : (A - B)\cdot\end{aligned}$$

On the other hand, we have $|A| > \dfrac{\tau_y}{2\mu(m-1)}$, which gives, in addition to the Cauchy–Schwarz inequality :

$$\begin{aligned}(\tau_m(A) - \tau_m(B)) : (A - B) \geq\ & 2\mu|A - B|^2 \\ & + 2(m-1)\mu|A - B|\left(|A - B| + \frac{\tau_y}{2\mu(m-1)} - |A|\right).\end{aligned} \tag{2.11}$$

We also have $|A - B| + \dfrac{\tau_y}{2\mu(m-1)} - |A| \geq 0$, then $(\tau_m(A) - \tau_m(B)) : (A - B) > 0\cdot$ Finally, we can apply Theorem 1 of [27], with $n = p = 2$. □

Lemma 1. *Form (2.9), (2.10) and (2.11), we deduce the following inequality*

$$(\tau_m(A) - \tau_m(B)) : (A - B) \geq 2\mu|A - B|^2, \qquad \forall A, B \in \mathbb{M}^{2\times 2}\cdot \tag{2.12}$$

This inequality will be used somewhere in this chapter.

2.4 Compactness of approximate solutions

The aim of this section is to prove some results on the sequence u_m.

Proposition 1. *The approximate solution u_m, constructed in Section 2.3, satisfied the following estimations*

(i) *The sequence u_m is bounded in $L^2(0,T;V)\cap L^\infty(0,T;H)$.*

(ii) *The sequence $(u_m\cdot\nabla)u_m$ is bounded in $L^2(0,T;V')$.*

(iii) *The sequence $\tau_m(Du_m)$ is bounded in $L^2(\Omega_T)$.*

(iv) *The sequence $\partial_t u_m$ is bounded in $L^2(0,T;V')$.*

In this chapter, c denotes various constants independent of m.

Proof of (i). By taking u_m as a test function in the weak formulation (2.8), we obtain

$$\underbrace{\int_0^T\langle\partial_t u_m,u_m\rangle}_{:=I_m^1}+\underbrace{\int_{\Omega_T}\tau_m(Du_m):Du_m}_{:=I_m^2}+\underbrace{\int_{\Omega_T}(u_m\cdot\nabla)u_m\cdot u_m}_{:=I_m^3}=\underbrace{\int_0^T\langle f,u_m\rangle}_{:=I_m}\cdot \tag{2.13}$$

Let us start with the integral I_m^1, note that $u_m\in E_{2,2}$, so we use the Lions-Magenes theorem [21]

$$2\int_0^T\langle\partial_t u_m,u_m\rangle=\|u_m(T)\|_H^2-\|u_0\|_H^2,$$

then,

$$I_m^1\geq-\frac{1}{2}\|u_0\|_H^2\cdot \tag{2.14}$$

Now, we will prove the existence of a constant $k>0$ independent of m, such that

$$I_m^2\geq k\|u_m\|_{L^2(0,T;V)}\cdot \tag{2.15}$$

The coercivity of the operator τ_m implies

$$\int_\Omega\tau_m(Du_m):Du_m\geq 2\mu\|Du_m\|_{L^2(\Omega)}^2\cdot \tag{2.16}$$

On the other hand, the Korn inequality[2] ensures the existence of $K_\Omega>0$ such that

$$\|\nabla u_m\|_{L^2(\Omega)}^2\leq K_\Omega\|Du_m\|_{L^2(\Omega)}^2\cdot \tag{2.17}$$

By integrating the inequality (4.16) on $[0,T]$, and using (3.26) we find (2.15).

[2]For more details, see chapter 2 of [22].

For the third integral, we have

$$\int_\Omega (u_m \cdot \nabla) u_m \cdot u_m = \frac{1}{2} \sum_i \int_\Omega u_m^i \frac{\partial}{\partial x_i} |u_m|^2 dx = -\frac{1}{2} \int_\Omega \nabla \cdot u_m |u_m|^2 dx = 0. \tag{2.18}$$

We also have

$$\int_0^T \langle f, u_m \rangle dt \leq \int_0^T \|f\|_{V'} \|u_m\|_V dt.$$

Using the ε-Young inequality with $\varepsilon = k$ (the same k in (2.15)) we obtain

$$I_m \leq \frac{1}{2\varepsilon} \int_0^T \|f\|_{V'}^2 + \frac{\varepsilon}{2} \int_0^T \|u_m\|_V^2. \tag{2.19}$$

From (2.14), (2.15), (2.18) and (2.19) we deduce

$$\varepsilon \|u_m\|_{L^2(0,T;V)} \leq c + \frac{\varepsilon}{2} \|u_m\|_{L^2(0,T;V)} + \frac{1}{2} \|u_0\|_H^2.$$

We conclude that u_m is bounded in $L^2(0,T;V)$.

Now we will show that u_m is bounded in $L^\infty(0,T;H)$. Let $\theta \in (0,T]$, then the function given by $\varphi_m = u_m 1_{[0,\theta]}$, can be a test function in the weak formulation (2.8) and we obtain

$$\underbrace{\int_0^T \langle \partial_t u_m, \varphi_m \rangle}_{:=J_m^1} + \underbrace{\int_{\Omega_T} \tau_m(Du_m) : D\varphi_m}_{:=J_m^2} + \underbrace{\int_{\Omega_T} (u_m \cdot \nabla) u_m \cdot \varphi_m}_{:=J_m^3} = \underbrace{\int_0^T \langle f, \varphi_m \rangle}_{:=J_m}. \tag{2.20}$$

As proved in the first part of this proof, we use the Lions-Magenes theorem

$$J_m^1 = \int_0^\theta \langle \partial_t u_m, u_m \rangle = \frac{1}{2} \|u_m(\theta)\|_H^2 - \frac{1}{2} \|u_0\|_H^2, \tag{2.21}$$

moreover, we have

$$J_m^3 = \int_0^\theta \int_\Omega (u_m \cdot \nabla) u_m \cdot u_m = 0, \tag{2.22}$$

and thanks to the coercivity, we get

$$J_m^2 = \int_0^\theta \int_\Omega \tau_m(Du_m) : Du_m \geq 0. \tag{2.23}$$

By using the Hölder inequality and the boundedness of u_m in $L^2(0,T;V)$, we obtain

$$J_m \leq \|f\|_{L^2(0,T;V')} \|u_m\|_{L^2(0,T;V)} \leq c. \tag{2.24}$$

From (2.21), (2.22), (2.23) and (2.24), we deduce

$$\|u_m(\theta)\|_H^2 \leq c + \|u_0\|_H^2, \qquad \forall \theta \in [0,T]. \tag{2.25}$$

Since c is independent of θ, the sequence u_m is bounded in $L^\infty(0,T;H)$.

□

Proof of (ii). To prove this point, we need the following lemma:

Lemma 2. *The space $L^2(0,T;V) \cap L^\infty(0,T;H)$ is continuously embedded into $L^4(\Omega_T)$.*

Indeed, according to the lemma 6.2 [47] we have $\|v\|_{L^4(\Omega)}^2 \leq c\|v\|_{H_0^1}\|v\|_{L^2}$, for any $v \in H_0^1(\Omega)$. Then we get

$$\|v\|_{L^4(\Omega_T)}^4 \leq c\|v\|_{L^\infty(0,T;H)}^2 \|v\|_{L^2(0,T;V)}^2.$$

So, $L^2(0,T;V) \cap L^\infty(0,T;H)$ is continuously embedded into $L^4(\Omega_T)$.
Form lemma V.11 [21],

$$\int_\Omega (u_m \cdot \nabla) u_m \cdot \varphi = -\int_\Omega (u_m \cdot \nabla)\varphi \cdot u_m, \qquad \forall \varphi \in V. \tag{2.26}$$

Using Cauchy–Schwarz and Hölder inequalities, we obtain

$$\left| \int_\Omega (u_m \cdot \nabla)\varphi \cdot u_m \right| \leq \|u_m\|_{L^4}^2 \|\nabla \varphi\|_{L^2}. \tag{2.27}$$

Therefore,

$$\|(u_m \cdot \nabla) u_m\|_{V'} \leq c\|u_m\|_{L^4}^2.$$

Consequently,

$$\|(u_m \cdot \nabla) u_m\|_{L^2(0,T;V')}^2 \leq c\|u_m\|_{L^4(\Omega_T)}^4. \tag{2.28}$$

However, the sequence u_m is bounded in $L^2(0,T;V) \cap L^\infty(0,T;H)$ and according to the Lemma (2), u_m is bounded in $L^4(\Omega_T)$. Then $(u_m \cdot \nabla)u_m$ is bounded in $L^2(0,T;V')$. □

Proof of (iii). Clearly, $(\tau_m(Du_m))_m$ is bounded in $L^2(\Omega_T)$. Indeed, we have

$$|\tau_m(Du_m)|^2 \leq c(\tau_y^2 + |Du_m|^2).$$

Therefore,

$$\|\tau_m(Du_m)\|_{L^2}^2 \leq c + c\|Du_m\|_{L^2}^2 \leq c + c\|u_m\|_V^2.$$

by using the first estimation, we obtain

$$\|\tau_m(Du_m)\|_{L^2(\Omega_T)} \leq c. \tag{2.29}$$

□

Proof of (iv). Let us use again the weak formulation of the approximate problem. We have

$$\left|\int_0^T \langle \partial_t u_m, \varphi\rangle\right| \leq \left|\int_{\Omega_T} \tau_m(Du_m) : D\varphi\right| + \left|\int_{\Omega_T} (u_m \cdot \nabla)u_m \cdot \varphi\right| + \left|\int_0^T \langle f, \varphi\rangle\right|.$$

By using the Hölder inequality for each integral, we obtain

$$\begin{cases} \displaystyle\int_0^T |\langle f, \varphi\rangle| \leq \|f\|_{L^2(0,T;V')}\|\varphi\|_{L^2(0,T;V)}, \\ \displaystyle\int_{\Omega_T} |\tau_m(Du_m) : D\varphi| \leq \|\tau_m(Du_m)\|_{L^2(\Omega_T)}\|D\varphi\|_{L^2(\Omega_T)}. \end{cases} \tag{2.30}$$

Thanks to (2.27), and to the third estimation, we obtain

$$\left|\int_0^T \langle \partial_t u_m, \varphi\rangle\right| \leq c\|\varphi\|_{L^2(0,T;V)}. \tag{2.31}$$

It follows that

$$\|\partial_t u_m\|_{L^2(0,T;V')} \leq c. \tag{2.32}$$

□

2.5 Passing to the limit

In this section, we will construct a weak solution of (2.1)-(2.4) by using $\{u_m\}$ and some compactness results.

Proposition 2. *The following convergence is proved for subsequences which are denoted by* $\{u_m\}$.

(i) $u_m \to u$ *weakly in* $L^2(0,T;V)$ *and weakly-* in* $L^\infty(0,T;H)$.

(ii) $\partial_t u_m \to \partial_t u$ *weakly in* $L^2(0,T;V')$.

(iii) $(u_m \cdot \nabla)u_m \to (u \cdot \nabla)u$ *weakly in* $L^2(0,T;V')$.

(iv) $\tau_m(Du_m) \to \tau(Du)$ *weakly in* $L^2(\Omega_T)$.

Clearly, the function u satisfy equation (2.6). Moreover, It is easy to see that $\tau_m(Du_m)$ converges weakly to some ξ in $L^2(\Omega_T)$ but the principal difficulty will be to show that ξ is a Bingham tensor.

Proof of (i) . The space $L^2(0,T;V)$ is reflexive, so from any bounded sequence, we can extract a subsequence which converges weakly in $L^2(0,T;V)$, then u_m converges weakly to u in $L^2(0,T;V)$. On the other hand, the space $L^1(0,T;H)$ is separable [3] which gives the weak-* convergence in $L^\infty(0,T;H)$ of a subsequence of u_m, therefore we deduce (i). □

Proof of (ii). We know that the differentiation operator with respect to time is continuous in the sense of distributions, it means $\partial_t u_m \longrightarrow \partial_t u$, in the sense of distribution. But we proved that $\partial_t u_m$ is bounded in $L^2(0,T;V')$ which implies the weak convergence in this space, therefore we deduce (ii) by the uniqueness of the limit in $\mathcal{D}'(\Omega_T)$. □

Proof of (iii). To prove this convergence we need the following strong convergence.

Lemma 3. *The sequence u_m converges strongly to u in $L^2(0,T;H)$ and almost everywhere in Ω_T.*

This lemma is based on the compactness lemma (Theorem 5.1 [47]).
We have $\partial_t u_m \to \partial_t u$ weakly in $L^2(0,T;V')$ and $u_m \to u$ weakly in $L^2(0,T;V)$, using the compactness lemma, we obtain the strong convergence of u_m to u in $L^2(0,T;H)$. Moreover, we can extract a subsequence which converges to u almost everywhere in Ω_T.

Now, we have to prove the weak convergence of $(u_m \cdot \nabla)u_m$ to $u \cdot \nabla u$ in $L^2(0,T;V')$. Due to the lemma 3, $u_m \to u$ a.e in Ω_T, then for all $i,j \in \{1,2\}$ we have

$$u_m^i u_m^j \longrightarrow u^i u^j, \qquad \text{a.e in } \Omega_T. \tag{2.33}$$

We also have

$$\int_\Omega \left(u_m^i u_m^j\right)^2 dx \leq \|u_m^i\|_{L^4}^2 \|u_m^j\|_{L^4}^2.$$

Since, u_m is a bounded sequence in $L^4(\Omega_T)$, (Lemma(2)), we obtain

$$\|u_m^i u_m^j\|_{L^2(\Omega_T)} \leq c.$$

Which gives, by applying Lemma 1.3 [47, p. 12], the following convergence

$$u_m^i u_m^j \to u^i u^j \quad \text{weakly in } L^2(\Omega_T). \tag{2.34}$$

[3] For more details you can see [59, Ch. 1]

Let $\varphi \in L^2(0,T;V)$, then $\int_{\Omega_T} u_m^i \partial_i u_m^j \varphi_j = -\int_{\Omega_T} u_m^i u_m^j \partial_i \varphi_j$ (according to (2.26)). (2.34), permits to conclude that

$$\int_{\Omega_T} u_m^i u_m^j \partial_i \varphi_j \longrightarrow \int_{\Omega_T} u^i u^j \partial_i \varphi_j, \qquad \text{as } m \to \infty.$$

Consequently,

$$\int_{\Omega_T} u_m^i \partial_i u_m^j \varphi_j \longrightarrow \int_{\Omega_T} u^i \partial_i u^j \varphi_j, \qquad \text{as } m \to \infty.$$

Finally, we proved that

$$\int_{\Omega_T} (u_m \cdot \nabla) u_m \cdot \varphi = \sum_{i,j}^{2} \int_{\Omega_T} u_m^i \partial_i u_m^j \varphi_j \longrightarrow \sum_{i,j}^{2} \int_{\Omega_T} u^i \partial_i u^j \varphi_j = \int_{\Omega_T} (u \cdot \nabla) u \cdot \varphi,$$

for all $\varphi \in L^2(0,T;V)$. It follows that $(u_m \cdot \nabla)u_m$ converges to $(u \cdot \nabla)u$ weakly in $L^2(0,T;V')$. □

Proof of (iv). To prove the weak convergence of $\tau_m(Du_m)$ to $\tau(Du)$, we start by proving that Du_m converges strongly to Du in $L^2(\Omega_T)$ (so almost everywhere in Ω_T).

Lemma 4.

$$\int_{\Omega_T} (\tau_m(Du_m) - \tau_m(Du)) : (Du_m - Du) dx dt \longrightarrow 0, \qquad \textit{as } m \to +\infty.$$

Proof. Let us set the following notations :

$$I_m^1 = \int_{\Omega_T} \tau_m(Du_m) : (Du_m - Du), \quad I_m^2 = \int_{\Omega_T} \tau_m(Du) : (Du_m - Du).$$

We proved that $(u_m - u) \in L^2(0,T;V)$, so we can use $(u_m - u)$ as a test function in the weak formulation of the approximate problem, and we obtain

$$\int_0^T \langle \partial_t u_m, u_m - u \rangle + \int_{\Omega_T} \tau_m(Du_m) : D(u_m - u) + \int_{\Omega_T} (u_m \cdot \nabla) u_m \cdot (u_m - u) = \int_0^T \langle f, u_m - u \rangle,$$

which implies that:

$$I_m^1 = \int_{\Omega_T} \tau_m(Du_m) : D(u_m - u) = J_m^1 - J_m^2 - J_m^3.$$

Where

$$J_m^1 = \int_0^T \langle f, u_m - u\rangle dt, \quad J_m^2 = \int_0^T \int_\Omega (u_m \cdot \nabla) u_m \cdot (u_m - u) dx dt,$$

$$\text{and} \quad J_m^3 = \int_0^T \langle \partial_t u_m, u_m - u\rangle dt\cdot$$

Since $u_m \to u$ weakly in $L^2(0,T;V)$, then $\lim\limits_{m\to\infty} J_m^1 = 0$.

On other hand, $J_m^2 = -\int_0^T \int_\Omega (u_m \cdot \nabla) u_m \cdot u$, and from convergence (iv),

$$J_m^2 \longrightarrow \int_{\Omega_T} (u \cdot \nabla) u \cdot u = 0\cdot$$

For J_m^3, we use the Lions–Magenes theorem :

$$\frac{1}{2}\|u_m(T) - u(T)\|_H^2 = \int_0^T \langle \partial_t(u_m - u), u_m - u\rangle dt + \frac{1}{2}\|u_m(0) - u(0)\|_H^2\cdot$$

Moreover, $\int_0^T \langle \partial_t u, u_m - u\rangle dt \to 0$ as $m \to \infty$, this gives

$$\lim_{m\to\infty} \int_0^T \langle \partial_t u_m, u_m - u\rangle dt = \lim_{m\to\infty} \frac{1}{2}\|u_m(T) - u(T)\|_H^2 - \frac{1}{2}\|u_0 - u(0)\|_H^2\cdot$$

To deduce that $u_0 = u(0)$ in H, we will prove that $u_m(0) \longrightarrow u(0)$ weakly in H.
We know that $E_{2,2}$ is continuously embedded into $C^0([0,T];H)$, then $u_m(0)$ is bounded in H. On the other hand, (i) and (iii) of proposition (2) imply that $u_m(0)$ converges weakly to $u(0)$ in V'. Consequently, we deduce that $u_m(0) \to u(0)$ weakly in H. Therefore, $\lim\limits_{m\to\infty} J_m^3 \geq 0$, which implies that

$$\lim_{m\to\infty} I_m^1 \leq 0\cdot \tag{2.35}$$

Now, let us prove that $\lim\limits_{m\to\infty} I_m^2 = 0$. We know that the sequence u_m converges weakly to u in $L^2(\Omega_T)$, so, the sequence Du_m converges to Du in $D'(\Omega_T)$. In addition, $(Du_m)_m$ is bounded in $L^2(\Omega_T)$, then we deduce that

$$Du_m \longrightarrow Du \quad \text{weakly in } L^2(\Omega_T)\cdot$$

On the other hand, $\tau_m(Du)$ converges strongly to ϕ in $L^2(\Omega_T)$, where:

$$\phi = \begin{cases} \left(2\mu + \frac{\tau_y}{|Du|}\right) Du & \text{if } |Du| > 0, \\ \\ 0 & \text{if } Du = 0\cdot \end{cases} \tag{2.36}$$

Consequently

$$\lim_{m\to\infty}\int_{\Omega_T}(\tau_m(Du_m)-\tau_m(Du)):(Du_m-Du)\leq 0, \tag{2.37}$$

which, with the strict monotonicity of τ_m, gives

$$\lim_{m\to\infty}\int_{\Omega_T}(\tau_m(Du_m)-\tau_m(Du)):(Du_m-Du)=0\cdot$$

□

Lemma 5. *(Du_m) converges to Du strongly in $L^2(\Omega_T)$ and a.e in Ω_T.*

This lemma is a consequence of Lemma 4 and Lemma 1. Recall that we have the following inequality

$$2\mu|Du_m-Du|^2\leq(\tau_m(Du_m)-\tau_m(Du)):(Du_m-Du)\cdot \tag{2.38}$$

Then, we deduce

$$\lim_{m\to\infty}\|Du_m-Du\|^2_{L^2(\Omega_T)}\longrightarrow 0\cdot$$

We know that $\tau_m(Du_m)$ converges weakly to an element ξ in $L^2(\Omega_T)$. So we must check that ξ is a Bingham tensor. The following proof is inspired by [61], where Shelukhin et al. studies the Bingham problem with periodic boundary conditions.

We fix the following notations

$$\Omega_T^+=\Omega_T\cap\{|Du|>0\},\qquad \Omega_T^0=\Omega_T\cap\{|Du|=0\}\cdot \tag{2.39}$$

Part 1: Let us proof that $|\xi|\leq\tau_y$ a.e in Ω_T^0. Define

$$A=\Omega_T^0\cap\{|\xi|>\tau_y\},\qquad \varphi=\frac{\xi}{|\xi|}1_A,\qquad I=\int_{\Omega_T}\xi:\varphi,$$

$$I_m=\int_{\Omega_T}\tau_m(Du_m):\varphi,\qquad a=I-\tau_y\text{meas(A)}\cdot$$

Suppose that meas(A) >0, then $I=\int_A|\xi|>\text{meas(A)}\tau_y$, therefore $a>0$.
On the other hand I_m converges to I, i.e

$$\forall\varepsilon>0,\ \exists M(\varepsilon)\in\mathbb{N}:\quad\forall m\geq M(\varepsilon),\quad I-\varepsilon\leq I_m\leq I+\varepsilon\cdot$$

We choose $\varepsilon = \frac{a}{2}$. Then, there exists $M(a)$, such that

$$I_m \geq \frac{a}{2} + \tau_y \text{meas(A)}, \qquad \forall m \geq M(a)\cdot \tag{2.40}$$

Let $m > \max(M(a), \eta)$, with $\eta = f_l\left(\frac{3\tau_y \text{meas(A)}}{a} + 1\right) + 1$, where f_l is the floor function. Furthermore, we denote

$$A_m^1 = \Omega_T \cap \{|Du_m| \leq \gamma_m\}, \qquad A_m^2 = \Omega_T \cap \{\gamma_m < |Du_m| \leq \gamma_\eta\}$$

$$\text{and} \qquad A_m^3 = \Omega_T \cap \{|Du_m| > \gamma_\eta\}.$$

We have

$$I_m = \underbrace{\int_{A_m^1} 2m\mu Du_m : \varphi}_{:=I_m^1} + \underbrace{\int_{A_m^2} \left(2\mu + \frac{\tau_y}{|Du_m|}\right) Du_m : \varphi}_{:=I_m^2} + \underbrace{\int_{A_m^3} \left(2\mu + \frac{\tau_y}{|Du_m|}\right) Du_m : \varphi}_{:=I_m^3}\cdot$$

Now calculate

$$|I_m^1| \leq \int_{A_m^1 \cap A} 2m\mu |Du_m| \leq \frac{m}{m-1}\tau_y \text{meas}(A_m^1 \cap A), \tag{2.41}$$

$$\begin{aligned} |I_m^2| &\leq \tau_y \text{meas}(A_m^2 \cap A) + \int_{A_m^2 \cap A} 2\mu |Du_m| \\ &\leq \frac{m}{m-1}\tau_y \text{meas}(A_m^2 \cap A) + 2\mu\gamma_\eta \text{meas}(\Omega_T), \end{aligned} \tag{2.42}$$

$$|I_m^3| \leq \frac{m}{m-1}\tau_y \text{meas}(A_m^3 \cap A) + 2\mu \|Du_m\|_{L^2(\Omega_T)} \sqrt{\text{meas}(A_m^3 \cap A)}\cdot \tag{2.43}$$

From (2.40), (2.41), (2.42) and (2.43), we get

$$\begin{aligned} \frac{a}{2} + \tau_y \text{meas(A)} \leq \frac{m}{m-1}\tau_y \text{meas(A)} + 2\mu\gamma_\eta \text{meas}(\Omega_T) \\ + 2\mu \|Du_m\|_{L^2(\Omega_T)} \sqrt{\text{meas}(A_m^3 \cap A)})\cdot \end{aligned} \tag{2.44}$$

Due to the choice of η, we obtain $\gamma_\eta < \dfrac{a}{6\mu \text{meas}(\Omega_T)}$, and we have $\text{meas}(A \cap A_m^3) \to 0$, so

$$\frac{a}{2} + \tau_y \text{meas(A)} \leq \tau_y \text{meas(A)} + \frac{a}{3}\cdot \tag{2.45}$$

Which is absurd, i.e $\text{meas(A)} = 0$, thus $|\xi| \leq \tau_y$ a.e in Ω_T^0.

Part 2: Let us proof that $\xi = \tau(Du)$ a.e in Ω_T^+.

Set

$$B_m^1 = \Omega_T^+ \cap \{|Du_m| \leq \gamma_m\} \quad \text{and} \quad B_m^2 = \Omega_T^+ \cap \{|Du_m| > \gamma_m\}.$$

We have

$$W_m := |\tau_m(Du_m) - \tau(Du)|\, 1_{\Omega_T^+} = \left|2\mu Du_m 1_{B_m^1} + F(Du_m)1_{B_m^2} - F(Du)1_{\Omega_T^+}\right|,$$

where, $F(A) = \left(2\mu + \dfrac{\tau_y}{|A|}\right) A$, then

$$W_m \leq \frac{m}{m-1}\tau_y 1_{B_m^1} + \left|F(Du_m)1_{B_m^2} - F(Du)1_{\Omega_T^+}\right|\cdot$$

However, $Du_m \to Du$ a.e in Ω_T^+ and the function $X \mapsto F(X)$ is continuous, then $F(Du_m) \to F(Du)$ a.e in Ω_T^+. On the other hand $1_{B_m^1} \to 0$ and $1_{B_m^2} \to 1_{\Omega_T^+}$, which gives $W_m \to 0$, i.e.

$$\tau_m(Du_m) \to \tau(Du) \quad \text{ a.e in } \Omega_T^+\cdot$$

Let $\psi \in L^\infty(\Omega_T)$ be such that $\psi_{|_{\Omega_T^0}} = 0$. Let $Q' \subset \Omega_T$, $\theta_m = \tau_m(Du_m) : \psi$, and $\theta = \tau(Du) : \psi$. Using the Hölder inequality, we obtain

$$\int_{Q'} |\theta_m| \leq ||\psi||_{L^\infty(\Omega_T)} \sqrt{\text{meas}(Q')} \left(\tau_y \sqrt{\text{meas}(\Omega_T)} + 2\mu \|Du_m\|_{L^2(\Omega_T)}\right)\cdot \tag{2.46}$$

Therefore θ_m is uniformly integrable on Ω_T and $\theta_m \to \theta$ a.e in Ω_T. This gives, thanks to Vitali theorem, $\displaystyle\int_{\Omega_T^+} \tau_m(Du_m) : \psi \to \int_{\Omega_T^+} \tau(Du) : \psi$.
On the other hand $\tau_m(Du_m)$ converges weakly to ξ in $L^2(\Omega_T)$, then $\tau(Du) = \xi$ a.e in Ω_T^+.
Finally, we proved that $\tau_m(Du_m)$, converges weakly to a Bingham tensor and the proof is completed. □

2.6 Uniqueness of solutions

In this section, we will prove that the problem (2.1)-(2.4) has a unique solution. To do this we are inspired by the uniqueness proof of the Newtonian Navier Stokes equation.
We consider u_1 and u_2 to be two weak solutions of (2.6) and introduce $u = u_1 - u_2$. Therefore, we obtain

$$\begin{aligned}\int_0^T \langle \partial_t u, \varphi\rangle + \int_{\Omega_T} (\tau(Du_1) - \tau(Du_2)) : D\varphi \; + \int_{\Omega_T} (u_1 \cdot \nabla)u_1 \cdot \varphi \\ - \int_{\Omega_T} (u_2 \cdot \nabla)u_2 \cdot \varphi = 0, \qquad \forall \varphi \in L^2(0,T;V)\cdot\end{aligned} \tag{2.47}$$

On the other hand, we have

$$\int_{\Omega_T}(u_1\cdot\nabla)u_1\cdot\varphi\ -\int_{\Omega_T}(u_2\cdot\nabla)u_2\cdot\varphi=\int_{\Omega_T}(u_2\cdot\nabla)u\cdot\varphi\ +\int_{\Omega_T}(u\cdot\nabla)u_1\cdot\varphi\cdot$$

Let $t\in(0,T)$. Taking the function $\varphi=u1_{[0,t]}$ in (2.47) yields

$$\begin{aligned}&\int_0^t\langle\partial_t u,u\rangle ds+\int_0^t\int_\Omega(\tau(Du_1)-\tau(Du_2)):Du\ dxds\\&+\int_0^t\int_\Omega(u\cdot\nabla)u_1\cdot u\ dxds+\int_0^t\underbrace{\int_\Omega(u_2\cdot\nabla)u\cdot u\ dx}_{=0}ds=0\cdot\end{aligned}\tag{2.48}$$

Using the Lions-Magenes Theorem we obtain

$$\begin{aligned}\frac12\|u(s)\|_H^2+\int_0^t\int_\Omega(u\cdot\nabla)u_1\cdot u+\int_0^t\int_\Omega(\tau(Du_1)-\tau(Du_2)):Du\\=\frac12\|u(0)\|_H^2\cdot\end{aligned}\tag{2.49}$$

According to (2.27) and Lemma(2) we have

$$\int_\Omega|(u\cdot\nabla)u_1\cdot u\ |\,dx\le c\|u\|_V\|u\|_H\|u_1\|_V\cdot\tag{2.50}$$

Furthermore, we can easily prove the following inequality[4]

$$(\tau(A)-\tau(B)):(A-B)\ge2\mu|A-B|^2,\qquad\forall A,B\in\mathbb{M}^{2\times2}\cdot\tag{2.51}$$

From (2.51) and Korn's inequality we obtain

$$\int_\Omega(\tau(Du_1)-\tau(Du_2)):Du\ dx\ge\frac{2\mu}{K_\Omega}\|u\|_V^2\cdot\tag{2.52}$$

Thus,

$$\begin{aligned}\frac12\|u(s)\|_H^2+\frac{2\mu}{K_\Omega}\int_0^t\|u\|_V^2ds\le&c\int_0^t\|u\|_V\|u\|_H\|u_1\|_V\ ds\\&+\frac12\|u(0)\|_H^2\cdot\end{aligned}\tag{2.53}$$

Using Young's inequality, we get

$$\|u(s)\|_H^2\le\|u(0)\|_H^2+c\int_0^t\|u\|_H^2\|u_1\|_V^2\ ds\cdot\tag{2.54}$$

[4]We can adapt the proof of the strict monotonicity of τ_m.

Thanks to the Gronwall lemma, we deduce that

$$\|u(s)\|_H^2 \leq \|u(0)\|_H^2 \exp\left(c\int_0^t \|u_1\|_V^2 \, ds\right), \qquad \forall t \in [0,T]\cdot$$

Since $u(0) = 0$, we get the uniqueness of the weak solutions.

Corollary 1 (Energy equality)**.** *The solution u is more than a classical weak solution. In fact, we have $u \in C^0([0,T];H)$, moreover, for all $s_1, s_2 \in [0,T]$, u satisfies the following energy equality*

$$\frac{1}{2}\|u(s_2)\|_{L^2(\Omega)}^2 + \int_{s_1}^{s_2}\int_\Omega \tau(Du) : Du = \int_{s_1}^{s_2} \langle f, u\rangle + \frac{1}{2}\|u(s_1)\|_{L^2(\Omega)}^2\cdot \tag{2.55}$$

To prove the energy equality, we have only to take $\varphi = u1_{[s_1,s_2]}$ as a test function in (2.6) and use the Lions-Magenes theorem.

Corollary 2 (Variational inequality)**.** *The weak solution given by Theorem 1 satisfies the following variational inequality, for all $\varphi \in L^2(0,T;V)$*

$$\int_0^T \langle \partial_t u, \varphi - u\rangle + \int_{\Omega_T} (u\cdot\nabla)u\cdot\varphi + 2\mu\int_{\Omega_T} Du : D(\varphi - u) + \tau_y\int_{\Omega_T}(|D\varphi| - |Du|)$$

$$\geq \int_0^T \langle f, \varphi - u\rangle\cdot \tag{2.56}$$

Proof. Let us show the following inequality

$$\int_{\Omega_T} \tau(Du) : D(\varphi - u) \leq 2\mu\int_{\Omega_T} Du : D(\varphi - u) + \tau_y\int_{\Omega_T}|D\varphi| - \tau_y\int_{\Omega_T}|Du|\cdot \tag{2.57}$$

Using the Cauchy–Schwarz inequality and with the notation (2.39), we obtain

$$\begin{aligned}
\int_{\Omega_T^+} \tau(Du) : D(\varphi - u) &= \int_{\Omega_T^+}\left(2\mu + \frac{\tau_y}{|Du|}\right) Du : D(\varphi - u)\\
&= 2\mu\int_{\Omega_T} Du : D(\varphi - u) + \tau_y\int_{\Omega_T^+}\frac{Du : D\varphi}{|Du|} - \tau_y\int_{\Omega_T}|Du|\\
&\leq 2\mu\int_{\Omega_T} Du : D(\varphi - u) + \tau_y\int_{\Omega_T^+}|D\varphi| - \tau_y\int_{\Omega_T}|Du|\cdot
\end{aligned}$$

We also have

$$\int_{\Omega_T^0} \tau(Du) : D(\varphi - u) = \int_{\Omega_T^0}\tau(Du) : D\varphi \leq \tau_y\int_{\Omega_T^0}|D\varphi|\cdot \tag{2.58}$$

Hence, we deduce the inequality (2.57). This implies, jointly with (2.6), the variational inequality. □

Remark 1. *The inequality* (2.56) *implies that* u *satisfies the variational inequality proposed by Lions and Duvaut in [28], i.e.*

$$\begin{aligned}\langle \partial_t u(t), \varphi - u(t)\rangle + \int_\Omega (u(t)\cdot\nabla)u(t)\cdot\varphi + 2\mu\int_\Omega Du(t) : D(\varphi - u(t)) \\ + \tau_y \int_\Omega (|D\varphi| - |Du(t)|) \geq \langle f, \varphi - u(t)\rangle,\end{aligned} \tag{2.59}$$

for any $\varphi \in V$*. The proof of this result is given in [28, p. 300-301].*

2.7 Conclusion and outlook

As mentioned in the introduction, this work aims to prove the existence of the Navier Stokes equation solution for an incompressible homogeneous fluid that follows the Bingham model. In the first step, we constructed an approximate problem using the bi-viscosity model, which behaves like a Newtonian fluid under weak stress and like a non-Newtonian fluid when the stress rate is great than the yield stress. After this approximation, we applied the theorem presented by Dreyfuss and Hungerbuhler in [27], and then a weak solution to the problem in question was constructed by passing to the limit. This analysis shows that the conditions of Theorem 1 [27] is sufficient but not necessary since the Bingham tensor does not satisfy them. Another essential advantage of our theorem is that the membership of the function f to the space $L^2(\Omega_T)$ is not necessary (which is the case in [61, 13]). The next objective is to extend Theorem 1 to a thixotropic Bingham model, i.e., the yield strength is linearly dependent on the structural parameter, which follows a first-order rate equation taking into account the decay and accumulation of the material structure. The study of the non-homogeneous case may also be the subject of future work. The convergence of the Bingham solution to The Newtonian solution, when $\tau_y \to 0$, can be proved. A long-term objective is to analyze the non-Newtonian Navier Stokes equation, more complicated than the Bingham model, as Herschel–Bulkley and Casson models.

Chapter 3

A highly efficient finite volume method with a diffusion control parameter for hyperbolic problems

Contents

Abstract

This chapter proposes a highly accurate, fast, and conservative method for hyperbolic systems using the finite volume approach. This innovative scheme constructs the intermediate states at the interfaces of the control volumes using the method of characteristics. The approach is simple to implement, has no entropy defect as seen in the numerical tests, and avoids solving Riemann problems. A diffusion control parameter is introduced to increase the accuracy of the scheme. Numerical examples are presented for the the one-dimensional Euler equation for an ideal gas. The results demonstrate the method's ability to capture contact discontinuity and shock wave profiles with high accuracy and low cost, as well as its robustness.

3.1 Introduction

A complementary approach to experiment and modeling, numerical simulation is one of the three pillars of scientific research. Fluid mechanics is one of the pioneering sectors in this triangle, and the development of numerical schemes well suited to fluid mechanics is a subject that interests numerical scientists. One of the difficulties is reconciling accuracy and robustness with a reasonable computational cost, but the complications can be quite different depending on the targeted applications. Thus, despite the numerous works and the advances in a subject that is still relevant today [2, 66], it is quite natural that there is no uniformly efficient method in all regimes.

In the context of the numerical approximation of hyperbolic systems of conservation laws, several methods based essentially on the solution of the Riemann problem have been retained, and concern shock capturing schemes [3, 67, 46, 57, 68]. These methods propose strategies allowing the exact solution of the Riemann problem at each interface, which makes them expensive. In order to reduce the computational time, other approaches propose an approximate solution to the Riemann problem. For example, Roe and Harten [57, 58, 35] provided schemes based on the evaluation of numerical flux from the exact solution of the linearized problem, and the industry widely uses these schemes because they can capture shock waves with reasonable accuracy.

The main goal of this chapter is to describe a new method that can be an excellent tool for simulating most compressible flow phenomena. The proposed scheme belongs to a class of numerical schemes that incorporates the method of characteristics in reconstructing numerical flux. The classical version (without the diffusion control parameter) of this approach is called the Finite Volume Characteristics (FVC) scheme and has been proposed by Benkhaldoun and Seaïd in [16] and used in the context of shallow water flow [7, 11, 15, 71].

The proposed scheme is easy to implement, fast, and it accurately solves hyperbolic systems of conservation laws; moreover, it avoids the resolution of Riemann problem in the time integration process, and it is conservative. To approximate the characteristic curves, an iterative process is used, and the intermediate states are calculated using polynomial interpolation. These features are demonstrated using several reference problems for the Euler equations [24, 2]. The presented results provide accurate solutions with a low computational cost. The implementation procedure is described. It is simple to program and generates the numerical results for compressible Euler equations.

This chapter is structured as follows: a brief description of the mathematical model will be presented in Section 3.2. Section 3.3 is devoted to presenting the process of construction of the numerical scheme. Then, the results of the simulation will be presented in Section 3.4. The accuracy and the efficiency of the method are discussed, and some conclusions are presented in Section 3.5.

3.2 Governing equation

We consider the one-dimensional Euler equations modeling the dynamics of non-viscous fluid [65, p. 1-12]

$$\frac{\partial \mathbf{W}}{\partial t} + \frac{\partial \mathbf{F}(\mathbf{W})}{\partial x} = 0, \tag{3.1}$$

where

$$\mathbf{W} = \begin{pmatrix} \rho \\ \rho u \\ E \end{pmatrix}, \quad \text{and} \quad \mathbf{F}(\mathbf{W}) = \begin{pmatrix} \rho u \\ \rho u^2 + p \\ u(E+p) \end{pmatrix}, \tag{3.2}$$

where ρ is the density of the fluid, u is the fluid particle velocity, E is the total energy and p is the pressure. The state equation links $\rho,\ u,\ p$ and E as

$$E = \rho\left(\frac{1}{2}u^2 + e(\rho, p)\right), \tag{3.3}$$

where e is the specific internal energy; for ideal gases it has a following expression

$$e(\rho, p) = \frac{p}{(\gamma - 1)\rho}, \tag{3.4}$$

with γ is the ratio of specific heats, it is a constant that depends on the particular gas, e.g. $\gamma = 1.4$ for air. Another quantity that expresses the ratio of the local velocity of the fluid to the sound speed in this same fluid is called Mach number, which is a dimensionless number defined as

$$M = \frac{u}{c}, \tag{3.5}$$

where c is the sound speed in a gas. For an ideal gas, we can express c by

$$c = \sqrt{\frac{\gamma p}{\rho}}, \tag{3.6}$$

c varies with the nature and temperature of the fluid. So, the Mach number does not correspond to a fixed speed; it depends on local flow conditions. Generally, the speed is categorized by its corresponding regimes [70]. For example, subsonic regime ($M < 0.8$), transonic regime ($0.8 \leqslant M < 1.2$), supersonic regime ($1.2 \leqslant M < 5$) and hypersonic regime ($M \geqslant 5$).

A simple calculation shows that the system can be written in a quasi-linear form

$$\partial_t \mathbf{W} + \mathbf{J}_F \partial_x \mathbf{W} = 0, \tag{3.7}$$

where $\mathbf{J}_F$ is the Jacobian matrix of the physical flux $\mathbf{F}$ given by

$$\mathbf{J}_F = \begin{pmatrix} 0 & 1 & 0 \\ (\gamma - 3)\frac{u^2}{2} & (\gamma - 3)u & \gamma - 1 \\ (\frac{\gamma - 1}{2}u^2 - H)u & H + (1 - \gamma)u^2 & \gamma u \end{pmatrix},$$

here, H is the total specific enthalpy defined by

$$H = \frac{E + p}{\rho}. \tag{3.8}$$

The matrix $\mathbf{J}_F$ has three eigenvalues: $\lambda_1 = u - c$, $\lambda_2 = u$, and $\lambda_3 = u + c$. and the corresponding eigenvectors are

$$\mathbf{r}_1 = \begin{pmatrix} 1 \\ u - c \\ H - uc \end{pmatrix}, \quad \mathbf{r}_2 = \begin{pmatrix} 1 \\ u \\ \frac{u^2}{2} \end{pmatrix}, \quad \text{and} \quad \mathbf{r}_3 = \begin{pmatrix} 1 \\ u + c \\ H + uc \end{pmatrix}. \tag{3.9}$$

There are other mathematical quantities related to the quasi-linear Euler equations called the Riemann invariants that are constant along the characteristic curves; the right and left Riemann invariants are

$$RI_1 = u - \frac{2c}{\gamma - 1}, \quad \text{and} \quad RI_2 = u + \frac{2c}{\gamma - 1}. \tag{3.10}$$

Another form of Euler equations using the primitive variables can be formulated as

$$\partial_t \mathbf{W} + \mathbf{A}_{\mathbf{W}} \partial_x \mathbf{W} = 0, \tag{3.11}$$

where

$$\mathbf{W} = \begin{pmatrix} \rho \\ u \\ p \end{pmatrix}, \quad \text{and} \quad \mathbf{A}_{\mathbf{W}} = \begin{pmatrix} u & \rho & 0 \\ 0 & u & \frac{1}{\rho} \\ 0 & \gamma p & u \end{pmatrix}. \tag{3.12}$$

However, it turns out that for non-smooth solutions, the non-conservative formulations give incorrect shock solutions. This point has been noticed for shallow water equations [65, Subsection 3.3]. Despite this, non-conservative formulations have some advantages over their conservative counterpart when analyzing equations [42, 64].

3.3 Numerical method

In this section, we present our method for Euler equations (3.1). The method consists of two steps, predictor and corrector; in the first step, we construct the intermediate states using the method of characteristics, while in the second step, the numerical flux in the conservative discretization will be built using the physical flux.

3.3.1 Conservative discretization

The space-time evolution of the fluid motion is described by a vector function $\mathbf{W}(x, t)$, whose components are three flow-dependent variables. Computationally, this function is replaced by $\mathbf{W}_i^n$, which is an approximation of $\mathbf{W}(i\Delta x, n\Delta t)$, where, for simplicity, Δx and Δt are considered small constants that define a computational space-time grid. To properly capture the shocks generated by the equation system (3.1), $\mathbf{W}$ was chosen as $\mathbf{W}(x, t)$, the vector of variables in the model continues. P.D. Lax [45] addressed the fundamental problem of determining the $(n + 1)$ time-level solution from n-level data by creating **interface states** at

location such as $(i+1/2)\,\Delta x$ and proposed the following discretization

$$\frac{\mathbf{W}_i^{n+1}-\mathbf{W}_i^n}{\Delta t}+\frac{\mathbf{F}_{i+1/2}^n-\mathbf{F}_{i-1/2}^n}{\Delta x}=0. \tag{3.13}$$

Lax showed that we would recover the partial differential equation (1) when Δx and Δt go to zero in (3.13), with a good construction of $\mathbf{F}_{i+1/2}$ from the values of $\mathbf{W}$ in some neighborhood of $i+1/2$. Then, given the initial data $\mathbf{W}_i^0$ for all i, we can use equation (3.13) to construct the solution at the next instant. Thus, we define $\mathbf{W}_i^n$ as follows

$$\mathbf{W}_i^n=\frac{1}{\Delta x}\int_{(i-1/2)\Delta x}^{(i+1/2)\Delta x}\int_{n\Delta t}^{(n+1)\Delta t}\mathbf{W}(x,t)dtdx, \tag{3.14}$$

and $\mathbf{F}_{i\pm1/2}^n:=\mathbf{F}\left(\mathbf{W}_{i\pm1/2}^n\right)$ are the numerical fluxes at $x_{i\pm1/2}:=(i\pm1/2)\,\Delta x$ and time $t_n:=n\Delta t$. The spatial discretization of equation (3.13) is complete when a numerical construction of the fluxes $\mathbf{F}_{i\pm1/2}^n$ is chosen. In general, this construction requires a solution of Riemann problems at the interfaces $x_{i\pm1/2}$. From a computational viewpoint, this procedure is very demanding and may restrict the application of the method for which Riemann solutions are not available.

In the present work, we reconstruct the intermediate states $\mathbf{W}_{i\pm1/2}^n$ using the method of characteristics. The fundamental idea of this method is to impose a regular grid at the new time level and to backtrack the flow trajectories to the previous time level. At the old-time level, the quantities that are needed are evaluated by interpolation from their known values on a regular grid.

3.3.2 Method of characteristics

This method for hyperbolic systems of conservation laws can be carried out componentwise, provided that the conservative equations can be rewritten in an advective formulation. In general, the advective form of the system under study is built such that the conservative variables are transported with the same velocity field. In the current study, we apply our method to the Euler equations; we first reformulated the system of equations (3.1) in an advective form as

$$\partial_t\mathbf{W}+u\partial_x\mathbf{W}=\mathbf{G}(\mathbf{W}), \tag{3.15}$$

where

$$\mathbf{W}=\begin{pmatrix}\rho\\ \rho u\\ E\end{pmatrix},\quad\text{and}\quad\mathbf{G}(\mathbf{W})=\begin{pmatrix}-\rho\partial_x u\\ -\rho\partial_x u-\partial_x p\\ -E\partial_x u-\partial_x(pu)\end{pmatrix}. \tag{3.16}$$

$\mathbf{G}$ is considered as a source term of the transport equation (3.15), which will be discretized later using the finite difference method for the derivatives it contains.
This version of the equation is used to reconstruct the intermediate states $\mathbf{W}_{i+1/2}^n$ using the method of characteristics. We calculate now the characteristic curves $x_c(s)$ associated to

(3.15) as

$$\begin{cases} \dfrac{\mathrm{d}x_c(s)}{\mathrm{d}s} = u\left(x_c(s), s\right), \quad s \in \left[t_n, t_n + \alpha^n_{i+1/2}\Delta t\right], \\ x_c\left(t_n + \alpha^n_{i+1/2}\Delta t\right) = x_{i+1/2}, \end{cases} \tag{3.17}$$

where u is the velocity of the fluid flow. Note that $x_c(s)$ is the departure point at time s of a particle that will arrive at the gridpoint $x_{i+1/2}$ in time $t_n + \alpha^n_{i+1/2}\Delta t$, with $\alpha^n_{i+1/2}$ is a parameter less than 1, that controls the temporal grid, see Figure 4.3; the choice of $\alpha^n_{i+1/2}$ is discussed in subsection 3.3.3. The method of characteristics does not follow the flow particles forward in time, as the Lagrangian schemes do; instead, it traces backwards the position at time t_n of particles that will reach the points of a fixed mesh at time $t_n + \alpha^n_{i+1/2}\Delta t$. Therefore, the method avoids the grid distortion difficulties that the conventional Lagrangian schemes have. Hence, the solution of (3.17) can be expressed in an integral form as

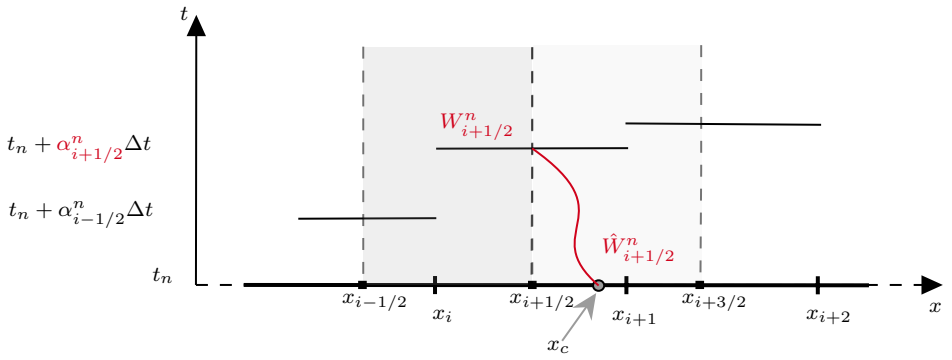

Figure 3.1: Sketch of the method of characteristics: A fluid particle at gridpoint $x_{i+1/2}$ is traced back in time to x_c.

$$x_c\left(t_n\right) = x_{i+1/2} - \int_{t_n}^{t_n + \alpha^n_{i+1/2}\Delta t} u\left(x_c(s), s\right) ds. \tag{3.18}$$

The integral in (3.18) can be computed numerically using a quadrature method, which generally leads to a non-linear equation in $x_c(t_n)$. A root-finding algorithm is subsequently required to solve this equation. In our simulations, we used a quadrature method of order 0 which gives us

$$x_c\left(t_n\right) = x_{i+1/2} - \alpha^n_{i+1/2}\Delta t u\left(x_c(t_n), t_n\right) \tag{3.19}$$

then we used the fixed point method to solve equation (3.19). Thus, once the characteristic curves $x_c\left(t_n\right)$ are accurately calculated, the intermediate solutions $\mathbf{W}^n_{i+1/2}$ of a generic function $\mathbf{W}(x_{i+1/2}, t_n + \alpha^n_{i+1/2}\Delta t)$ are reconstructed using

$$\mathbf{W}^n_{i+1/2} = \widehat{\mathbf{W}}^n_{i+1/2} + \int_{t_n}^{t_n + \alpha^n_{i+1/2}\Delta t} \mathbf{G}\left(\mathbf{W}\left(x_c(s), s\right)\right) ds, \tag{3.20}$$

where $\widehat{\mathbf{W}}^n_{i+1/2} = \mathbf{W}\left(x_c\left(t_n\right), t_n\right)$ are the solutions at the characteristic foot computed by interpolation from the gridpoints of the control volume where the departure points reside, see Figure 3.1 for an illustration. For instance, linear-based interpolation polynomials can be

formulated component by component as

$$\widehat{\mathbf{W}}^n_{i+1/2} = \mathbf{W}^n_i + \frac{\mathbf{W}^n_{i+1} - \mathbf{W}^n_i}{\Delta x}\Big(x_c(t_n) - x_i(t_n)\Big), \tag{3.21}$$

Note that another polynomial interpolation can be used for smooth solutions. However, we have noticed that there is no significant improvement if we change the order of interpolation. This is justified by the fact that the information about the characteristic curve $x_c(t_n)$, which lies between cell i and $i+1$, is given by these cells. Due to the approximation of the integral in equation (3.20) by the rectangle method, the numerical fluxes in (3.13) are reconstructed using

$$\mathbf{W}^n_{i+1/2} = \widehat{\mathbf{W}}^n_{i+1/2} + \alpha^n_{i+1/2}\Delta t\mathbf{G}(\widehat{\mathbf{W}}^n_{i+1/2}), \tag{3.22}$$

such that the derivatives it contains $\mathbf{G}$ are calculated by a finite difference between cells i and $i+1$ for the interface $i+1/2$.
Finally, the FVC scheme with the diffusion control parameter $\alpha^n_{i+1/2}$ can be written as fellows

$$\mathbf{W}^{n+1}_i = \mathbf{W}^n_i - \frac{\Delta t}{\Delta x}\Big(\mathbf{F}\Big(\mathbf{W}^n_{i+1/2}\Big) - \mathbf{F}\Big(\mathbf{W}^n_{i-1/2}\Big)\Big), \tag{3.23}$$

where $\mathbf{W}^n_{i\pm1/2}$ are calculated using (3.22), and $\mathbf{F}$ is the physical flux given in (3.2). The process to compute $\alpha^n_{i+1/2}$ will be discussed in the following section.

3.3.3 Control parameter $\alpha^n_{i+1/2}$

The choice of the control parameter is based on the stability analysis presented by Benkhaldoun and Seaïd in [16]. This analysis leads us to propose a control parameter $\alpha^n_{i+1/2}$ calculated locally and at each time step with the following formula,

$$\alpha^n_{i+1/2} = \tilde{\alpha}_{i+1/2} + \left(\frac{1}{2} - \tilde{\alpha}_{i+1/2}\right)\phi(r_{i+1/2}) \tag{3.24}$$

where

$$\tilde{\alpha}_{i+1/2} = \frac{\Delta x}{2\Delta t S_{i+1/2}}, \quad \text{and} \quad S_{i+1/2} = \max_k\left(\max_i\left(\left|\lambda^k_i\right|, \left|\lambda^k_{i+1}\right|\right)\right) \tag{3.25}$$

here λ^k_i is the k^{th} eigenvalue of (4.12), $S_{i+1/2}$ is the local Rusanov speed and $\phi(r_{i+1/2})$ is a slope limiter. The results, presented in Section 3.4, were obtained using the Minmod limiter; note that other slope limiters functions can be used, as van Albada function. The ratio $r_{i+1/2}$ is given by

$$r_{i+1/2} = \frac{q_i - q_{i-1}}{q_{i+1} - q_i} \tag{3.26}$$

where

$$q_i = \max_i\left(\left|u_i + \frac{2c_i}{\gamma - 1}\right|, \left|u_i - \frac{2c_i}{\gamma - 1}\right|\right), \tag{3.27}$$

and

$$\phi(r) = \max(0, min(1, r)), \qquad \lim_{r\to\infty}\phi(r) = 1 \tag{3.28}$$

we note that if $\phi = 1$, we have $\alpha^n_{i+1/2} = \frac{1}{2}$ and as proved in [16, Lemma. 3.2] the method is a second-order scheme. On the other hand, when $\phi = 0$, then $\alpha^n_{i+1/2} = \tilde{\alpha}_{i+1/2}$ which, combined with (4.27), give us a stable and TVD scheme (thanks to Lemma 2.2 [16]).

3.3.4 The FVC Algorithm

In summary, below is the algorithm of the FVC method with the local diffusion parameter

Algorithm 1 FVC method for compressible Euler equations

$\mathbf{W} = (\rho, \rho u, E)$;
Initialize conditions;
for each time iteration **do**
  Compute the time step Δt;
  Compute $\alpha^n_{i+1/2}$ for all interfaces; /*Using formula (3.24)*/
  Compute $x_c(t_n)$; /*Using formula (3.18)*/
  Compute $\mathbf{W}^n_{i+1/2}$ for all interfaces; /*Using formula (3.22)*/
  Compute the solution $\mathbf{W}^{n+1}$; /*Using formula (3.23)*/
  Update the solution: $\mathbf{W}^{n+1} \leftarrow \mathbf{W}^n$;
  Apply boundary conditions;
end for

3.4 Numerical results and discussions

In order to evaluate the accuracy, performance, and robustness of our method, we applied it to Euler equations (3.2) with a series of numerical tests. In this chapter, we consider a perfect gas with a specific heat ratio $\gamma = 1.4$. The computational domain is $\Omega = [0, 1]$, and the boundary conditions are transmissive. The exact solutions are performed using the open-source code [19].

We compare our results with those given by Rusanov [60], Roe [57], and HLL [36] methods. For time discretization, we use a first-order Euler scheme, and the time step Δt is adjusted according to the following CFL condition

$$\Delta t = Cr \frac{\Delta x}{\max_i \left(\sqrt{2\alpha^n_{i+1/2}} \Lambda^n_i \right)} \tag{3.29}$$

where Cr is the Courant number and $\Lambda_i = \max_k(|\lambda^k_i|)$ is the spectral radius of the Euler equations.

3.4.1 Sod shock tube

Sod shock tube problem [63] with a sonic point in rarefaction is one of the most important tests since it evaluates the satisfaction of the entropy property of numerical methods. The solution to this problem consists of a right shock wave, a right traveling contact discontinuity wave, and a left sonic rarefaction wave [65]. The initial condition is defined as

$$\begin{cases} \rho^0(x < 0.5) = 1, \\ u^0(x < 0.5) = 0.75, \\ p^0(x < 0.5) = 1, \end{cases} \quad \text{and} \quad \begin{cases} \rho^0(x \geq 0.5) = 0.125, \\ u^0(x \geq 0.5) = 0, \\ p^0(x \geq 0.5) = 0.1\cdot \end{cases} \tag{3.30}$$

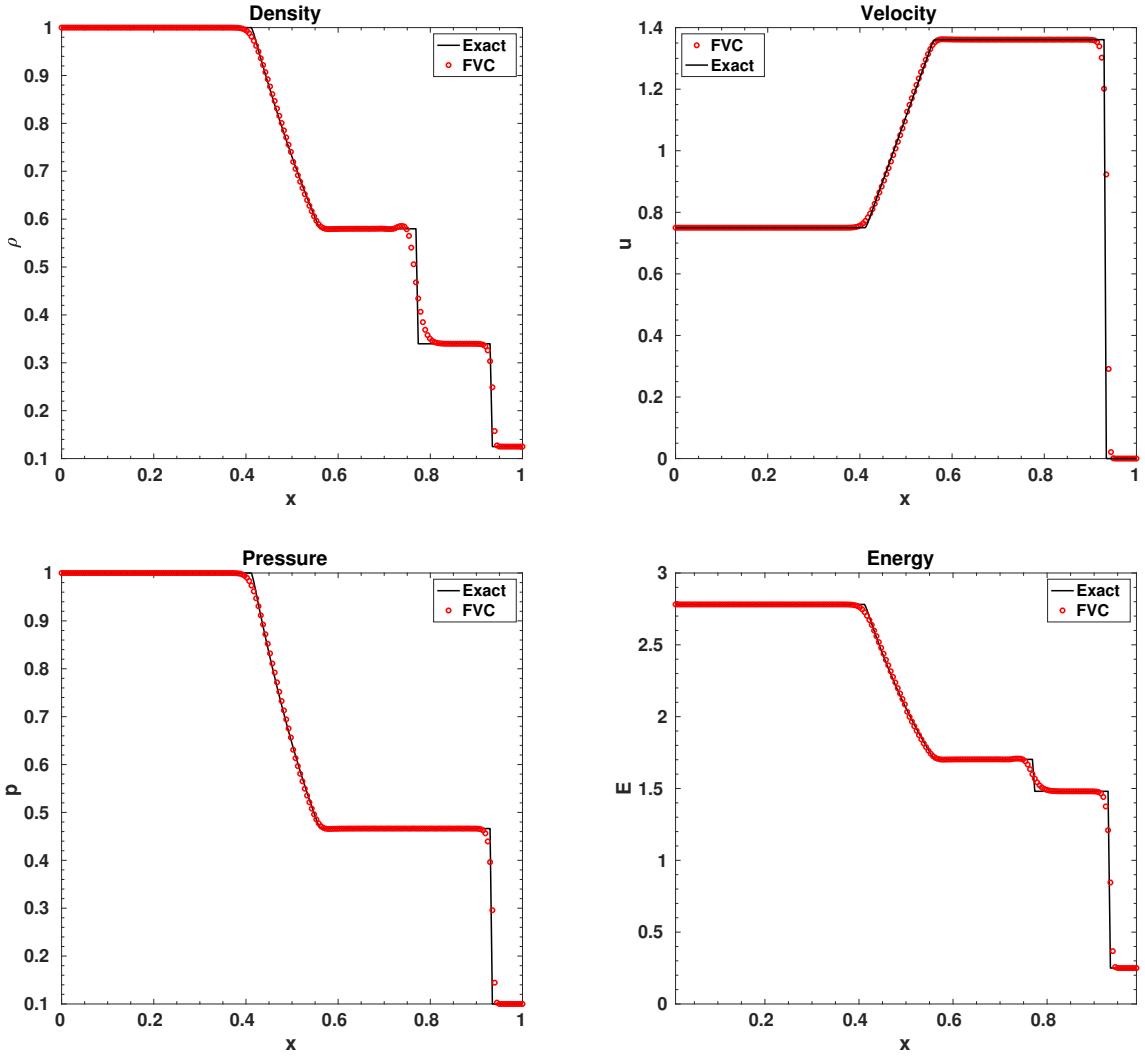

FIGURE 3.2: Sod shock tube: density ρ (top left), velocity u (top right), pressure p (bottom left) and total energy E (bottom right) at time $t = 0.2s$ with 200 regular cells.

The numerical results presented in this section were calculated with 200 cells and Cr= 0.8. In Figure 3.2, we compare our method to the exact solution at time $t = 0.2s$.

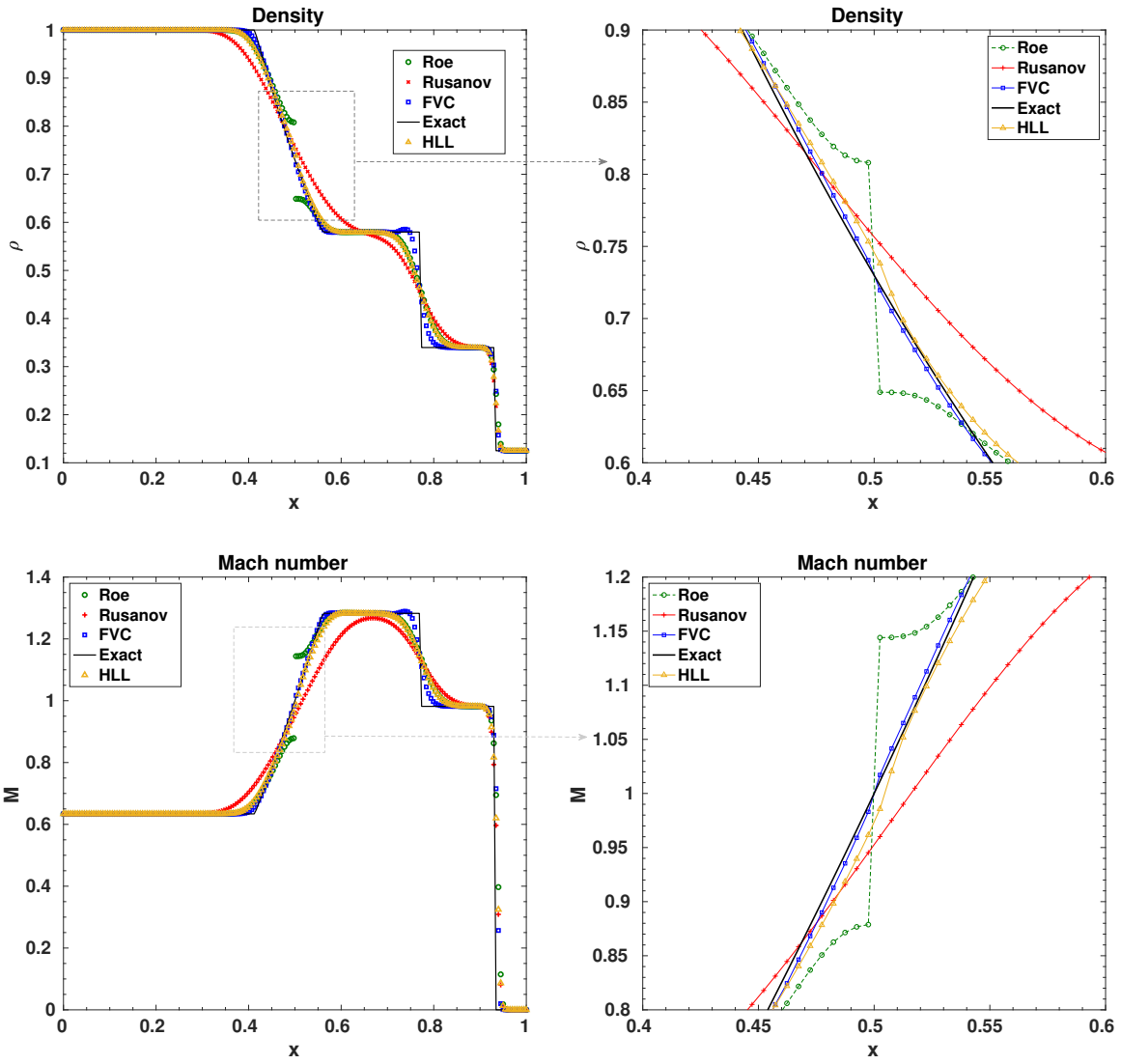

Figure 3.3: Sod shock tube: density ρ (top left), a zoom on ρ around the sonic point (top right), Much number M (bottom left) and a zoom on M around the sonic point (bottom right) at time $t = 0.2s$ with 200 regular cells.

We note that the shock, the contact, and the rarefaction are correctly captured. Figure 3.3 shows a comparison between our method, Roe scheme, HLL, and Rusanov schemes. It is clear that our method is more accurate. Another essential advantage of the FVC scheme is that it perfectly approximates the rarefaction wave, including the sonic point, which is not the case for the Roe scheme, where the entropy problem appears. The same error has been observed in [65, p. 227] for the Godunov scheme and other schemes (see [65, p. 280]).

Figure 3.4 represents the behavior of FVC scheme in respect to the choice of $\alpha^n_{i+1/2}$. It is clear that choosing $\alpha^n_{i+1/2} = \frac{1}{2}$ implies the creation of oscillations. On the other hand, choosing $\alpha^n_{i+1/2} = 1$ gives a stable scheme, but the results are more diffused than the case of a

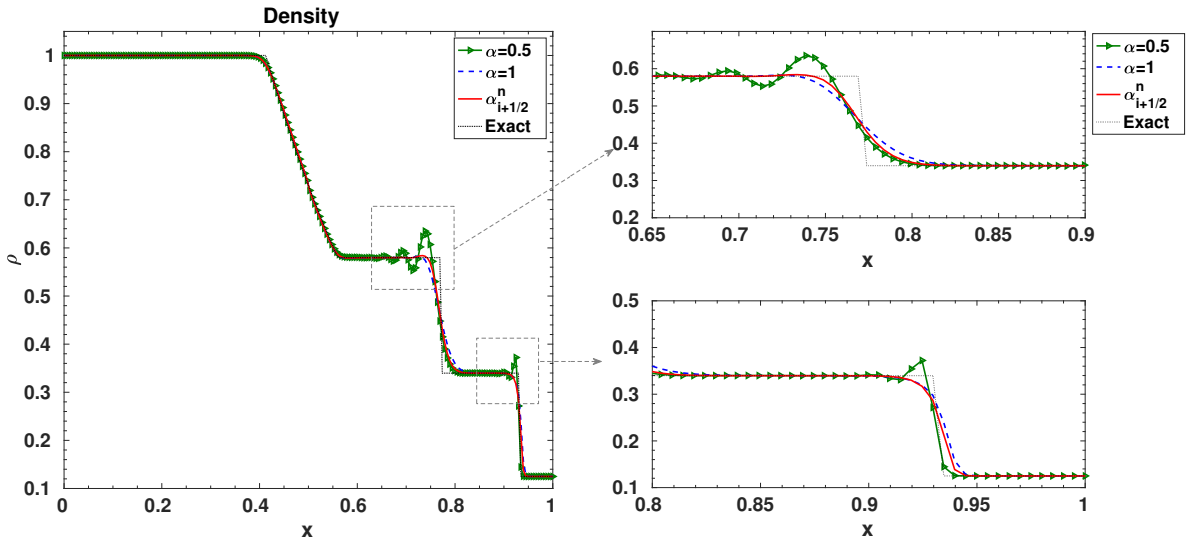

FIGURE 3.4: Sod shock tube: numerical solution profile according to the choice of the parameter $\alpha^n_{i+1/2}$ at time $t = 0.2s$ with 200 regular cells.

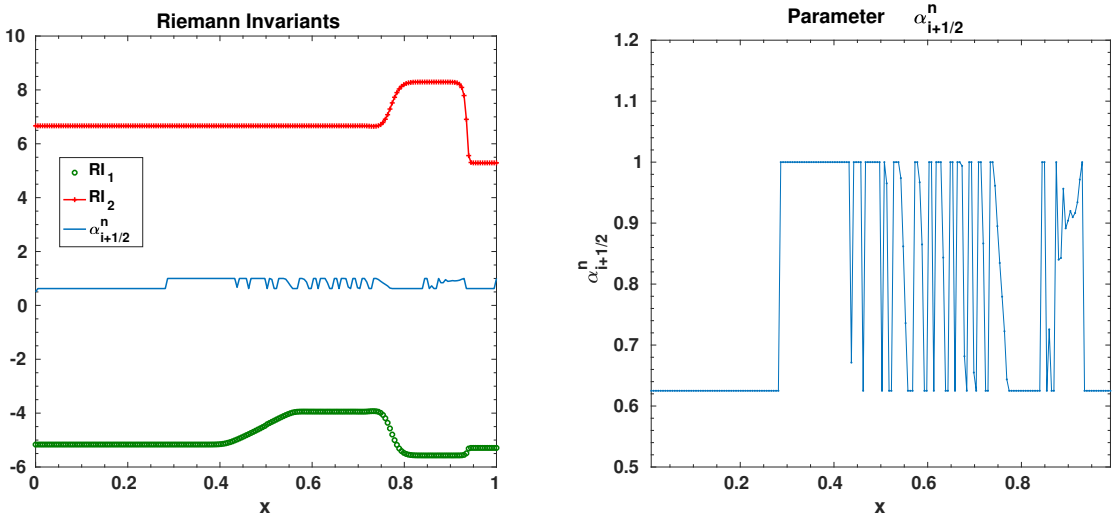

FIGURE 3.5: Sod shock tube: Riemann invariant (left) and parameter $\alpha^n_{i+1/2}$ (right) at time $t = 0.2s$ with 200 regular cells.

variable $\alpha^n_{i+1/2}$. These numerical results are consistent with our comments in section (3.3) on the reason behind the choice of the control parameter $\alpha^n_{i+1/2}$.

In Figure 3.5 we plot the Riemann invariants (left) and the variations of $\alpha^n_{i+1/2}$ computed using Riemann invariants (right), this figure shows us that $\alpha^n_{i+1/2}$ is involved in the area where the shock, the rarefaction and the contact discontinuity appear.

In Table 3.1 and Figure 3.6, we compare the L^1 error for the shock tube problem using

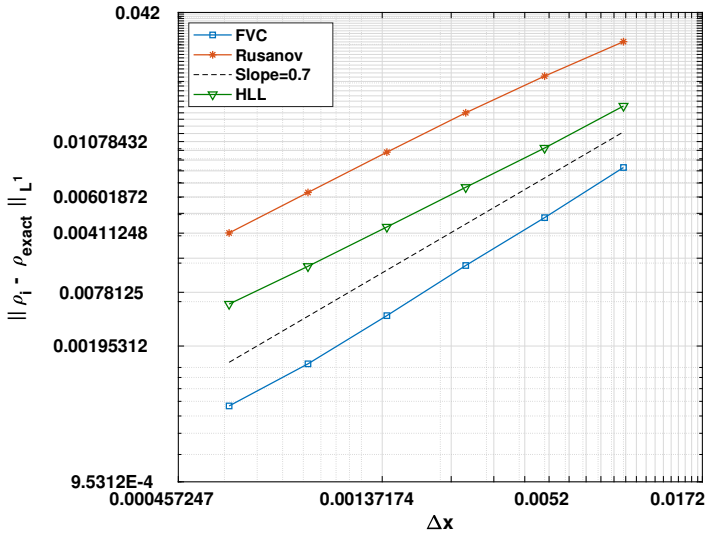

Figure 3.6: L^1 error plot (logarithmic scales) for Sod shock problem at time $t = 0.2s$.

different schemes. This table confirms what we said previously about the accuracy of the FVC method compared to the Rusanov scheme, HLL scheme, and a modified Roe scheme. The convergence rate for our method is close to 0.77 while it is equal to 0.59, 0.60 and 0.58 for Roe, HLL and Rusanov respectively.
In Table 3.2, we present the computational times for each method. As shown in this table, our method is faster than other schemes, which is one of the most important advantages of our method.

Table 3.1: Sod shock tube: L^1-error for the density at time $t = 0.2s$.

Mesh	Rusanov		Roe*		HLL		FVC	
	Error	Order	Error	Order	Error	Order	Error	Order
100	3.0879e-2	-	1.5499e-2	-	1.5683e-2	-	7.7572e-3	-
200	2.1485e-2	0.5233	1.0066e-2	0.6226	1.0076e-2	0.6382	4.4211e-3	0.8111
400	1.4603e-2	0.5571	6.6070e-3	0.6075	6.6654e-3	0.5962	2.6685e-3	0.7284
800	9.6443e-3	0.5986	4.3727e-3	0.5954	4.3878e-3	0.6032	1.5500e-3	0.7837
1600	6.3116e-3	0.6117	2.8986e-3	0.5932	2.9005e-3	0.5972	8.8431e-4	0.8097
3200	4.1210e-3	0.6150	1.9484e-3	0.5731	1.9492e-3	0.5734	5.3636e-4	0.7213

*Roe with Harten entropy correction [35] with $\delta = 10^{-2}$.

3.4.2 Vacuum test

We now turn to the well-known vacuum test, which is used to evaluate the performance of numerical methods for low-density flows. The solution consists of two symmetric rarefaction waves and a stationary contact discontinuity. This problem can be found in [65], and the initial conditions are

Table 3.2: Computational times in seconds for Sod shock tube problem.

Gridpoints	Rusanov	Roe*	HLL	FVC
100	0.19	0.55	0.203	0.208
200	0.821	2.22	0.821	0.86
400	3.26	9.10	3.33	3.14
800	13.11	36.84	13.35	11.83
1600	53.52	145.38	54.74	46.05
3200	210.662	585.17	217.69	181.34

Note: The CPU time was measured on Intel(R) Xeon(R) Silver 4210 CPU @ 2.20GHz processor.
*Roe with Harten entropy correction [35] with $\delta = 10^{-2}$.

$$\begin{cases} \rho^0(x < 0.5) = 1, \\ u^0(x < 0.5) = -2.0, \\ p^0(x < 0.5) = 0.4, \end{cases} \quad \text{and} \quad \begin{cases} \rho^0(x \geq 0.5) = 1, \\ u^0(x \geq 0.5) = 2.0, \\ p^0(x \geq 0.5) = 0.4\cdot \end{cases} \tag{3.31}$$

In Figure 3.7, we compare the FVC scheme to the numerical solution computed with the Rusanov method, HLL method, and to the exact solution with 200 regular cells and Cr=0.8 at $t = 0.15s$. The rarefaction waves are captured, and we note that in the contact wave zone, where density and pressure are close to zero, the results are acceptable, and , we notice that the positivity of the solution is numerically preserved under the CFL condition (4.27). We recall that the Roe scheme fails on this problem, but a modified version can be used (see, for example, Einfeldt et al. [30]).

In Figure 3.8, we present the variations of $\alpha^n_{i+1/2}$ (right) and the Riemann invariants (left); this figure shows us that $\alpha^n_{i+1/2}$ adapts itself where the stationary discontinuity appears which give us a good approximation of the velocity profile in this zone.

3.4.3 Robustness test

In this section, we will perform the robustness of our method using two benchmarks; these tests were proposed in [65]. The first one consists of a strong right shock wave, a contact discontinuity, and a left rarefaction wave, and we have:

$$\begin{cases} \rho^0(x < 0.5) = 1, \\ u^0(x < 0.5) = 0, \\ p^0(x < 0.5) = 1000, \end{cases} \quad \text{and} \quad \begin{cases} \rho^0(x \geq 0.5) = 1, \\ u^0(x \geq 0.5) = 0, \\ p^0(x \geq 0.5) = 0.01. \end{cases} \tag{3.32}$$

The second test consists of a strong left shock wave, a contact discontinuity, and a right rarefaction wave; the initial conditions are

$$\begin{cases} \rho^0(x < 0.5) = 1, \\ u^0(x < 0.5) = 0, \\ p^0(x < 0.5) = 0.01, \end{cases} \quad \text{and} \quad \begin{cases} \rho^0(x \geq 0.5) = 1, \\ u^0(x \geq 0.5) = 0, \\ p^0(x \geq 0.5) = 100. \end{cases} \tag{3.33}$$

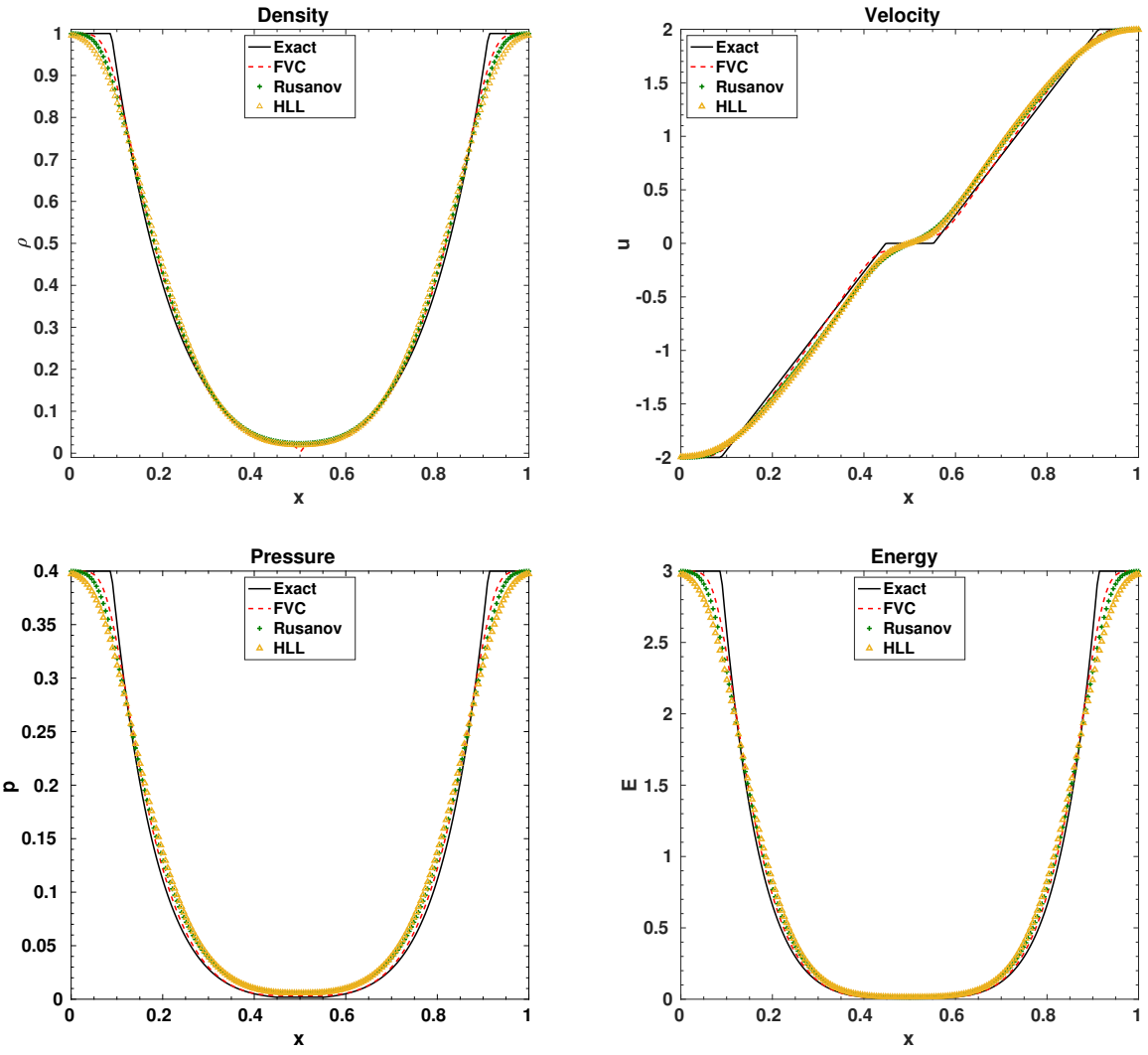

Figure 3.7: Vacuum test: density ρ (top left), velocity u (top right), pressure p (bottom left) and total energy E (bottom right) at time $t = 0.15s$ with 200 regular cells.

In Figure 3.9 we present the numerical solutions of Euler equations with initial data (3.32) obtained by FVC scheme, Roe scheme, HLL scheme and by Rusanov scheme with 2000 grid cells at time t=0.012s. All schemes show a correct agreement with the exact solution but as we can see in the density curve (left top), FVC scheme is more accurate on the contact discontinuity.

Figure 3.10 shows the numerical solutions of Euler equations with initial data (3.33) obtained by FVC scheme, Roe scheme, HLL and by Rusanov scheme with 2000 cells at time $t = 0.035s$. The difference between this problem and the previous one, is that the velocity is negative. As in Figure 3.9, we note that our method captured the contact discontinuity better than other schemes.

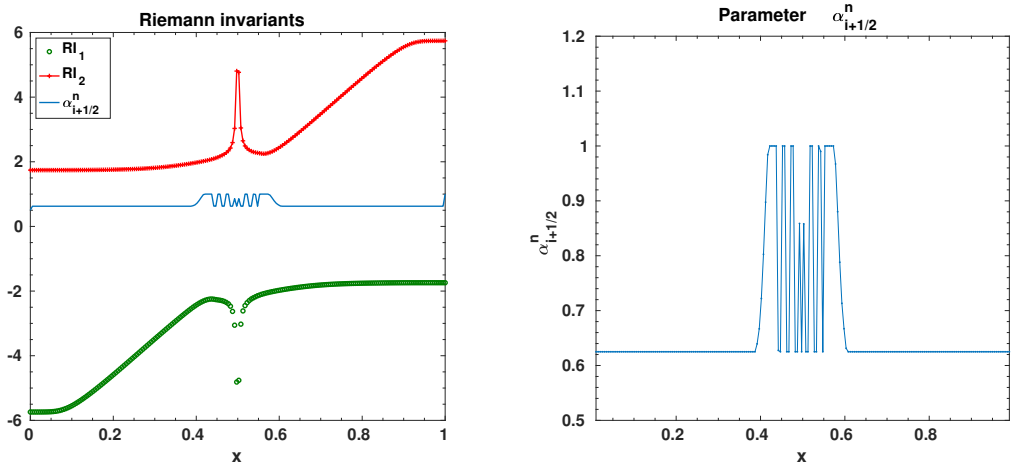

FIGURE 3.8: Vacuum test: Riemann invariant (left) and parameter $\alpha^n_{i+1/2}$ (right) at time $t = 0.15$ s with 200 regular cells.

3.4.4 A low-speed contact discontinuity

In this section, we check the ability of our method to resolve slowly–moving contact discontinuities and also a stationary contact discontinuity. Toro et al. [65] proposed two problems; the first one corresponds to an isolated stationary contact wave and the initial data is given by

$$\begin{cases} \rho^0(x < 0.5) = 1.4, \\ u^0(x < 0.5) = 0, \\ p^0(x < 0.5) = 1, \end{cases} \quad \text{and} \quad \begin{cases} \rho^0(x \geq 0.5) = 1, \\ u^0(x \geq 0.5) = 0, \\ p^0(x \geq 0.5) = 1\cdot \end{cases} \tag{3.34}$$

The second one corresponds to an isolated contact moving slowly to the right, where the initial data is

$$\begin{cases} \rho^0(x < 0.5) = 1.4, \\ u^0(x < 0.5) = 0.1, \\ p^0(x < 0.5) = 1, \end{cases} \quad \text{and} \quad \begin{cases} \rho^0(x \geq 0.5) = 1, \\ u^0(x \geq 0.5) = 0.1, \\ p^0(x \geq 0.5) = 1\cdot \end{cases} \tag{3.35}$$

Figure 3.11 and Figure 3.12 show the numerical results obtained by FVC, HLL, Roe, and Rusanov, compared to the exact solution with 200 cells at time t=2s. In Figure 3.11, we can see that the numerical results obtained by our method are very similar to those obtained by Roe scheme, where the contact is perfectly captured unlike the Rusanov scheme and HLL who diffuse. For the slow-moving contact test (3.35), we remark on the density curve that our method is more accurate than Roe, HLL and Rusanov. For the velocity, which is supposed to be constant, there is a small oscillation that appears in all numerical solutions but is smaller in the case of FVC we mention that for this sensitive benchmark, we used a constant $\alpha^n_{i+1/2}$.

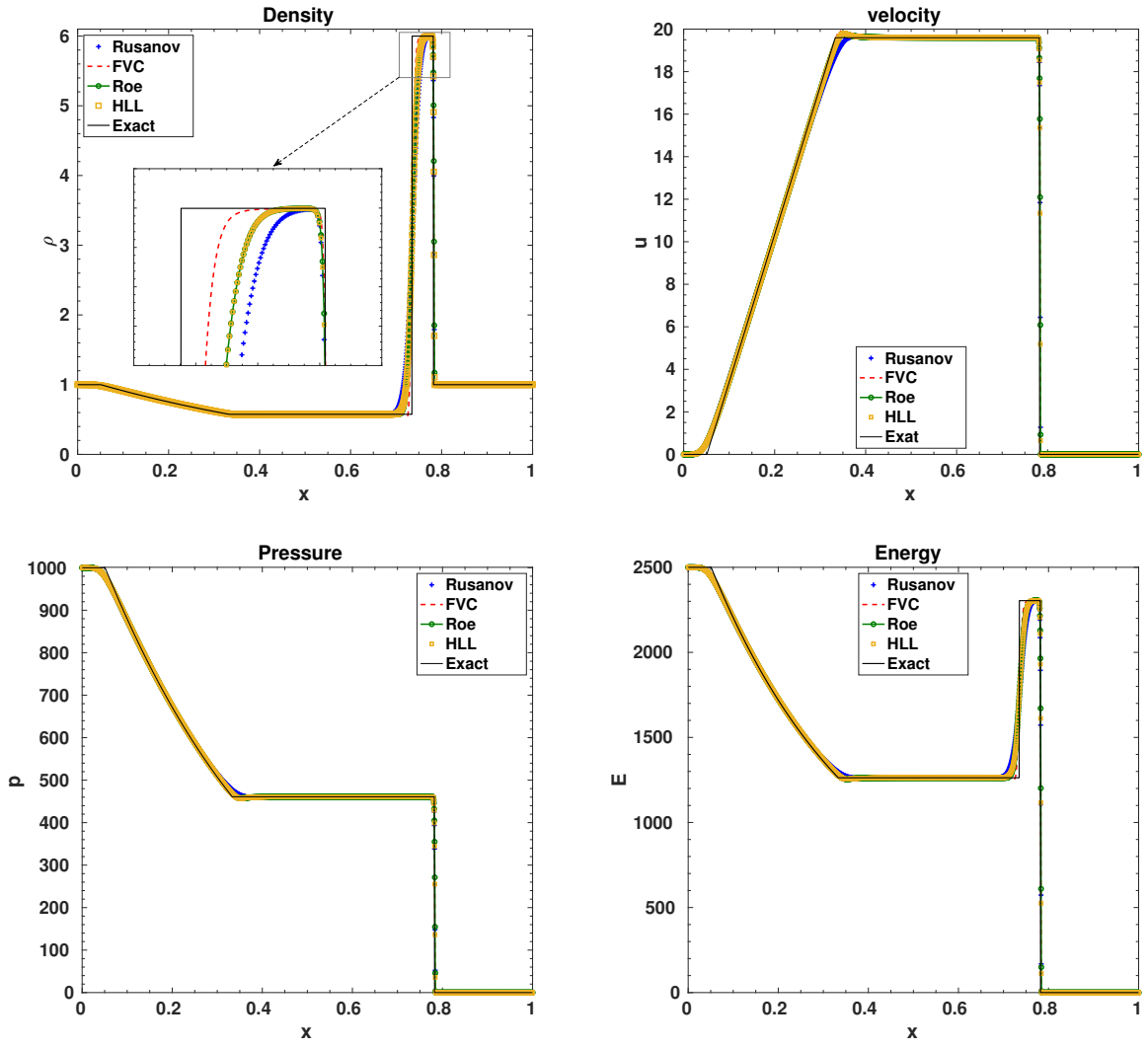

Figure 3.9: Robustness test: density ρ (top left), velocity u (top right), pressure p (bottom left) and total energy E (bottom right) at time $t = 0.012s$ with 2000 regular cells.

3.5 Conclusions and outlook

In this work, we proposed an accurate finite volume method for solving hyperbolic problems with application to the one-dimensional Euler equations. This method does not need the Jacobian matrix or solving a Riemann problem, which makes it a simple method to implement. The proposed method has been tested using several benchmarks; the results show the high accuracy of our method and, more specifically, its ability to capture contact discontinuities. An essential advantage of this method is that it converges to the entropic solution, i.e., the physical solution, without any entropic correction. Moreover, the method is fast and highly accurate.

In the next chapter, we will extend this method to multidimensional problems on unstructured meshes, with application to several physical problems.

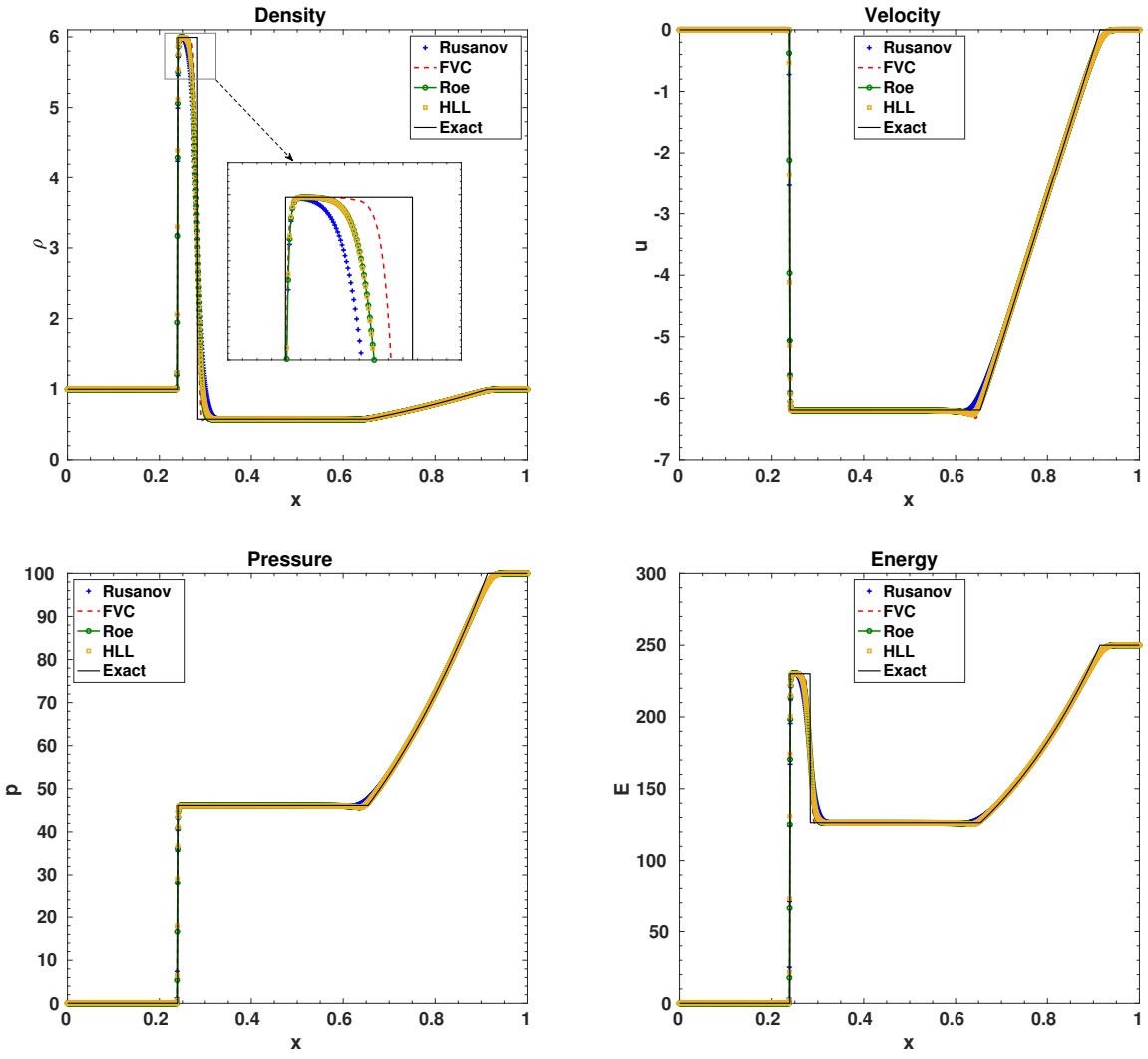

FIGURE 3.10: Robustness test: density ρ (top left), velocity u (top right), pressure p (bottom left) and total energy E (bottom right) at time $t = 0.035s$ with 2000 regular cells.

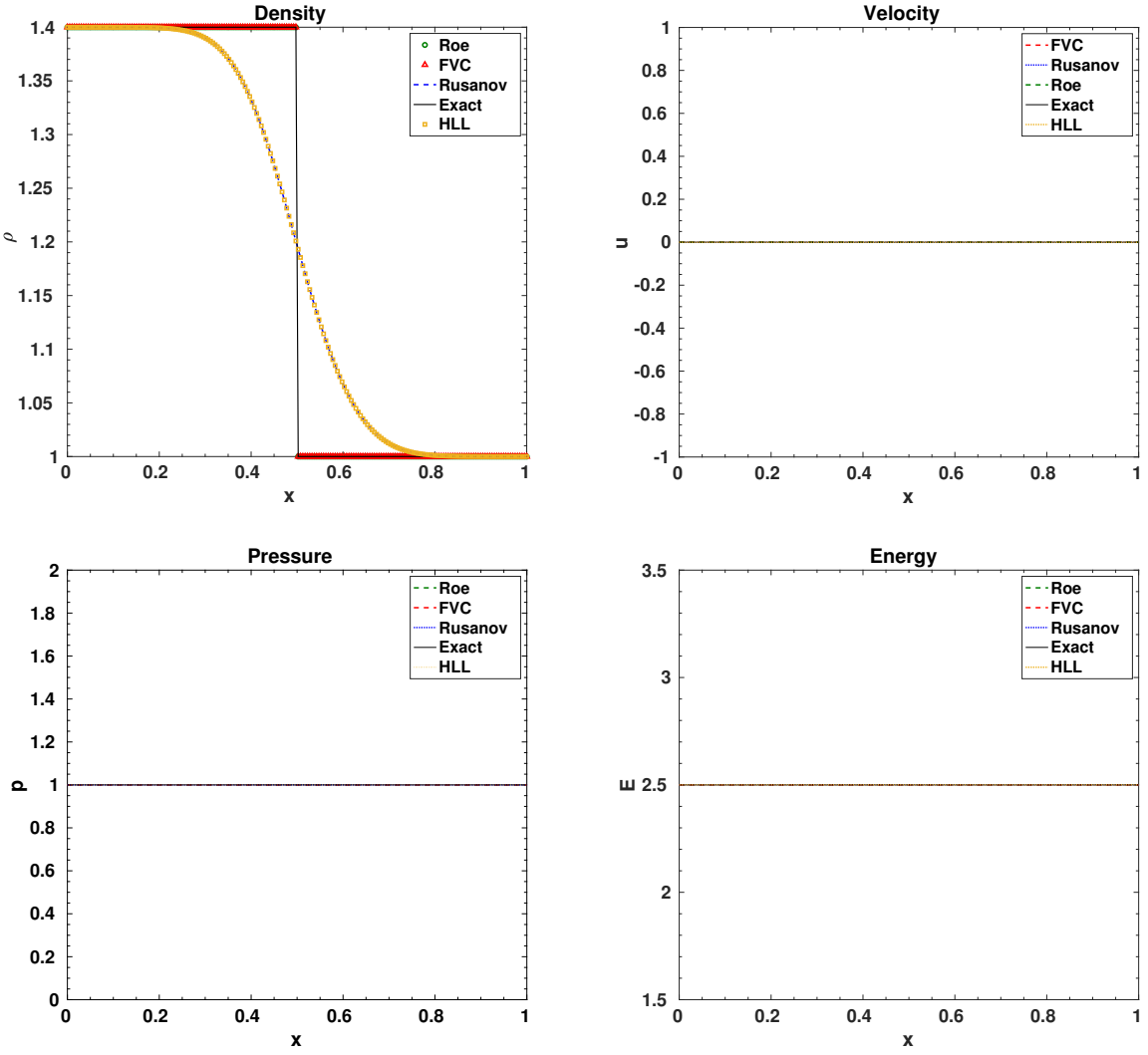

Figure 3.11: Stationary discontinuity test: density ρ (top left), velocity u (top right), pressure p (bottom left) and total energy E (bottom right) at time $t = 2.0s$ with 200 regular cells.

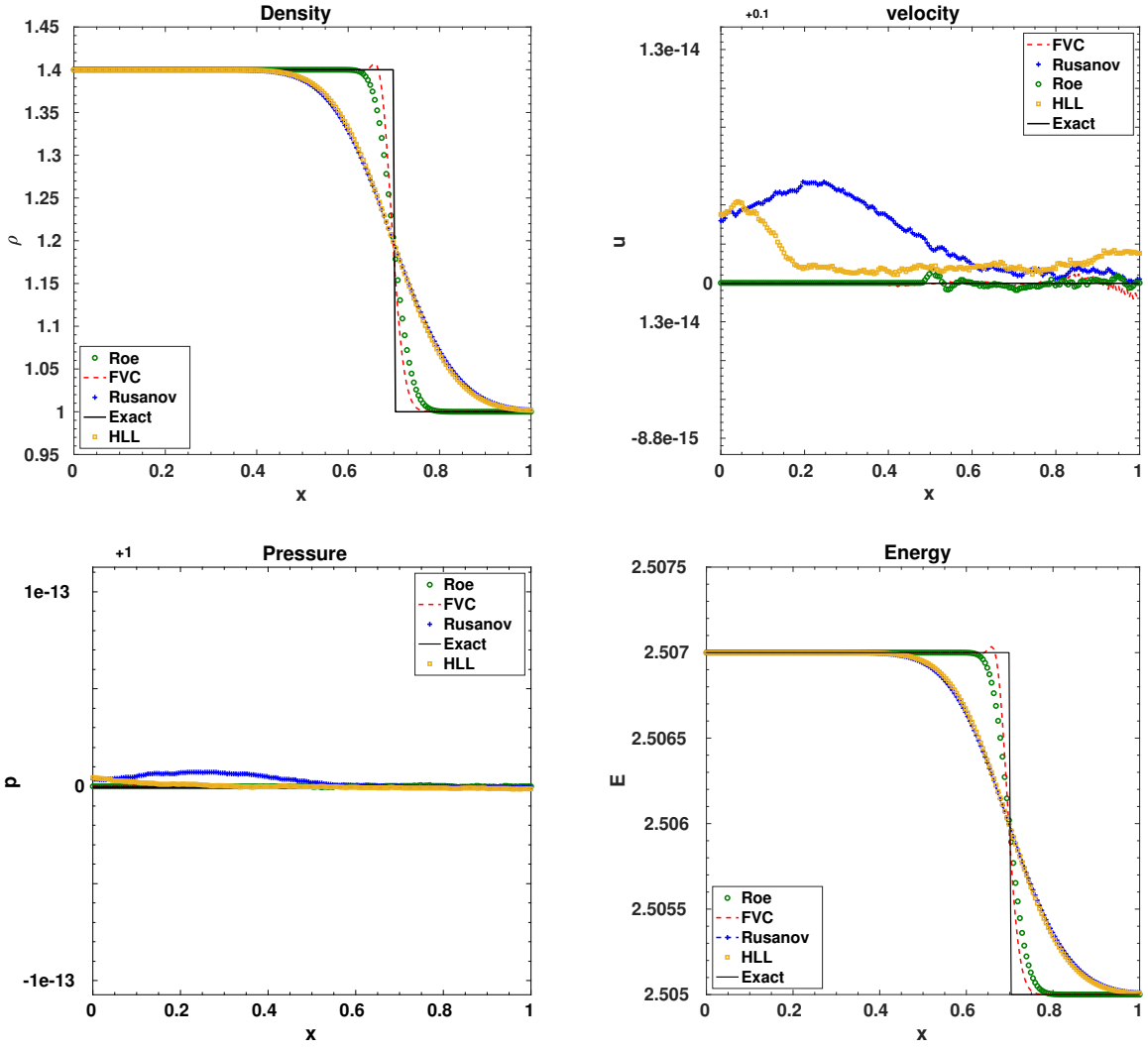

FIGURE 3.12: Low speed contact discontinuity test: density ρ (top left), velocity u (top right), pressure p (bottom left) and total energy E (bottom right) at time $t = 2.0s$ with 200 regular cells.

Chapter 4

A finite volume scheme with a diffusion control parameter on unstructured hybrid mesh: application to two-dimensional Navier Stokes problem

Contents

Abstract

This chapter presents a new approach to controlling the numerical diffusion in the finite volume characteristic (FVC) scheme. The approach is a generalization of the one-dimensional method proposed in the previews chapter, and it employs the backward method of characteristics to create interface states. The approach was evaluated using two-dimensional Navier-Stokes equations on unstructured hybrid meshes. The results demonstrate that the proposed approach is effective in controlling numerical diffusion and capturing the shock and the boundary layer.

4.1 Introduction

In recent years, computational fluid dynamics (CFD) has played a crucial role in various engineering and scientific applications, particularly in the modeling and simulating of complex flow phenomena. One of the essential components of CFD is the numerical scheme employed to solve the governing equations. The finite volume characteristics (FVC) scheme is a widely used method in this context, [16, 15, 72, 71] owing to its ability to provide accurate and efficient results.

Accurate simulation of supersonic flows, where fluid velocities exceed the speed of sound, is crucial for aerospace applications. One of the most famous examples of this type of flow is supersonic flow over a flat plate. The importance of this problem stems from the fact that the solutions for supersonic viscous flow over a flat plate could be extrapolated to derive parameters for high-speed flow over slender surfaces held at constant temperatures [29]. Viscous supersonic flow over a flat plate has been the subject of several studies [10, 31, 41]. Kalita et al. [41] present a rigorous study of the effect of numerical diffusion on the numerical solution of supersonic viscous flow over a flat plate.

In this chapter, we present a significant enhancement to the FVC scheme by introducing a control diffusion parameter. Unlike the initial version of the scheme, where α was a freely chosen constant. The new formulation α_{ij}^n (see section 4.3.1.1) depends on time and space, and is computed locally at each interface between cells i and j, thereby providing improved robustness and adaptability. This advancement paves the way for greater flexibility in handling complex computational scenarios with the FVC scheme, striking a balance between accuracy and computational efficiency ultimately leading to more reliable and insightful outcomes in the field of CFD.

In Section 2, we present the compressible Navier Stokes equation. Following this, Section 3 introduces the finite volume characteristics method, incorporating the diffusion control parameter for unstructured hybrid meshes. Section 4 is dedicated to the application of the proposed technique to Euler and Navier Stokes equations. Subsequently, numerical results and examples are showcased in Section 4, leading to a discussion on the accuracy and efficiency of the method. The chapter is concluded in Section 5 with conclusions and perspectives.

4.2 Governing equations

We consider The two-dimensional compressible Navier-Stokes equations for modeling the dynamics of viscous fluids. In the form presented hereafter, the variables retained to describe the conservation laws are the density ρ, the velocity vector $\mathbf{u} := (u, v)$, the total energy E, the temperature T and the pressure p

$$\begin{cases} \partial_t \rho + \nabla \cdot (\rho \mathbf{u}) = 0, \\ \partial_t (\rho \mathbf{u}) + \nabla \cdot (\rho \mathbf{u} \otimes \mathbf{u}) + \boldsymbol{\nabla} p + \nabla \cdot \tau = 0, \\ \partial_t (\rho E) + \nabla \cdot ((\rho E + p)\mathbf{u}) + \nabla \cdot (\tau \mathbf{u}) - \nabla \cdot (\kappa \boldsymbol{\nabla} T) = 0\cdot \end{cases} \tag{4.1}$$

The viscous stress tensor τ is given by

$$\tau = \frac{2}{3}\mu(\nabla \cdot \mathbf{u})\mathbf{I} - \mu\left(\nabla\mathbf{u} + \nabla\mathbf{u}^t\right). \tag{4.2}$$

For ideal gases, the energy of the system is related to these unknowns with the following state law

$$\frac{p}{\rho} = RT, \quad \rho E = \frac{1}{2}\rho|\mathbf{u}|^2 + \frac{p}{(\gamma - 1)}, \tag{4.3}$$

with γ is the ratio of specific heats, it is a constant that depends on the particular gas (e.g. $\gamma = 1.4$ for air), κ is the heat conduction, Pr is the Prandtl number, R is the gas constant and μ is viscosity coefficient.

To simplify the presentation of the mathematical model, we rewrite the system (4.1) in a conservative vector form

$$\partial_t \mathbf{W} + \nabla \cdot \mathbf{Fc}(\mathbf{W}) = \nabla \cdot \mathbf{Fd}(\mathbf{W}, \nabla\mathbf{W}), \tag{4.4}$$

where

$$\mathbf{W} = \begin{pmatrix} \rho \\ \rho u \\ \rho v \\ \rho E \end{pmatrix}, \qquad \mathbf{Fc}(\mathbf{W}) = \begin{pmatrix} \rho u & \rho v \\ \rho u^2 + p & \rho uv \\ \rho uv & \rho v^2 + p \\ u(\rho E + p) & v(\rho E + p) \end{pmatrix}, \tag{4.5}$$

$$\mathbf{Fd}(\mathbf{W}, \nabla\mathbf{W}) = \begin{pmatrix} 0 & 0 \\ \tau_{xx} & \tau_{xy} \\ \tau_{xy} & \tau_{yy} \\ u\tau_{xx} + v\tau_{xy} + \kappa\partial_x T & u\tau_{yx} + v\tau_{yy} + \kappa\partial_y T \end{pmatrix}. \tag{4.6}$$

With

$$\tau_{xx} = \mu\left(\frac{4}{3}\partial_x u - \frac{2}{3}\partial_y v\right), \quad \tau_{xy} = \mu\left(\partial_x v + \partial_x v\right) \quad and \quad \tau_{yy} = \mu\left(\frac{4}{3}\partial_y v - \frac{2}{3}\partial_x u\right).$$

4.3 Numerical method

In this section, we formulate the Finite Volume Characteristic scheme with a diffusion control parameter to solve equation (4.7). The method uses an unstructured hybrid mesh to facilitate grid generation for complex configurations of the computational domain. As mentioned in previous works [16, 71, 72], the method requires two steps and can be interpreted as a predictor-corrector following the first idea presented in [14]. In the predictor step, the method of characteristics is used to determine the intermediate values to evaluate the numerical flux, while in the correction step, a fully conservative solution is obtained.

In section (4.3.1), we outline the numerical approach proposed for the case of an Inviscid flow ($\mu = 0$). In this case the equation (4.1) reduces to the following form

$$\begin{cases} \partial_t \rho + \nabla \cdot (\rho \mathbf{u}) = 0, \\ \partial_t (\rho \mathbf{u}) + \nabla \cdot (\rho \mathbf{u} \otimes \mathbf{u}) + \boldsymbol{\nabla} p = 0, \\ \partial_t (\rho E) + \nabla \cdot (\mathbf{u}(\rho E + p)) = 0, \end{cases} \tag{4.7}$$

therefore, the conservative form (4.4) becomes

$$\partial_t \mathbf{W} + \nabla \cdot \mathbf{Fc}(\mathbf{W}) = 0, \tag{4.8}$$

Secondly, we examine the case of viscous flow, in section (4.3.2), by combining the FVC method and the diamond scheme. This approach requires a primal mesh for the convective flux and a diamond mesh for the diffusive flux (see Fig. 4.1).

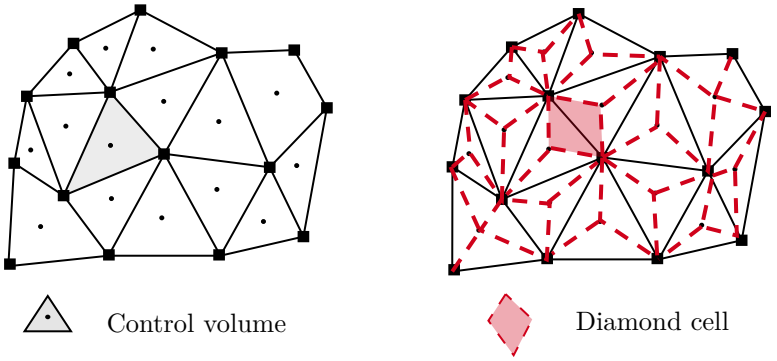

Figure 4.1: Primal mesh and control volumes (left) diamond mesh and diamond cell (right).

4.3.1 Inviscid flow

Suppose that the computational domain Ω is divided into a finite number of control volumes $\Omega = (\Omega_i)_{i \in I}$, with I a finite set of indices. We will further assume that the mesh is admissible in the finite volume discretization sense under cell-centered formulation [32, section 10.1]. Integrating equation (4.8) over a control volume Ω_i, gives the following integral system

$$\frac{d}{dt} \int \Omega_i \mathbf{W} dV + \int_{\partial \Omega_i} \mathbf{Fc}(\mathbf{W}) \cdot \mathbf{n} \, d\sigma = 0, \tag{4.9}$$

$\mathbf{n}$ is the normal vector to the edge $\partial \Omega_i$ of the cell Ω_i in the outward direction, dV and $d\sigma$ are respectively the surface element and the length element. According to the framework of the finite volume method, the semi-discrete equation associated with (4.8) is defined as

$$\frac{d\mathbf{W}_i}{dt} = -\frac{1}{|\Omega_i|} \sum_{j \in N_i} |\gamma_{ij}| \mathbf{\Phi}(\mathbf{W}_{ij}, \mathbf{n}_{ij}), \tag{4.10}$$

where

$$\mathbf{W}_i = \frac{1}{|\Omega_i|} \int \Omega_i \mathbf{W} dV, \quad \text{and} \quad \mathbf{\Phi}(\mathbf{W}_{ij}, \mathbf{n}_{ij}) \simeq \frac{1}{|\gamma_{ij}|} \int_{\gamma_{ij}} \mathbf{Fc}(\mathbf{W}) \cdot \mathbf{n}_{ij} d\sigma, \tag{4.11}$$

$\mathbf{W}_i$ represents the average quantity stored at the cell center of cell Ω_i. $\mathbf{W}_{ij}$ and $\mathbf{\Phi}(\mathbf{W}_{ij}, \mathbf{n}_{ij})$ refer to the intermediate state and the numerical flux, respectively, computed at the interface γ_{ij} between cells Ω_i and V_j.

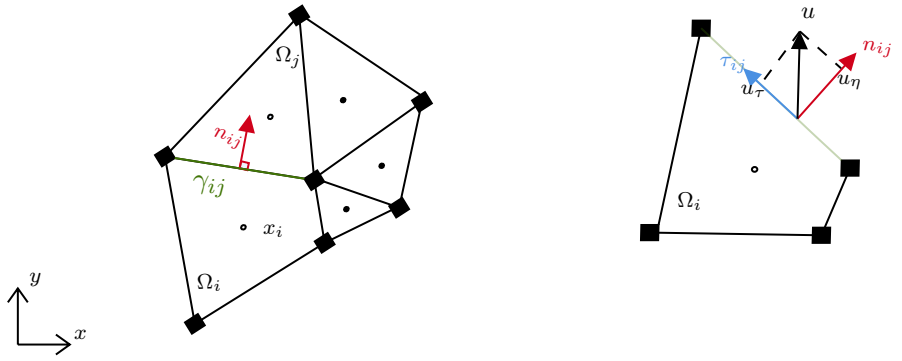

Figure 4.2: Generic control cells (left) and projected velocity frame (right).

In this paragraph, we set some notation:

- p_i: vertex of Ω_i,
- x_i: centroid of the cell Ω_i,
- γ_{ij}: boundary face between the cells Ω_i and V_j,
- $|\gamma_{ij}|$: length of γ_{ij},
- $|\Omega_i|$: volume of the cell Ω_i,
- $\partial\Omega_i$: boundary of the cell Ω_i,
- $\mathcal{P}_i$: the perimeter of the cell Ω_i.
- $\mathbf{n}_{ij}$: unit normal to γ_{ij}, outward to Ω_i such as, $\mathbf{n}_{ji} = -\mathbf{n}_{ij}$.

and N_i is the set of neighboring cells of the cell Ω_i. The spatial discretization of equation (4.10) is complete when a numerical construction of the flux $\mathbf{\Phi}(\mathbf{W}_{ij}, \mathbf{n}_{ij})$ is chosen. In general, this construction requires the solution of Riemann problems at the interfaces. From an algorithmic point of view, this procedure is very demanding. It may limit the application of the method when the solutions to the Riemann problem are complex or even impossible. This is why we have opted for constructing intermediate states $\mathbf{W}_{ij}$ using the method of characteristics, and the numerical flux is then calculated using the physical flux as $\mathbf{\Phi}(\mathbf{W}_{ij}, \mathbf{n}_{ij}) := \mathbf{Fc}(\mathbf{W}_{ij}) \cdot \mathbf{n}_{ij}$. The basic idea of this method is the imposition of a non-regular spatial grid at the subsequent temporal instance and retracing the flow paths to the preceding temporal instance.

To construct the intermediate states $\mathbf{W}_{ij}$, we first rewrite the system in an advection form. For this, we use a projected velocity model whose velocity components are projected onto the frame $\mathcal{R} = (\mathcal{V}_i; \vec{\tau}, \vec{\eta})$ (Fig. 4.2 right). The advection model we found is an equation whose solution we can calculate in an almost exact way. Let $\vec{\eta} := (n_x, n_y)^T$ be the unit outward normal to the edge of the cell Ω_i and $\vec{\tau} := (\tau_x, \tau_y)^T$ is the tangential vector, knowing that, $(\tau_x, \tau_y) = (-n_y, n_x)$. The projected velocity model associated with the Euler equations (4.8) is reformulated as (4.12), see [72, section 3.2.1].

$$\frac{\partial \mathbf{U}}{\partial t}(t, X) + u_\eta(t, X)\frac{\partial \mathbf{U}}{\partial \eta}(t, X) = \mathbf{S}(\mathbf{U}(t, X)), \tag{4.12}$$

where

$$\mathbf{U} = \begin{pmatrix} \rho \\ \rho u_\eta \\ \rho u_\tau \\ \rho E \end{pmatrix}, \qquad \mathbf{S}(\mathbf{U}) = \begin{pmatrix} -\rho \partial_\eta(u_\eta) \\ -\rho u_\eta \partial_\eta(u_\eta) - \partial_\eta p \\ -\rho u_\tau \partial_\eta(u_\eta) \\ -\rho E \partial_\eta(u_\eta) - \partial_\eta(p u_\eta) \end{pmatrix}. \tag{4.13}$$

$\mathbf{U}$ is the projected conservative unknown, u_η is the normal speed, and $\mathbf{S}(\mathbf{U})$ is the right-hand side that contains other terms of the system. The method of characteristics that is used traces the backward position at time t_n of a particle that will reach the gridpoint point $X_\star$ (arrival gridpoint) of a fixed mesh at time $t_n + \alpha_{ij}^n \Delta t$ (see Fig 4.3). The characteristic curves associated with (4.12) are the solutions of the following ODE.

$$\begin{cases} \dfrac{dX^c(t)}{dt} = u_\eta(t, X^c(t))\mathbf{n}, \quad t \in [t_n, t_n + \alpha_{ij}^n \Delta t], \\ X^c(t_n + \alpha_{ij}^n \Delta t) = X_\star. \end{cases} \tag{4.14}$$

A numerical integration method can calculate the solution (characteristic curves) of (4.14). Generally, the second-order methods lead to a non-linear equation in $X_c(t_n)$. A root-finding algorithm is subsequently required to solve this equation. Once the characteristic curves are

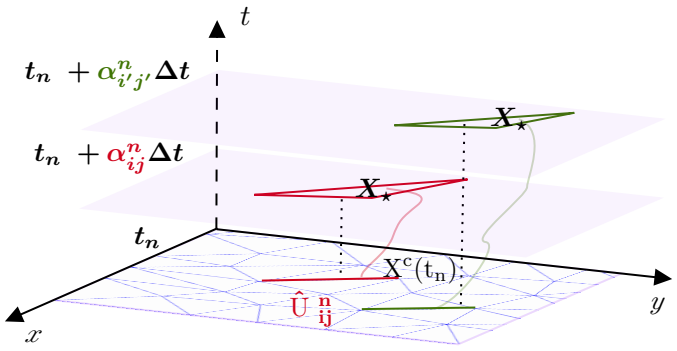

Figure 4.3: Sketch of the method of characteristics: A particle at $X_\star$ gridpoint is traced back in time to $X^c(t_n)$ where the intermediate solution $\hat{\mathbf{U}}_{ij}^n$ is interpolated.

identified, the advection equation (4.12) can be solved using

$$\mathbf{U}(t_n + \alpha_{ij}^n \Delta t, X_\star) = \mathbf{U}(t_n, X^c(t_n)) + \int_{t_n}^{t_n + \alpha_{ij}^n \Delta t} \mathbf{S}(\mathbf{U}(s, X^c(s)))\, ds. \tag{4.15}$$

The projected solution on the interface γ_{ij} is computed using the following formula

$$\mathbf{U}_{ij}^n = \hat{\mathbf{U}}_{ij}^n + \mathbf{I_F}(\hat{\mathbf{U}}_{ij}^n), \tag{4.16}$$

where $\mathbf{I_F}$ is the approximation of the integral in (4.15) and $\hat{\mathbf{U}}_{ij}^n = \sum_{k \in V(X^c)} \beta_k(X^c) \mathbf{U}_k^n$, with $V(X^c)$ is the neighbor set of all cells that share at less a vertex with the face γ_{ij} and $\beta_k(X^c)$ is the interpolation weight. The normal derivative terms in $\mathbf{S}$ are evaluated using the diamond scheme, see [72, section 3.2.3] for more details. The time discretization of the semi-discrete

equation (4.10) is based on an explicit scheme of order one. Let $t_n = n\Delta t$ with $t_0 = 0$ representing the initial time. If we denote $\mathbf{W}_j^n$ as the mean value in cell V_j of the solution at time t_n. The fully-discrete formulation of the equation (4.9) is given by

$$\mathbf{W}_i^{n+1} = \mathbf{W}_i^n - \frac{\Delta t}{|\Omega_i|} \sum_{j \in N_i} |\gamma_{ij}| \mathbf{\Phi}(\mathbf{W}_{ij}^n, \mathbf{n}_{ij}). \tag{4.17}$$

4.3.1.1 Local diffusion control parameter α_{ij}^n

In this section, we propose a control diffusion parameter that follows the same approach as the one we proposed for one-dimensional hyperbolic systems [5]. The objective of this chapter is to provide a simple way to extend this approach to the two-dimensional hyperbolic system. The construction of the diffusion control parameter is based on the analysis presented in [16]. On each cell Ω_i, we define the local diffusion control parameter α_i^n as follow

$$\alpha_i^n = \bar{\alpha}_i^n + \left(\frac{1}{2} - \bar{\alpha}_i^n\right) \psi_i \tag{4.18}$$

where

$$\bar{\alpha}_i^n = \max_{k \in N_i} \left(\frac{|\gamma_{ik}|}{2\Delta t S_{ik}}\right), \quad \text{and} \quad S_{ik} = \max_l \left(\max\left(\left|\lambda_i^l\right|, \left|\lambda_k^l\right|\right)\right) \tag{4.19}$$

here λ_i^l is the l^{th} eigenvalue of normal flux, and ψ_i is the Barth-Jespersen limiter function [12], we note that other limiter functions can be used. In this context, we have implemented a ratio that constrains the calculation involving Riemann invariants. Additional information can be found in [5]. Then the local diffusion control parameter for the interfaces is given by $\alpha_{ij}^n = \max(\alpha_i^n, \alpha_j^n)$.

4.3.2 Viscous flow

In this section, we explain how to use the FVC method with the diffusion control parameter for the Navier Stokes problem on an unstructured mesh. The integration of equation (5.43), gives

$$\frac{d}{dt} \int_{\Omega_i} \mathbf{W} dV + \frac{1}{|\Omega_i|} \sum_{j \in N_i} |\gamma_{ij}| \mathbf{\Phi}(\mathbf{W}_{ij}, \mathbf{n}_{ij}) = \frac{1}{|\Omega_i|} \sum_{j \in N_i} |\gamma_{ij}| \mathbf{\Psi}(\mathbf{W}_{ij}, \nabla \mathbf{W}_{ij}, \mathbf{n}_{ij}), \tag{4.20}$$

where $\mathbf{\Phi}(\mathbf{W}_{ij})$ is the approximation of the inviscid flux by the FVC method, $\nabla \mathbf{W}_{ij}$ is the gradient of $\mathbf{W}$ of at the interface γ_{ij} and $\mathbf{\Psi}(\mathbf{W}_{ij}, \nabla \mathbf{W}_{ij}, \mathbf{n}_{ij})$ is an approximation of $\mathbf{Fd}(\mathbf{W}, \nabla \mathbf{W}) \cdot \mathbf{n}$ at the interface γ_{ij}.

The construction of the numerical flux $\mathbf{\Psi}$ is based on the approximation of the gradient of velocity $\mathbf{u}$ and temperature T at the interface γ_{ij}. As mentioned in the introduction, we use the diamond scheme for the construction of these gradients and we have

$$\nabla \mathbf{u}_{ij} = \begin{pmatrix} {}^t(\nabla u_{ij}) \\ {}^t(\nabla v_{ij}) \end{pmatrix} = \frac{1}{2|\mathcal{D}_{ij}|} \begin{pmatrix} (u_S - u_N)\, {}^t n_{LR} \, |\gamma_{LR}| + (u_j - u_i)\, {}^t n_{ij} \, |\gamma_{ij}| \\ (v_S - v_N)\, {}^t n_{LR} \, |\gamma_{LR}| + (v_j - v_i)\, {}^t n_{ij} \, |\gamma_{ij}| \end{pmatrix}, \tag{4.21}$$

and

$$\nabla T_{ij} = \frac{1}{2|\mathcal{D}_{ij}|}\left(\left(T_S - T_N\right) n_{LR}\,|\gamma_{LR}| + \left(T_j - T_i\right) n_{ij}\,|\gamma_{ij}|\right), \tag{4.22}$$

where the values of $\mathbf{u}$ and T at the points S and N are represented by the variables $\mathbf{u}_S = (u_S, v_S)$ and $\mathbf{u}_N = (u_N, v_N)$ for the velocity and by T_S T_N for the temperature (see Figure 4.4) and they are computed using the least squares method.

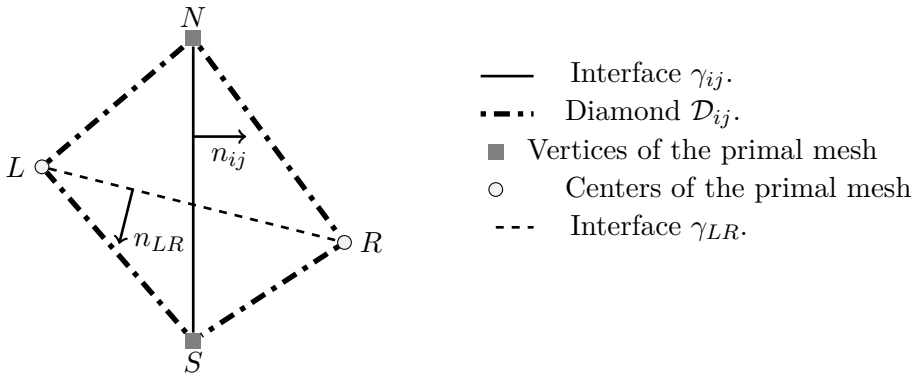

Figure 4.4: Diamond $\mathcal{D}_{ij}$ and notations.

$$\mathbf{\Psi}\left(\mathbf{W}_{ij}, \nabla\mathbf{W}_{ij}, \mathbf{n}_{ij}\right) = \begin{pmatrix} 0 & 0 \\ \tau_{xx}^{ij} & \tau_{xy}^{ij} \\ \tau_{xy}^{ij} & \tau_{yy}^{ij} \\ u_{ij}\tau_{xx}^{ij} + v_{ij}\tau_{xy}^{ij} + \kappa\partial_x T_{ij} & u_{ij}\tau_{yx}^{ij} + v_{ij}\tau_{yy}^{ij} + \kappa\partial_y T_{ij} \end{pmatrix} \cdot \mathbf{n}_{ij} \tag{4.23}$$

where

$$\mathbf{u}_{ij} = \frac{\mathbf{u}_i + \mathbf{u}_j}{2}, \quad \tau_{xx}^{ij} = \mu\left(\frac{4}{3}\partial_x u_{ij} - \frac{2}{3}\partial_y v_{ij}\right), \quad \tau_{xy}^{ij} = \mu\left(\partial_x v_{ij} + \partial_x u_{ij}\right)$$

and

$$\tau_{yy}^{ij} = \mu\left(\frac{4}{3}\partial_y v_{ij} - \frac{2}{3}\partial_x u_{ij}\right).$$

The fully-discrete formulation of the equation (4.1) is given by

$$\mathbf{W}_i^{n+1} = \mathbf{W}_i^n - \frac{\Delta t}{|\Omega_i|}\sum_{j\in N_i}|\gamma_{ij}|\mathbf{\Phi}(\mathbf{W}_{ij}^n, \mathbf{n}_{ij}) + \frac{1}{|\Omega_i|}\sum_{j\in N_i}|\gamma_{ij}|\mathbf{\Psi}(\mathbf{W}_{ij}, \nabla\mathbf{W}_{ij}, \mathbf{n}_{ij}). \tag{4.24}$$

4.3.3 Algorithm

In summary, below is the algorithm of FVC scheme with the local diffusion parameter α_{ij}^n for compressible Navier Stokes equation

Algorithm 2 FVC scheme for 2D compressible Navier Stokes equations

$\mathbf{W} = (\rho, \rho u, \rho v, \rho E)$;
Initialize conditions;
for each time iteration **do**
  Compute the time step Δt;
  Compute α_{ij}^n for the interface γ_{ik}
  Compute $X^c(t_n)$;
  Compute the projected solution $\mathbf{U}_{ij}^n$ on γ_{ij};
  Compute the discrete gradients $\nabla \mathbf{u}_{ij}$ and ∇T_{ij};
  Compute the solution $\mathbf{W}^{n+1}$ using (4.24);
  Update the solution: $\mathbf{W}^{n+1} \leftarrow \mathbf{W}^n$;
  Apply boundary conditions;
end for

4.4 Numerical results

In this section, we present numerical results for the Euler equation and the Navier Stokes equation. In both cases, the time steps are limited by a CFL condition. For Euler equation the time step Δt is given as follows

$$\Delta t = Cr \min_{i,j \in I} \left(\frac{\gamma_{ij}}{\sqrt{2\alpha_{ij}^n} \Lambda_{ij}^n} \right). \tag{4.25}$$

Cr is the Courant number and Λ_{ij} is the spectral radius of the normal flux.

For the compressible Navier-Stokes equation, Gassner et al. [49] propose to rewrite the diffusion flow using diffusion matrices, and they propose a hyperbolic time and parabolic time step.

$$\Delta t = Cr \frac{1}{\sqrt{\frac{1}{\Delta t_1^2} + \frac{1}{\Delta t_2^2}}}, \tag{4.26}$$

with

$$\Delta t_1 = \min_{i,j \in I} \left(\frac{\gamma_{ij}}{\sqrt{2\alpha_{ij}^n} \Lambda_{ij}^n} \right), \qquad \Delta t_2 = \min_{i,j \in I} \left(\frac{\gamma_{ij}^2}{\max\limits_{i \in I} \left(\max \left(\frac{3\mu}{4\rho_i}, \frac{\kappa}{\rho_i R} \right) \right)} \right), \tag{4.27}$$

4.4.1 2D Sod shock tube test

This section examines the one-dimensional shock tube problem in a two-dimensional setting $\Omega = [0, 0.06] \times [0, 1]$ and the initial condition is defined as

$$(\rho^0, u^0, v^0, p^0) = \begin{cases} (1, 0.75, 0, 1) & \text{if } x \leq 0.5, \\ (0.125, 0, 0, 0.1) & \text{otherwise.} \end{cases} \tag{4.28}$$

The numerical results presented in this section were calculated with a Cartesian mesh composed of 600×40 cells and $Cr = 0.8$ and we use the same exact solution as in the 1D case as a reference solution.
In Fig. 4.7 (left), we present a cross-section in the x-direction of the numerical results computed using our method, Roe and Rusanov. In Fig. 4.7 (right), we present α_{ij}^n at t=0.2s.

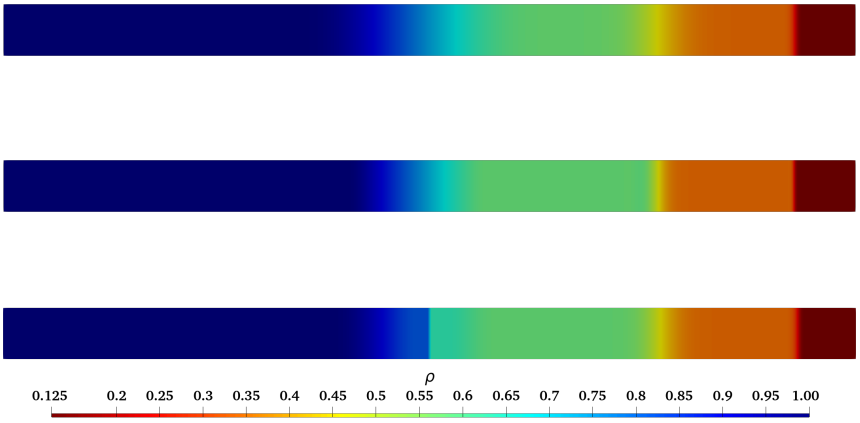

Figure 4.5: 2D Sod shock tube: the density distribution at t=0.2s using Rusanov (top), FVC (middle) and Roe (bottom)

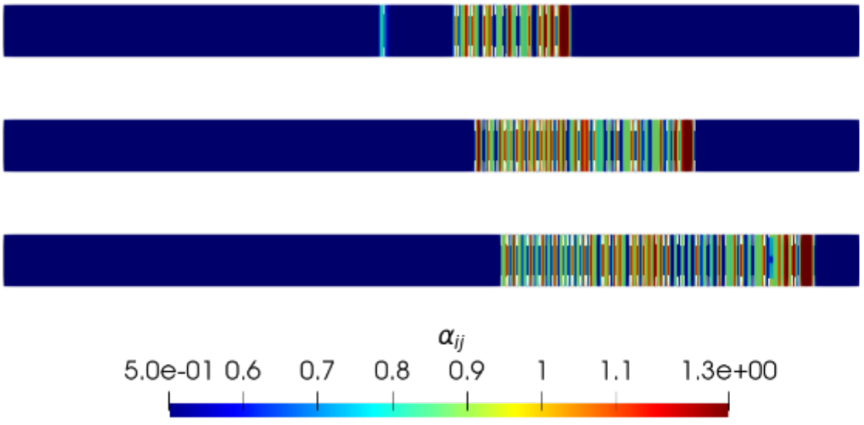

Figure 4.6: 2D Sod shock tube: the local control diffusion parameter α_{ij}^n at t=0.06 (top), t=0.13 (middle) and t=0.2 (bottom).

As the 1D shock tube test [5], we note that the shock, the contact, and the rarefaction are better captured using the FVC scheme. Moreover, the FVC scheme (unlike the Roe scheme) does not generate an artificial shock around the sonic point.
In Fig 4.9 we compare the L^1 error using different schemes. It confirms that FVC method is more accurate than Rusanov scheme, and Roe scheme with Harten entropy correction [35].

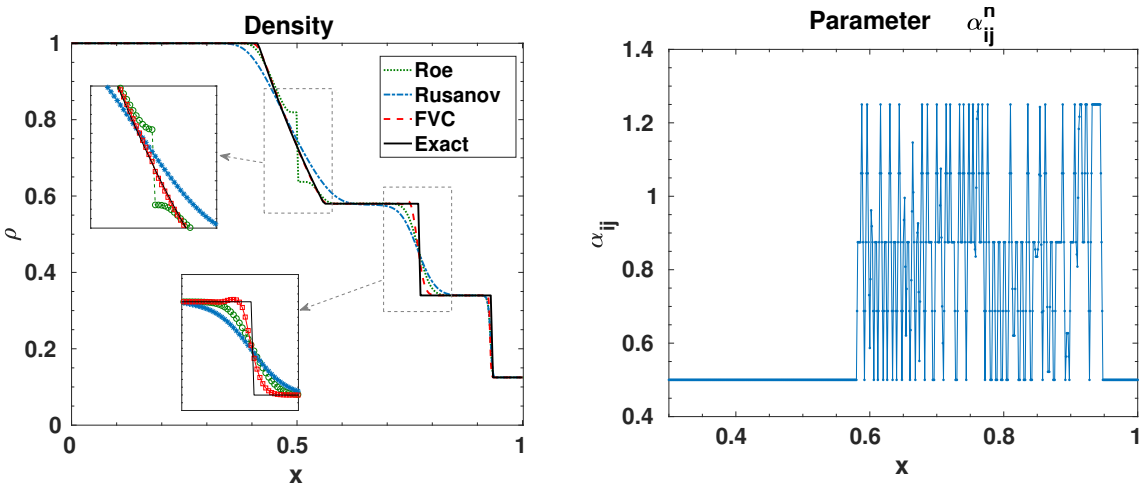

FIGURE 4.7: 2D Sod shock tube: cross-section of the density distribution (left) and cross-section of the control parameter α_{ij}^n variation (right) along the x-direction at time $t = 0.2s$.

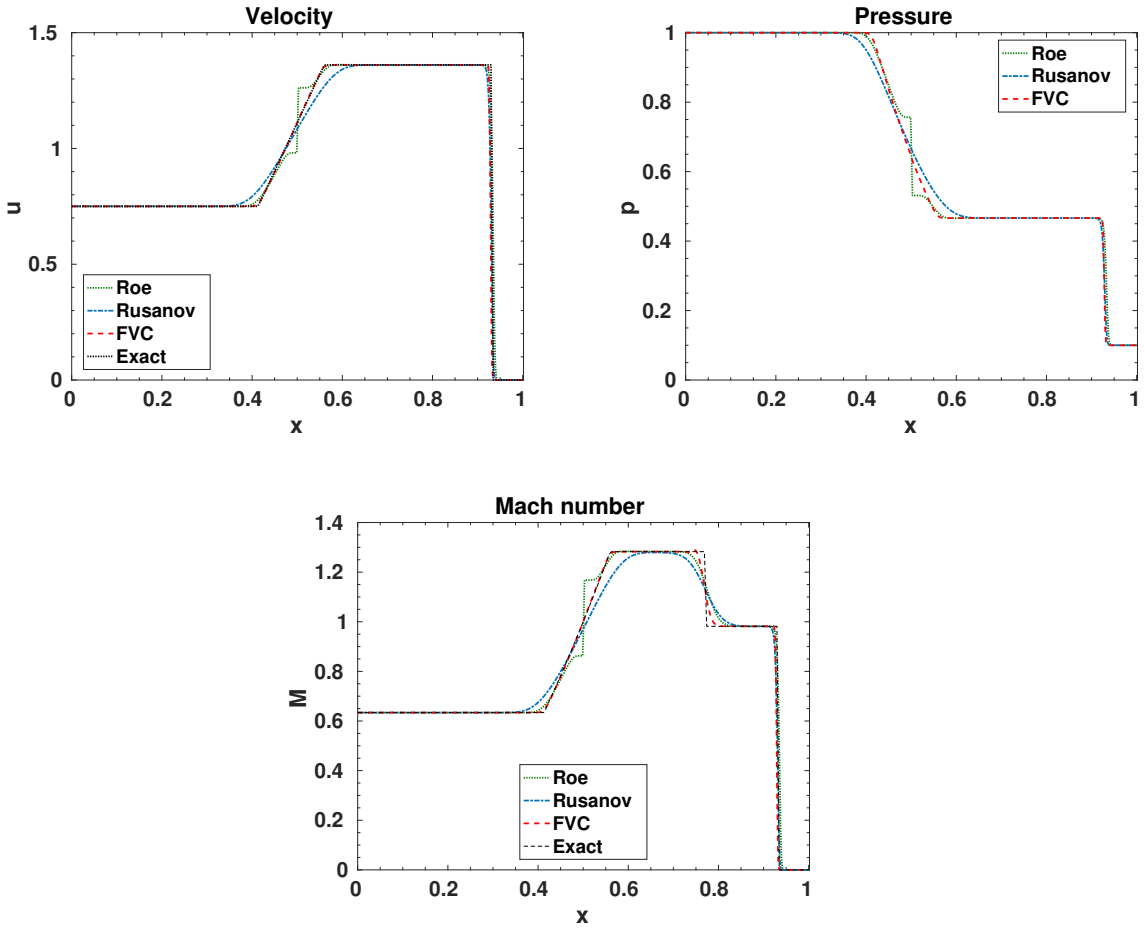

FIGURE 4.8: 2D Sod shock tube: cross-section of the axial velocity (top left), pressure (top right) and Mach number (bottom) along the x-direction at time $t = 0.2s$.

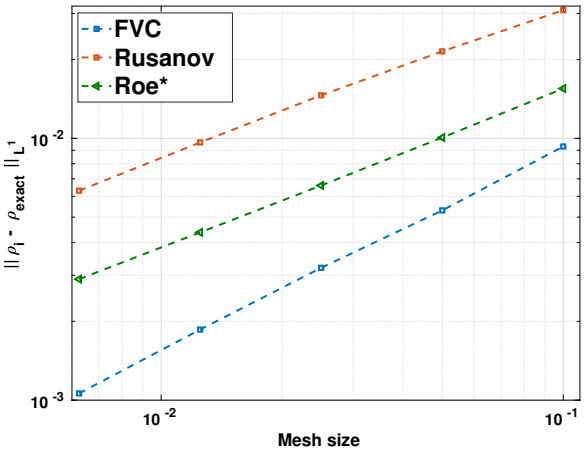

Figure 4.9: L^1 error (logarithmic scales) for 2D sod shock problem at time t = 0.2s.

4.4.2 2D explosion test

Here, we solve a two-dimensional explosion problem on the computational domain $\Omega = [-1, 1] \times [-1, 1]$ and the following initial condition

$$(\rho^0, u^0, v^0, p^0) = \begin{cases} (1, 0, 0, 1) & \text{if } \sqrt{x^2 + y^2} \leq 0.5, \\ (0.125, 0, 0, 0.1) & \text{otherwise.} \end{cases} \tag{4.29}$$

The numerical results presented in this section were calculated with a hybrid mesh composed of 22 236 non-uniform cells and $Cr = 0.8$. We use the numerical solution obtained by Roe scheme on 10^6 cells as a reference solution. Fig. 4.10 shows the bird's eye views of the density (left) and the local diffusion parameter (right) at t=0.2s. To better understand these results, we plot the cross-section in Fig 4.11, which shows us that the method is more accurate than Roe and Rusanov schemes (left). In addition, the right figure shows us that α_{ij}^n adapts itself to get a less diffused solution. The FVC scheme exhibits a minor oscillation at the end of the rarefaction wave; this oscillation vanishes as the number of cells is increased.

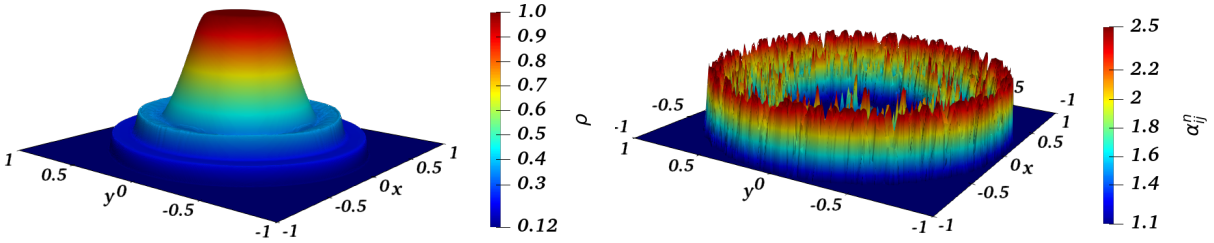

Figure 4.10: 2D explosion: the bird's eye view of density distribution (left) and bird's eye view of the local control diffusion parameter α_{ij}^n variation (right) at t=0.2s

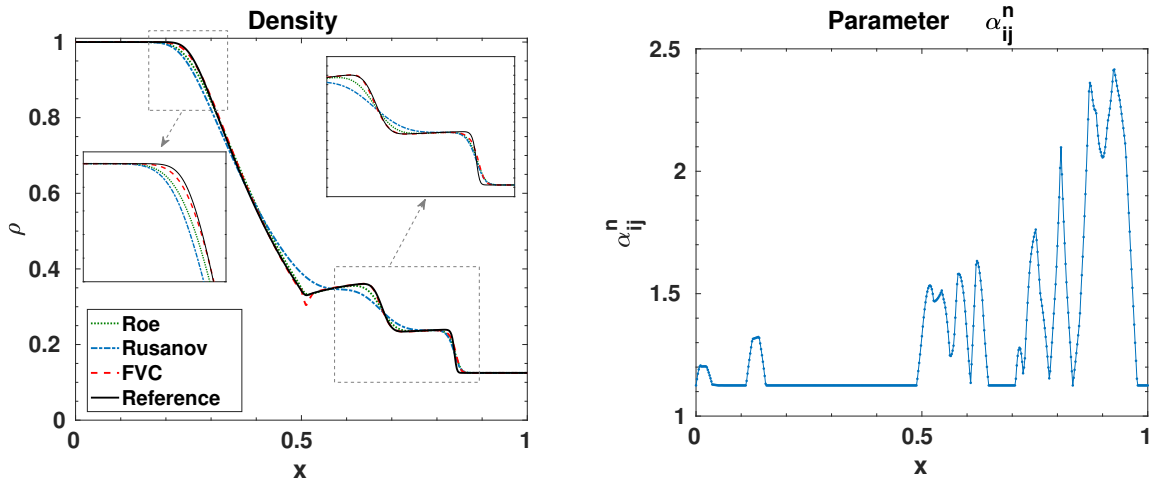

Figure 4.11: 2D explosion: cross-section of the density distribution (left) and cross-section of the control parameter α_{ij}^n variation along the radial direction(right) at t=0.2s.

4.4.3 Supersonic flow over a flat plate

The main aim of this particular test case is to validate the numerical results obtained for the scenario governed by the Euler equation. In addition to the presence of a boundary layer, this flow configuration also gives rise to the formation of a shock wave, as shown in Figure 4.12. This dual characteristic represents an interesting challenge for our approach and check the ability of the diffusion control parameter α to detect the shock to better capture it.

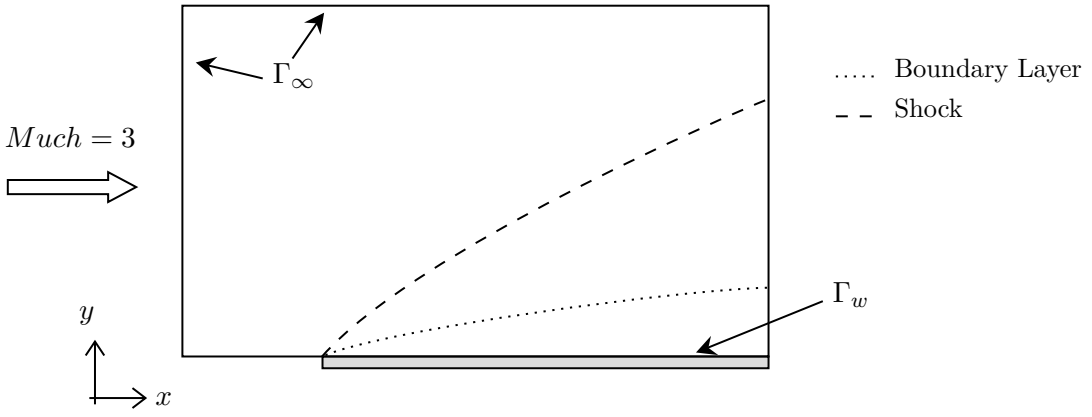

Figure 4.12: Various zones for viscous supersonic flow over a flat plate.

The flow is assumed to be uniform at the far-field boundary Γ_∞, and we impose

$$\rho_\infty = 1, \quad \mathbf{u}_\infty = \begin{pmatrix} \cos\alpha \\ \sin\alpha \end{pmatrix}, \quad p_\infty = \frac{1}{\gamma M_\infty^2}, \quad \text{and} \quad T_\infty = \frac{1}{\gamma(\gamma-1)M_\infty^2}, \tag{4.30}$$

where α is the angle of attack and M_∞ is the freestream Mach number. On the wall boundary Γ_w, we assume the no-slip condition together with an inhomogeneous Dirichlet condition on the temperature (isothermal wall):

$$u_w = v_w = 0 \quad \text{and} \quad T_w = \left(1 + \frac{\gamma - 1}{2} M_\infty^2\right) T_\infty, \tag{4.31}$$

while the density is free of any condition.

The numerical results presented in this section were with a Cartesian mesh composed of 8142 cells, as shown in Figure 4.13, and $Cr = 0.4$. We use the numerical solution obtained by the second order Roe scheme as a reference solution. The initial condition of the problem is given by the freestream condition.

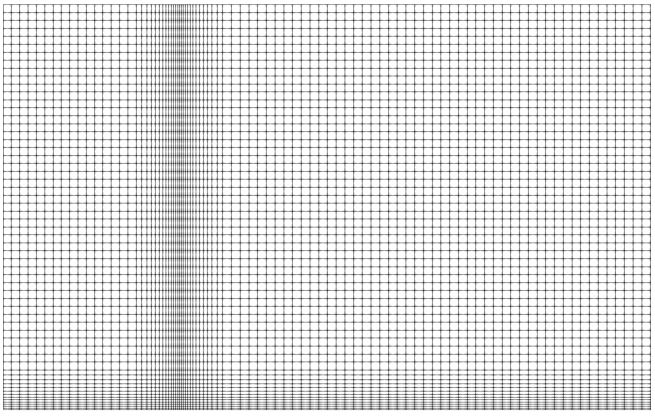

Figure 4.13: Cartesian mesh for the flat plate problem with 8142 cells.

In Figure 4.14, the numerical outcomes from employing the FVC scheme, Roe scheme, and Rusanov scheme are compared, with each method's results organized into rows one, two, and three, respectively. The comparison spans two moments in time: $t = 3$ showcased in the first column and $t = 10$ in the second column. Across all three numerical solutions, the formation of the boundary layer is evident, alongside the shock wave, which becomes less pronounced in the Rusanov scheme due to its inherently high diffusivity.

For a more detailed comparison, Figure 4.15 depicts the velocity u profiles at two different positions, $x = 2$ in the first column and $x = 4$ in the second column, at three distinct times across the rows. These visualizations demonstrate the shock wave and its movement over time. It is observable that the FVC scheme more accurately captures the shock wave compared to the Roe scheme, while in the Rusanov case, the shock wave is nearly obscured by numerical diffusion. This comparison underscores the effectiveness of the diffusion control parameter α in identifying and accurately modeling shock waves, highlighting its critical role in enhancing the precision of fluid dynamics simulations.

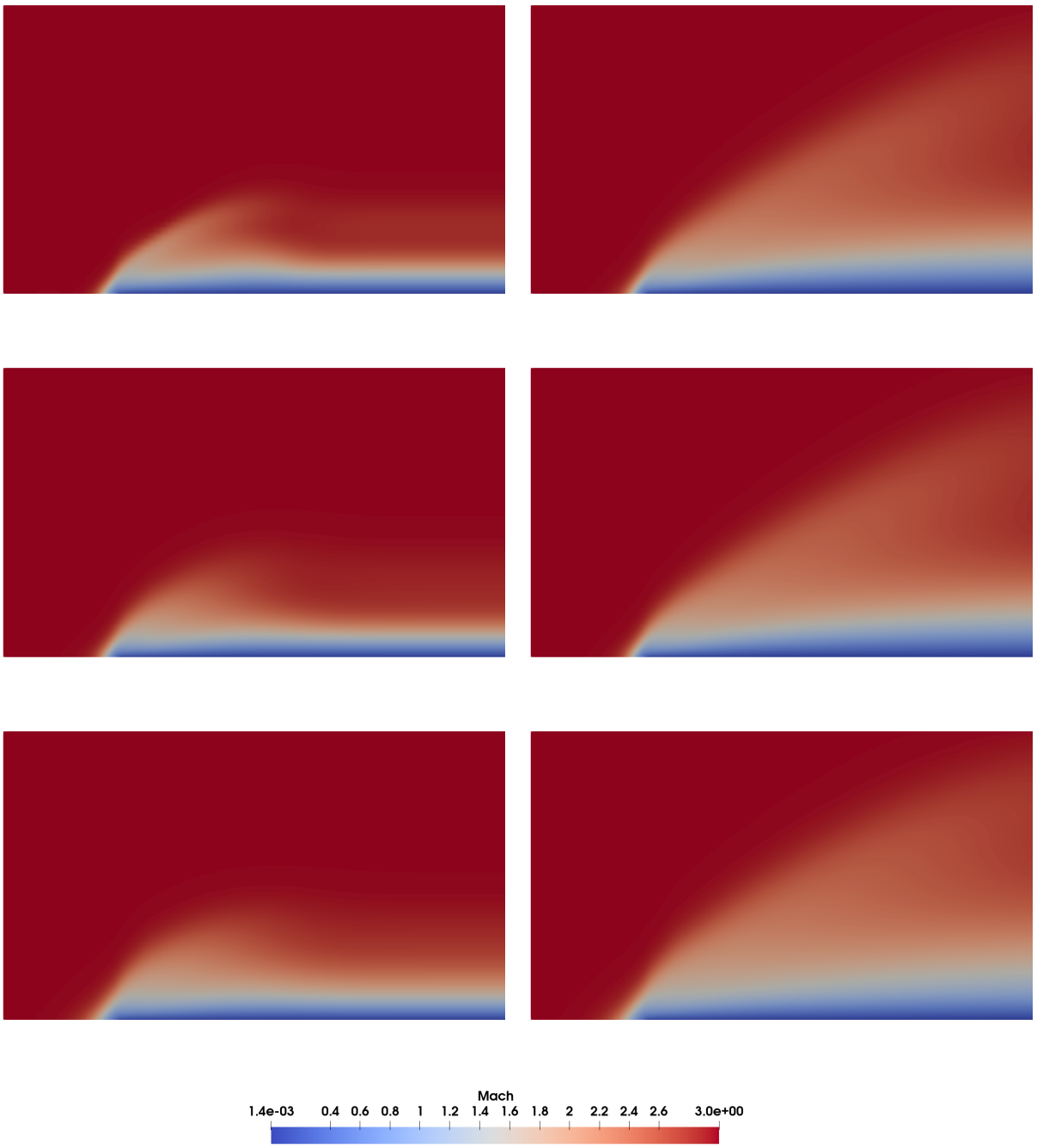

Figure 4.14: Mach number M with FVC (first row), Roe (second row) and Rusanov scheme (third row) at time $t = 3$ (first column) and $t = 10$ (second column) with 8142 cells for the flat plate problem ($\alpha = 0$, $M_\infty = 3$).

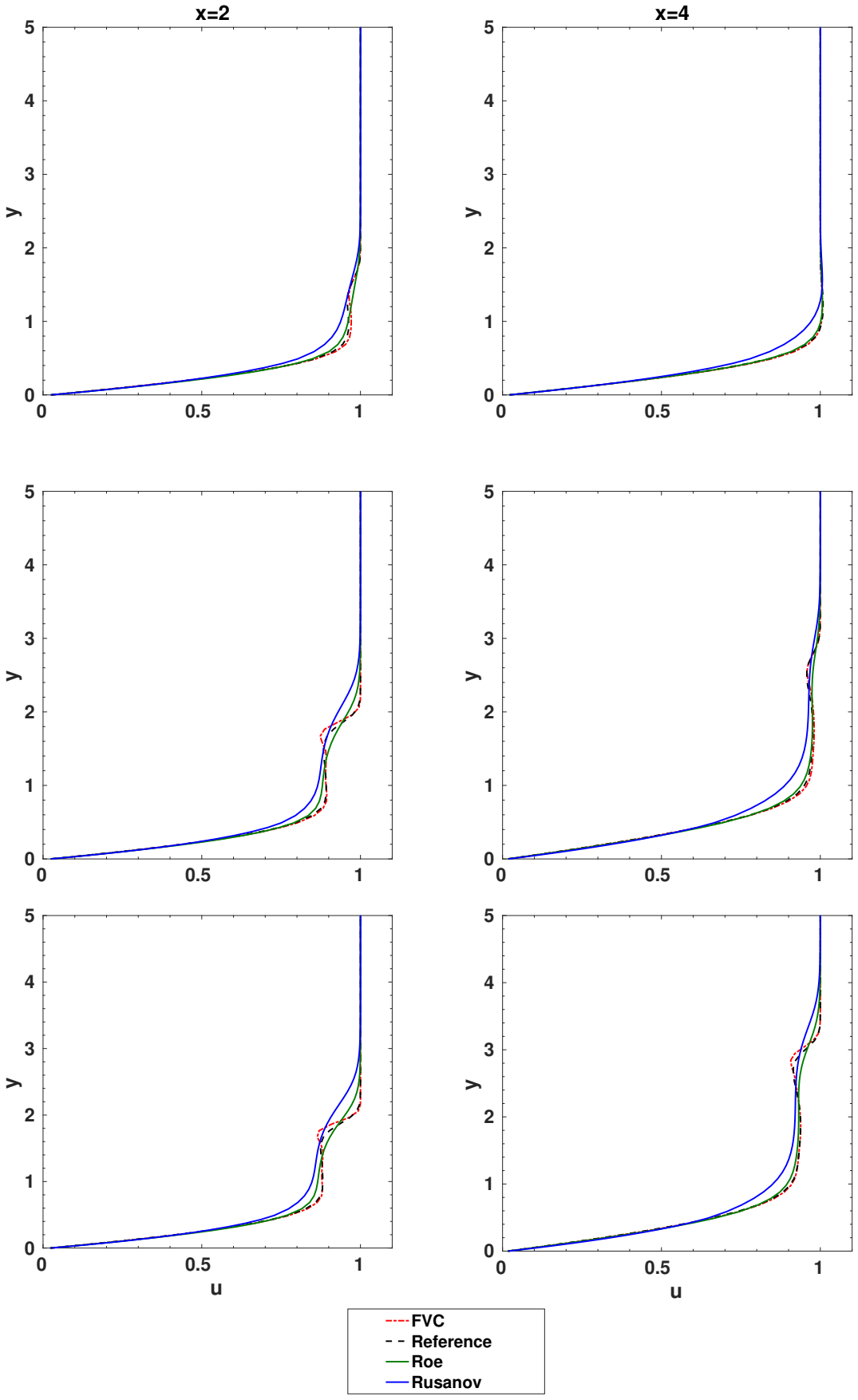

Figure 4.15: u-velocity profile for flat plate benchmark at time $t = 3$ (first row), $t = 6$ (second row), $t = 10$ (third row) with 8142 cells for the flat plate problem ($\alpha = 0$, $M_\infty = 3$).

4.5 Conclusions

In conclusion, this chapter presents a significant enhancement to the FVC scheme by introducing the novel formulation of the α parameter, which was previously a free choice constant in the initial version of the scheme [16]. With the α_{ij}^n formulation, we have successfully made the FVC scheme is more robust and adaptable. The numerical results of this study demonstrate remarkable shock resolution and high accuracy in smooth regions, while effectively eliminating nonphysical oscillations in proximity to shock zones. Furthermore, its ability to capture the boundary layer and shock in viscous flows validates the effectiveness of the approach. Although the numerical calculations have been focused on the compressible Navier Stokes equations, the versatility of the present scheme allows direct extension to various fluid flow problems in 2D and 3D dimensions, as well as for non-Newtonian flows, which is the objective of the next chapter.

Chapter 5

A finite volume method with a diffusion control parameter for compressible Bingham flows

Contents

Abstract

The final part of this thesis focuses on the numerical simulation of an isothermal compressible Bingham flow, highlighting the effectiveness of the FVC with the diffusion control parameter. In the one-dimensional scenario, we use a semi-implicit method, and for the two-dimensional case, we extend the FVC/diamond strategy proposed in the previous chapter for Newtonian flows to the case of Bingham flows. The numerical results demonstrate the effectiveness of the FVC method for the one-dimensional case, as well as its capability to simulate the plug zones in the context of weakly compressible two-dimensional Bingham laminar flows.

5.1 Introduction

This chapter focuses on the compressible flow of Bingham fluids, known by their yield stress behavior. These fluids pose challenges for numerical modeling because of the implicit characteristics of their stress tensor. In this context, the FVC method, enhanced by a diffusion control parameter, emerges as an effective approach for solving the compressible Bingham equation accurately. The methodology outlined in the chapter covers the discretization and numerical methods crucial for tackling the intricate challenges associated with simulations of Bingham flows, providing innovative insights into the prediction and comprehension of these fluid behaviors.

5.2 One-dimensional Bingham equation

5.2.1 Governing equation

The one-dimensional mathematical model that describes the dynamic of a Bingham fluid is given by

$$\begin{cases} \partial_t \rho + \partial_x(\rho u) = 0 & \text{in } \Omega_T, \\ \partial_t(\rho u) + \partial_x\left(\rho u^2\right) - \partial_x(\tau(\partial_x u)) + \partial_x p = \rho f & \text{in } \Omega_T, \\ u(\cdot,0) = u_0 \quad \text{and} \quad \rho(\cdot,0) = \rho_0 & \text{in } \Omega, \end{cases} \tag{5.1}$$

where ρ is the density of the fluid, u is the fluid particle velocity, p is the pressure given as a function of density[1], f represents external forces, and τ is the Bingham stress tensor

$$\begin{cases} \tau(\partial_x u) = \left(\mu + \dfrac{\tau_y}{|\partial_x u|}\right)\partial_x u & \text{if } \partial_x u \neq 0, \\ |\tau| \leq \tau_y & \text{otherwise} \end{cases} \tag{5.2}$$

Here, μ is the viscosity, τ_y is the yield stress and Ω_T the open set $(0,L)\times(0,T)$, where $L>0$ and T is the final time.
The well-posedness for this problem has been investigated in [8], where the author shows the existence and uniqueness of strong solutions for the one-dimensional Bingham flow.

5.2.2 Numerical method

5.2.2.1 Regularisation method

The operator (5.2) becomes implicit below the yield stress, making it challenging to directly simulate a Bingham flow. To overcome this issue, we can regularize the stress tensor using an explicit tensor that approximates the behavior of a Bingham fluid. Various regularization methods can be used; an overview of these methods is provided in [23].

1) Papanastasiou [53]:

$$\mu_\varepsilon\left(|\partial_x u_\varepsilon|\right) = \mu + \frac{\tau_y}{|\partial_x u|}\left(1 - e^{-\frac{|\partial_x u_\varepsilon|}{\varepsilon}}\right) \tag{5.3}$$

[1] In this section, we take $p = a\rho^\gamma$, where a and γ are positive constants.

$$\tau_\varepsilon(\partial_x u_\varepsilon) = \left(\mu + \frac{\tau_y}{|\partial_x u|}\left(1 - e^{-\frac{|\partial_x u_\varepsilon|}{\varepsilon}}\right)\right)\partial_x u_\varepsilon \tag{5.4}$$

2) Bercovier and Engelman [17]:

$$\mu_\varepsilon\left(|\partial_x u_\varepsilon|\right) = \mu + \frac{\tau_y}{\sqrt{\varepsilon^2 + |\partial_x u_\varepsilon|^2}} \tag{5.5}$$

$$\tau_\varepsilon(\partial_x u_\varepsilon) = \left(\mu + \frac{\tau_y}{\sqrt{\varepsilon^2 + (\partial_x u_\varepsilon)^2}}\right)\partial_x u_\varepsilon \tag{5.6}$$

3) Bi-viscosity model [18]: This model approximates the behavior of a Bingham fluid as a highly viscous Newtonian fluid when $\tau \leq \tau_y$ (practically solid). We have employed this approximation to construct a weak solution for an incompressible Bingham flow.[1].

$$\mu_\varepsilon(|\partial_x u_\varepsilon|) = \begin{cases} \mu + \frac{\tau_y}{|\partial_x u_\varepsilon|} & \text{if } |\partial_x u_\varepsilon| \geq \frac{\tau_y \varepsilon}{\mu(1-\varepsilon)}, \\ \mu/\varepsilon & \text{otherwise} \end{cases} \tag{5.7}$$

$$\tau_\varepsilon(\partial_x u_\varepsilon) = \begin{cases} \left(\mu + \frac{\tau_y}{|\partial_x u_\varepsilon|}\right)\partial_x u_\varepsilon & \text{if } |\partial_x u_\varepsilon| \geq \frac{\tau_y \varepsilon}{\mu(1-\varepsilon)}, \\ \mu\frac{\partial_x u_\varepsilon}{\varepsilon} & \text{otherwise} \end{cases} \tag{5.8}$$

Among these three models, the second one is the simplest to use because it offers a C^∞ estimate of μ_ε, consequently, we use the Bercovier and Engelman approximation, and the problem to solve is

$$(P_\varepsilon): \begin{cases} \partial_t \rho_\varepsilon + \partial_x(\rho_\varepsilon u_\varepsilon) = 0 & \text{in } \Omega_T, \\ \partial_t(\rho_\varepsilon u_\varepsilon) + \partial_x\left(\rho_\varepsilon u_\varepsilon^2\right) - \partial_x\left(\left(\mu + \frac{\tau_y}{\sqrt{\varepsilon^2 + (\partial_x u_\varepsilon)^2}}\right)\partial_x u\right) + \partial_x p(\rho_\varepsilon) = \rho_\varepsilon f & \text{in } \Omega_T, \\ u_\varepsilon(\cdot,0) = u_0 \quad \text{and} \quad \rho_\varepsilon(\cdot,0) = u_0 & \text{in } \Omega, \end{cases} \tag{5.9}$$

5.2.2.2 Time splitting algorithm

To solve numerically the problem (P_ε), we use the standard time splitting algorithm.

The following procedure is used to calculate the values of ρ^n and u^n. Assume that ρ^n, u^n are known. First, we solve the compressible Euler equation and obtain $u^{n+\frac{1}{2}}, \rho^{n+\frac{1}{2}}$:

$$(P_\varepsilon^{n+1/2}): \begin{cases} \dfrac{\rho^{n+\frac{1}{2}} - \rho^n}{\Delta t} + \partial_x\left(\rho^n u^n\right) = 0, \\ \dfrac{\rho^{n+\frac{1}{2}} u^{n+\frac{1}{2}} - \rho^n u^n}{\Delta t} + \partial_x\left(\rho^n (u^n)^2 + p^n\right) = 0. \end{cases} \tag{5.10}$$

In the second step we obtain u^{n+1}, ρ^{n+1} by solving

$$(P_\varepsilon^{n+1}) : \begin{cases} \dfrac{\rho^{n+1} - \rho^{n+\frac{1}{2}}}{\Delta t} = 0, \\ \dfrac{\rho^{n+1}u^{n+1} - \rho^{n+\frac{1}{2}}u^{n+\frac{1}{2}}}{\Delta t} - \partial_x(\tau_\varepsilon(\partial_x u^{n+1})) = \rho^{n+\frac{1}{2}} f^{n+\frac{1}{2}}. \end{cases} \tag{5.11}$$

As the first equation trivially gives $\rho^{n+1} = \rho^{n+1/2}$, only the second one is needed.

5.2.2.3 Finite volume characteristic method for barotropic Euler equation

The approach we follow in this chapter consists of solving the following hyperbolic problem

$$\partial_t \mathbf{W} + \partial_x \mathbf{F}(\mathbf{W}) = 0, \tag{5.12}$$

where

$$\mathbf{W} = \begin{pmatrix} \rho \\ \rho u \end{pmatrix}, \quad \text{and} \quad \mathbf{F}(\mathbf{W}) = \begin{pmatrix} \rho u \\ \rho u^2 + p(\rho) \end{pmatrix}. \tag{5.13}$$

As demonstrated in chapter 4, the FVC method is an efficient approach for hyperbolic systems. To apply this method, we start by rewriting the system (5.13) in its advective form:

$$\partial_t \mathbf{W} + u\partial_x \mathbf{W} = \mathbf{G}(\mathbf{W}), \tag{5.14}$$

where

$$\mathbf{G}(\mathbf{W}) = \begin{pmatrix} -\rho\partial_x u \\ -\rho\partial_x u - \partial_x p \end{pmatrix}. \tag{5.15}$$

This version of the equation is used to reconstruct the intermediate states $\mathbf{W}^n_{i+1/2}$ using the method of characteristics. We calculate now the characteristic curves $x_c(s)$ associated to (5.14) as

$$\begin{cases} \dfrac{\mathrm{d}x_c(s)}{\mathrm{d}s} = u\left(x_c(s), s\right), \quad s \in \left[t_n, t_n + \alpha^n_{i+1/2}\Delta t\right], \\ x_c\left(t_n + \alpha^n_{i+1/2}\Delta t\right) = x_{i+1/2}, \end{cases} \tag{5.16}$$

where u is the velocity of the fluid flow. Note that $x_c(s)$ is the departure point at time s of a particle that will arrive at the gridpoint $x_{i+1/2}$ in time $t_n + \alpha^n_{i+1/2}\Delta t$, with $\alpha^n_{i+1/2}$ is a parameter less than 1, that controls the temporal grid.This parameter is calculated locally and at each time step with the following formula,

$$\alpha^n_{i+1/2} = \tilde{\alpha}_{i+1/2} + \left(\frac{1}{2} - \tilde{\alpha}_{i+1/2}\right)\phi(r_{i+1/2}) \tag{5.17}$$

where

$$\tilde{\alpha}_{i+1/2} = \frac{\Delta x}{2\Delta t S_{i+1/2}}, \quad \text{and} \quad S_{i+1/2} = \max_k \left(\max_i \left(\left|\lambda^k_i\right|, \left|\lambda^k_{i+1}\right|\right)\right) \tag{5.18}$$

here λ_i^k is the k^{th} eigenvalue of (5.13), $S_{i+1/2}$ is the local Rusanov speed and $\phi(r_{i+1/2})$ is a slope limiter. The results, presented in this section, were obtained using the Minmod limiter. The ratio $r_{i+1/2}$ is given by

$$r_{i+1/2} = \frac{q_i - q_{i-1}}{q_{i+1} - q_i} \tag{5.19}$$

where

$$q_i = \max_i \left(\left| u_i + \frac{2c_i}{\gamma - 1} \right|, \left| u_i - \frac{2c_i}{\gamma - 1} \right| \right), \tag{5.20}$$

and

$$\phi(r) = \max(0, min(1, r)), \qquad \lim_{r \to \infty} \phi(r) = 1 \tag{5.21}$$

The solution of (5.16) can be approximate as follow

$$x_c\left(t_n\right) = x_{i+1/2} - \alpha_{i+1/2}^n \Delta t u\left(x_c(t_n), t_n\right) \tag{5.22}$$

then we used the fixed point method to solve equation (5.22). Thus, once the characteristic curves $x_c\left(t_n\right)$ are accurately calculated, the intermediate solutions $\mathbf{W}_{i+1/2}^n$ of a generic function $\mathbf{W}(x_{i+1/2}, t_n + \alpha_{i+1/2}^n \Delta t)$ are reconstructed using

$$\mathbf{W}_{i+1/2}^n = \widehat{\mathbf{W}}_{i+1/2}^n + \int_{t_n}^{t_n + \alpha_{i+1/2}^n \Delta t} \mathbf{G}(\mathbf{W}\left(x_c(s), s\right)) \, ds, \tag{5.23}$$

where $\widehat{\mathbf{W}}_{i+1/2}^n = \mathbf{W}\left(x_c\left(t_n\right), t_n\right)$ are the solutions at the characteristic foot computed by linear-based interpolation

$$\widehat{\mathbf{W}}_{i+1/2}^n = \mathbf{W}_i^n + \frac{\mathbf{W}_{i+1}^n - \mathbf{W}_i^n}{\Delta x} \Big(x_c(t_n) - x_i(t_n) \Big), \tag{5.24}$$

Due to the approximation of the integral in equation (5.23) by the rectangle method, the solution at the interfaces is reconstructed using

$$\mathbf{W}_{i+1/2}^n = \widehat{\mathbf{W}}_{i+1/2}^n + \alpha_{i+1/2}^n \Delta t \mathbf{G}(\widehat{\mathbf{W}}_{i+1/2}^n), \tag{5.25}$$

such that the derivatives contained in $\mathbf{G}$ are calculated by a finite difference between cells i and $i+1$ for the interface $i+1/2$.
Finally, the FVC scheme with the diffusion control parameter $\alpha_{i+1/2}^n$ can be written as fellows

$$\mathbf{W}_i^{n+1/2} = \mathbf{W}_i^n - \frac{\Delta t}{\Delta x} \Big(\mathbf{F}\Big(\mathbf{W}_{i+1/2}^n\Big) - \mathbf{F}\Big(\mathbf{W}_{i-1/2}^n\Big) \Big), \tag{5.26}$$

where $\mathbf{W}_{i \pm 1/2}^n$ are calculated using (5.25), and $\mathbf{F}$ is the physical flux given in (5.13).

5.2.2.4 Implicit finite volume method for viscoplastic equation

Integrating the problem P_ε^{n+1} over a control $[x_{i-1/2}, x_{i+1/2}]$ we obtain

$$\begin{cases} \rho_i^{n+1} = \rho_i^{n+\frac{1}{2}}, \\ \rho_i^{n+1} u_i^{n+1} = \rho_i^{n+\frac{1}{2}} u_i^{n+\frac{1}{2}} + \dfrac{\Delta t}{\Delta x}\left[\left(\tau_\varepsilon\left(\partial_x u_{i+1/2}^{n+1}\right)\right) - \left(\tau_\varepsilon\left(\partial_x u_{i-1/2}^{n+1}\right)\right) + \rho_i^{n+\frac{1}{2}} \bar{f}_i^{n+\frac{1}{2}}\right]. \end{cases} \tag{5.27}$$

By setting $\partial_x u_{i+1/2}^{n+1} = \dfrac{u_{i+1}^{n+1} - u_i^{n+1}}{\Delta x}$ and using Bercovier regularisation we get

$$\begin{aligned} \rho_i^{n+1} u_i^{n+1} = \; & \rho_i^{n+\frac{1}{2}} u_i^{n+\frac{1}{2}} + \frac{\Delta t}{\Delta x} \rho_i^{n+\frac{1}{2}} \bar{f}_i^{n+\frac{1}{2}} \\ & + \frac{\Delta t}{\Delta x}\left(\frac{\mu}{\Delta x} + \frac{\tau_y}{\sqrt{\Delta x^2 \varepsilon^2 + \left(u_{i+1}^{n+1} - u_i^{n+1}\right)^2}}\right) \left(u_{i+1}^{n+1} - u_i^{n+1}\right) \\ & - \frac{\Delta t}{\Delta x}\left(\frac{\mu}{\Delta x} + \frac{\tau_y}{\sqrt{\Delta x^2 \varepsilon^2 + \left(u_i^{n+1} - u_{i-1}^{n+1}\right)^2}}\right) \left(u_i^{n+1} - u_{i-1}^{n+1}\right), \end{aligned} \tag{5.28}$$

to solve (5.28), we use the fixed point method :

$$\begin{aligned} & \left(\frac{2\mu\Delta t}{\Delta x} + \frac{\tau_y \Delta t}{\sqrt{\Delta x^2\varepsilon^2 + \left(u_{i+1}^{n+1,k} - u_i^{n+1,k}\right)^2}} + \frac{\tau_y \Delta t}{\sqrt{\Delta x^2\varepsilon^2 + \left(u_i^{n+1,k} - u_{i-1}^{n+1,k}\right)^2}} + \Delta x \rho_i^{n+1/2}\right) u_i^{n+1,k+1} \\ & - \left(\frac{\mu\Delta t}{\Delta x} + \frac{\tau_y \Delta t}{\sqrt{\Delta x^2\varepsilon^2 + \left(u_{i+1}^{n+1,k} - u_i^{n+1,k}\right)^2}}\right) u_{i+1}^{n+1,k+1} - \left(\frac{\mu\Delta t}{\Delta x} + \frac{\tau_y \Delta t}{\sqrt{\Delta x^2\varepsilon^2 + \left(u_i^{n+1,k} - u_{i-1}^{n+1,k}\right)^2}}\right) u_{i-1}^{n+1,k+1} \\ & = \Delta t \rho_i^{n+\frac{1}{2}} \bar{f}_i^{n+\frac{1}{2}} + \Delta x \rho_i^{n+1/2} u_i^{n+1/2}. \end{aligned}$$

Therefore, we have to solve the following linear system

$$\begin{pmatrix} A_1 & -B_1 & & & \\ -B_1 & A_2 & -B_2 & & \\ & \ddots & \ddots & \ddots & \\ & & \ddots & \ddots & -B_{N_x-1} \\ & & & -B_{N_x-1} & A_{N_x} \end{pmatrix} \begin{pmatrix} u_1^{n+1,k+1} \\ \vdots \\ \vdots \\ \vdots \\ u_{N_x}^{n+1,k+1} \end{pmatrix} = \begin{pmatrix} C_1 \\ \vdots \\ \vdots \\ \vdots \\ C_{N_x} \end{pmatrix}, \tag{5.29}$$

where

$$\begin{cases} B_i = \dfrac{\mu\Delta t}{\Delta x} + \dfrac{\tau_y \Delta t}{\sqrt{\Delta x^2\varepsilon^2 + \left(u_{i+1}^{n+1,k} - u_i^{n+1,k}\right)^2}}, \quad i = 0, \ldots, N_x, \\ A_i = B_{i-1} + B_i + \Delta x \rho_i^{n+1/2}, \quad i = 1, \ldots, N_x, \\ C_i = \Delta t \rho_i^{n+\frac{1}{2}} \bar{f}_i^{n+\frac{1}{2}} + \Delta x \rho_i^{n+1/2} u_i^{n+1/2}, \quad i = 2, \ldots, N_x - 1. \\ C_1 = \Delta t \rho_1^{n+\frac{1}{2}} \bar{f}_1^{n+\frac{1}{2}} + \Delta x \rho_1^{n+1/2} u_1^{n+1/2} + B_0 u_0^{n+1} \\ C_{N_x} = \Delta t \rho_{N_x}^{n+\frac{1}{2}} \bar{f}_{N_x}^{n+\frac{1}{2}} + \Delta x \rho_{N_x}^{n+1/2} u_{N_x}^{n+1/2} + B_{N_x} u_{N_x+1}^{n+1} \end{cases} \tag{5.30}$$

To address the linear system (5.29), one may employ traditional direct or iterative approaches. Given that the matrix is tridiagonal, Thomas's method serves as an efficient strategy for managing this system. This method allows for the solution to be obtained through $O(n)$ operations, contrasting with the $O(n^3)$ operations necessitated by Gaussian elimination. An additional factor favoring this method is the presence of a dominant diagonal within our matrix, which guarantees the algorithm's convergence [37]. Consequently, the problem (5.29) can be resolved utilizing the subsequent formula. Therefore, the problem (5.29) can be solved using the following formula

$$u_i^{n+1,k+1} = \lambda_i u_{i+1}^{n+1,k+1} + r_i, \quad \text{for } i = N_x - 1, \ldots, 2. \tag{5.31}$$

where

$$\begin{cases} \lambda_i = \dfrac{B_i}{A_i - B_{i-1}\lambda_{i-1}} \quad \text{for } i = 2, \ldots, N_x - 1, \\ r_i = \dfrac{C_i + B_{i-1} r_{i-1}}{A_i - B_{i-1}\lambda_{i-1}} \quad \text{for } i = 2, \ldots, N_x. \\ \lambda_1 = B_1/A_1, \qquad r_1 = C_1/A_1, \\ u_{N_x}^{n+1,k+1} = r_{N_x}. \end{cases} \tag{5.32}$$

We stop the iteration procedure when $\left\|u^{n+1,k+1} - u^{n+1,k}\right\| \leq \varepsilon_{\text{tol}}$.

Remark 2. *Note that if we want to use a different regularization, the coefficients of the matrix in (5.29) will change. For example, if we use Papanastasiou regularisation, the coefficients of*

the matrix are given by

$$\begin{cases} B_i = \dfrac{\mu\Delta t}{\Delta x} + \dfrac{\tau_y \Delta t}{\left|u_{i+1}^{n+1,k} - u_i^{n+1,k}\right|}\left(1 - e^{\dfrac{|u_{i+1}^{n+1,k} - u_i^{n+1,k}|}{\varepsilon dx}}\right), \quad i = 0, \ldots, N_x, \\ A_i = B_{i-1} + B_i + \Delta x \rho_i^{n+1/2}, \quad i = 1, \ldots, N_x, \\ C_i = \Delta t \rho_i^{n+\frac{1}{2}} \bar{f}_i^{n+\frac{1}{2}} + \Delta x \rho_i^{n+1/2} u_i^{n+1/2}, \quad i = 2, \ldots, N_x - 1. \\ C_1 = \Delta t \rho_1^{n+\frac{1}{2}} \bar{f}_1^{n+\frac{1}{2}} + \Delta x \rho_1^{n+1/2} u_1^{n+1/2} + B_0 u_0^{n+1} \\ C_{N_x} = \Delta t \rho_{N_x}^{n+\frac{1}{2}} \bar{f}_{N_x}^{n+\frac{1}{2}} + \Delta x \rho_{N_x}^{n+1/2} u_{N_x}^{n+1/2} + B_{N_x} u_{N_x+1}^{n+1} \end{cases} \tag{5.33}$$

5.2.2.5 Algorithm

In summary, below is the algorithm of the numerical method proposed to approximate the solution of a Bingham flow using FVC with a control diffusion parameter and a regularized tensor

Algorithm 3 FVC-Regularisation method for 1D compressible Bingham Flow

$\mathbf{W} = (\rho, \rho u)$;
Initialize conditions;
for each time iteration **do**
  Compute the time step Δt;
  Solve Euler problem:
    Compute $\alpha_{i+1/2}^n$ for all interfaces;
    Compute $x_c(t_n)$;
    Compute $\mathbf{W}_{i+1/2}^n$ for all interfaces;
    Compute the solution $\mathbf{W}^{n+1/2}$;
    Update the intermediate solution: $\mathbf{W}^{n+1/2} \leftarrow \mathbf{W}^n$;
    Update $\mathbf{W}^{n+1/2}$ on boundary;
  Solve viscoplastic problem:
    Choose ε and ε_{tol}
      k=0 and $u^{n+1,k} = u^{n+1/2}$
      While $||u^{n+1,k+1} - u^{n+1,k}|| > \varepsilon_{tol}$ **do**
        $u^{n+1,k} \leftarrow u^{n+1,k+1}$
        Compute $u^{n+1,k+1}$ using (5.31)
        k++
  Update the solution: $\mathbf{W}^{n+1} \leftarrow (\rho^{n+1/2}, \rho^{n+1/2} u^{n+1})$;
  Apply boundary conditions;
end for

5.2.3 Numerical results

As the approach proposed in this chapter is a semi-implicit method, the time step Δt is limited by the following CFL condition

$$\Delta t = Cr \frac{\Delta x}{\max_i \left(\sqrt{2\alpha^n_{i+1/2}} \Lambda^n_i \right)} \tag{5.34}$$

where Cr is the Courant number and $\Lambda_i = \max_k(|\lambda^k_i|)$ is the spectral radius of the barotropic Euler equations.

5.2.3.1 Accuracy test

To evaluate the FVC method with a diffusion control parameter for Bingham flow, we use the analytical solution proposed in [51].

The exact velocity is given by

$$u_e(t,x) = \begin{cases} tx & \text{if } 0 \le x \le 1 \\ t & \text{if } 1 \le x \le 3 \\ t(4-x) & \text{if } 3 \le x \le 4 \end{cases} \tag{5.35}$$

For $a = 1/2$ and $\gamma = 2$ the exact density is given by

$$\rho_e(t,x) = \begin{cases} e^{-\frac{t^2}{2}} & \text{if } 0 \le x \le 1 \\ e^{x-1-\frac{t^2}{2}} & \text{if } 1 \le x \le 1 + \frac{t^2}{2} \\ 1 & \text{if } 1 + \frac{t^2}{2} \le x \le 3 \\ \dfrac{1}{4-x} & \text{if } 3 \le x \le 4 - e^{-\frac{t^2}{2}} \\ e^{\frac{t^2}{2}} & \text{if } 4 - e^{-\frac{t^2}{2}} \le x \le 4. \end{cases} \tag{5.36}$$

Using the Bercovier regularization, the following function is a term source of (5.9)-(5.40)

$$\rho_e f = \begin{cases} xe^{-t^2/2} + \left(1 + t^2\right) & \text{if } 0 < x < 1, \\ e^{x-1-\frac{t^2}{2}} + e^{2x-2-t^2} + t\left(\mu + \dfrac{\tau_y}{\sqrt{\varepsilon^2 + t^2}}\right) & \text{if } 1 < x < 1 + \frac{t^2}{2}, \\ 1 + t\left(\mu + \dfrac{\tau_y}{\sqrt{\varepsilon^2 + t^2}}\right) & \text{if } 1 + \frac{t^2}{2} < x < 3 \\ 1 - t^2 + \dfrac{1}{(4-x)^3} & \text{if } 3 < x < 4 - e^{-\frac{t^2}{2}} \\ e^{\frac{t^2}{2}}(4-x)\left(1 - t^2\right) & \text{if } 4 - e^{-\frac{t^2}{2}} < x < 4. \end{cases} \tag{5.37}$$

Initially, $\rho(\cdot, 0) = 1$ and $u(\cdot, 0) = 0$. For the boundary conditions, we use homogeneous Dirichlet boundary conditions.

Figure 5.1 illustrates the numerical solutions obtained using finite volume methods, specifically Roe, Rusanov, and FVC, each paired with the regularization technique introduced by Bercovier, alongside the exact solution delineated by equations (5.35)-(5.36). Across the three ε values examined, it's observable that the FVC method coupled with Bercovier regularization exhibits lesser diffusion compared to the other methodologies, thereby achieving greater precision. This enhanced accuracy is attributable to the implementation of a control diffusion parameter.

To support this observation, the L^1 and L^2 errors concerning density were calculated, as detailed in Table 5.1 and Table 5.2. These tables explicitly demonstrate that the FVC method surpasses both the Roe and Rusanov schemes in terms of accuracy. The presence of the control diffusion parameter in the FVC method significantly contributes to its ability to produce solutions that are closer to the exact values, minimizing errors and diffusive effects that typically challenge numerical simulations of fluid flow, particularly in complex Bingham fluids.

In Table 5.3, the computational times for each method are presented. As depicted in the table, our approach outperforms other schemes, which can be attributed to the efficiency of the FVC method, as demonstrated in the preceding chapter on the Euler equation.

Table 5.1: L^1 Errors for the density ρ with $\mu = 10^{-3}$ and $\tau_y = 2$.

ε	Mesh	Rusanov	Roe	FVC
10^{-2}	200	4.030943e-02	3.089232e-02	2.236029e-02
	400	2.523166e-02	2.145582e-02	1.703005e-02
	800	1.881412e-02	1.751807e-02	1.559115e-02
	1600	1.562118e-02	1.543954e-02	1.489059e-02
10^{-4}	200	3.030419e-02	1.858219e-02	1.475899e-02
	400	1.531041e-02	1.030015e-02	6.076885e-03
	800	8.466159e-03	5.867581e-03	3.461764e-03
	1600	4.407962e-03	3.022328e-03	1.698364e-03
10^{-6}	200	3.020988e-02	1.857224e-02	1.466148e-02
	400	1.521494e-02	1.018462e-02	5.973536e-03
	800	8.364665e-03	5.746597e-03	3.348680e-03
	1600	4.301818e-03	2.890213e-03	1.572311e-03

5.2.3.2 Bingham flow under the gravitational force

In this benchmark, the objective is to examine the response of a Bingham fluid to applied forces. For this purpose, a flow scenario under gravitational force is considered, where the force term f in equation (5.9) is represented by $f = g\sin(\theta)$, with g denoting the gravitational constant and θ representing the angle of inclination. This scenario can be likened to a Bingham fluid flowing through a pipeline tilted at an angle. The initial conditions are set with a density $\rho(\cdot, 0) = 1$ and $u(\cdot, 0) = 0$. Homogeneous Neumann boundary conditions are applied to the edges of the domain. The fluids viscosity μ_0 is set to 10^{-3}, $a = 1/2$, and $\gamma = 2$.

Table 5.2: L^2 Errors for the density ρ with $\mu = 10^{-3}$ and $\tau_y = 2$.

ε	Mesh	Rusanov	Roe	FVC
10^{-2}	200	3.923155e-03	2.889723e-03	2.128153e-03
	400	1.865139e-03	1.513830e-03	1.207284e-03
	800	1.011378e-03	8.926398e-04	7.770246e-04
	1600	6.033298e-04	5.643922e-04	5.241236e-04
10^{-4}	200	3.301246e-03	2.074852e-03	1.488531e-03
	400	1.321787e-03	8.894142e-04	5.049370e-04
	800	5.624510e-04	3.882260e-04	2.146503e-04
	1600	2.361940e-04	1.640668e-04	8.675113e-05
10^{-6}	200	3.297434e-03	2.073599e-03	1.484124e-03
	400	1.318483e-03	8.852815e-04	5.009955e-04
	800	5.597705e-04	3.851663e-04	2.117027e-04
	1600	2.340508e-04	1.616917e-04	8.447040e-05

Table 5.3: CPU times for Bingham problem with $\mu = 10^{-3}$ and $\tau_y = 2$.

ε	Mesh	Rusanov	Roe	FVC
10^{-2}	200	3.98	5.00	3.54
	400	11.93	15.07	8.36
	800	48.14	56.21	30.42
	1600	189.45	231.09	124.03
10^{-4}	200	6.50	8.26	5.65
	400	23.57	28.76	17.74
	800	97.82	104.16	69.43
	1600	359.28	386.20	257.17
10^{-6}	200	7.00	9.29	6.13
	400	26.36	31.29	19.56
	800	102.76	106.23	72.49
	1600	354.31	397.34	263.64

The numerical results presented in this section were calculated using FVC scheme for the convective part with $Cr = 0.8$, and Bercovier regularization (5.40) with $\varepsilon = 10^{-3}$ for the viscoplastic part.

In Figure 5.2, the velocities at different times (rows) are presented for various values of τ_y (columns). For an angle equal to 3°, the velocity is nearly zero when the yield stress τ_y is set to 50. This implies that the fluid behaves like a solid, even under applied force. For a fluid with a smaller yield stress, we observe that the velocity at $t = 4$ is different from zero but stays near zero. However, when we apply the same force (i.e., the same angle) to a Bingham fluid with $\tau_y = 1$, we observe that the fluid flows immediately. In other words, the force is strong enough to transport the fluid. To better understand and validate the physical behavior of a Bingham fluid, we increase the angle θ (i.e., the force f). In contrast to the previous case, the fluid moves even for $\tau_y = 50$, indicating that applying such force allows us to set the fluid in

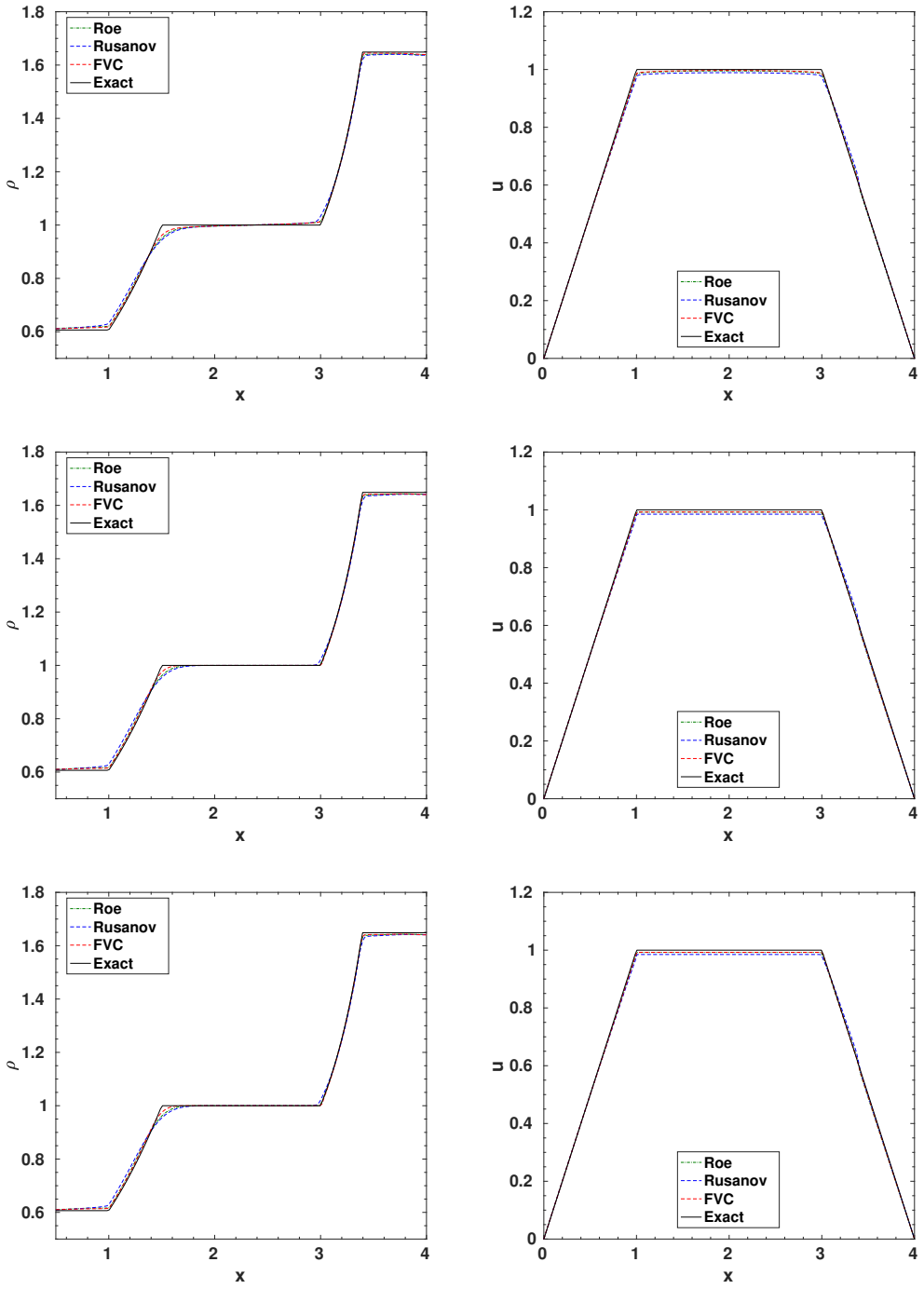

Figure 5.1: Compressible Bingham problem: density ρ (left), velocity u (right) for $\varepsilon = 10^{-2}$ (first row), $\varepsilon = 10^{-4}$ (second row) and $\varepsilon = 10^{-6}$ (third row) with $\tau_y = 2$ and $\mu_0 = 10^{-3}$ at time t = 1s with 400 regular cells.

motion. these results are consistent with the physical behavior of this kind of Non Newtonian fluids.

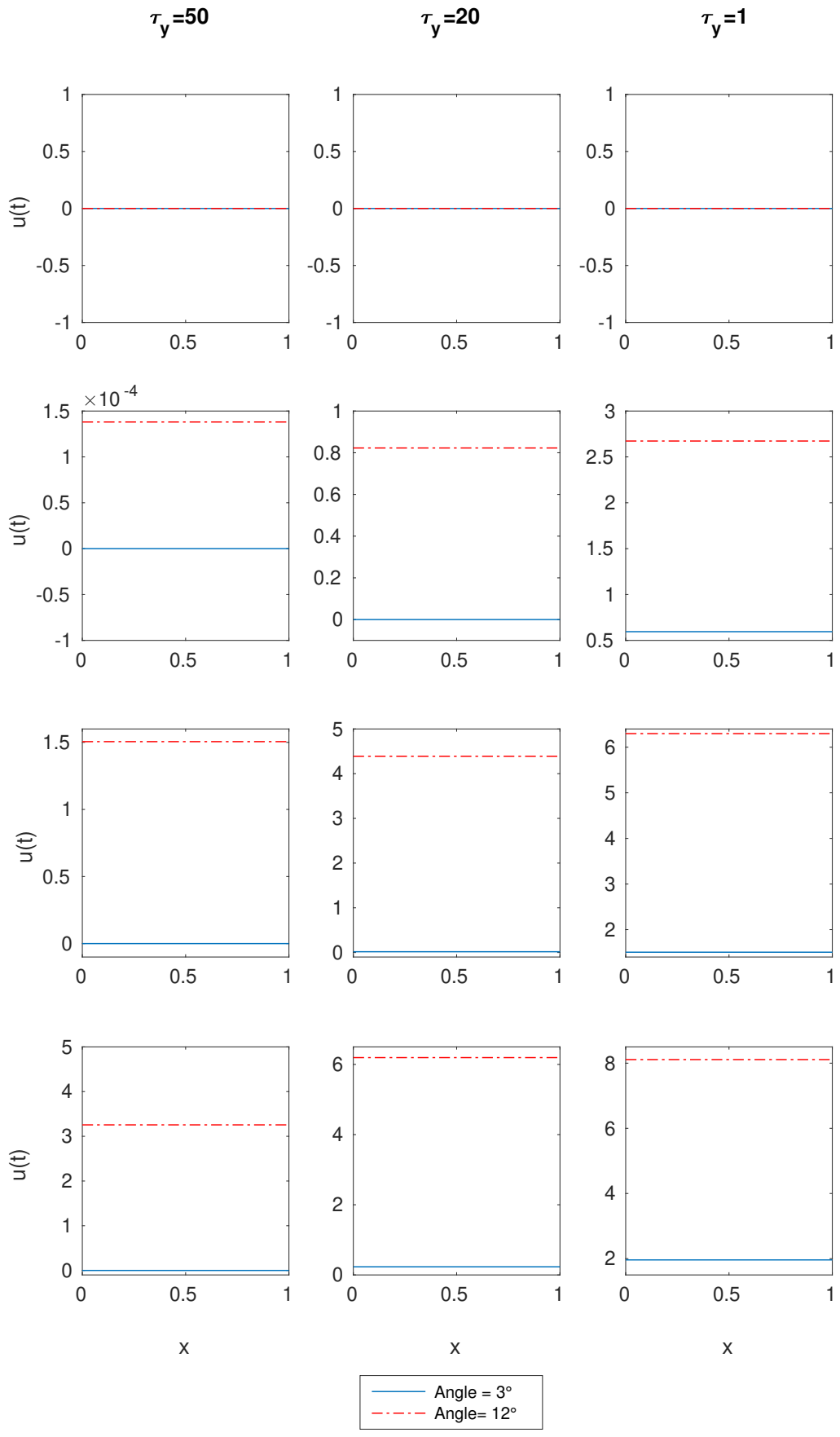

FIGURE 5.2: Velocity u with $\tau_y = 50$ (first column), $\tau_y = 20$ (second column) and $\tau_y = 1$ (third column) at time $t = 0$ (first row), $t = 1.33$ (second row), $t = 3.11$ (third row) and $t = 4$ (fourth row) with 200 regular cells.

In Figure 5.3, we present the velocity u over time for various values of τ_y. Additionally, Figure 5.4 illustrates the relationship between u and τ_y at time $t = 4$. These two figures confirm the observations previously discussed.

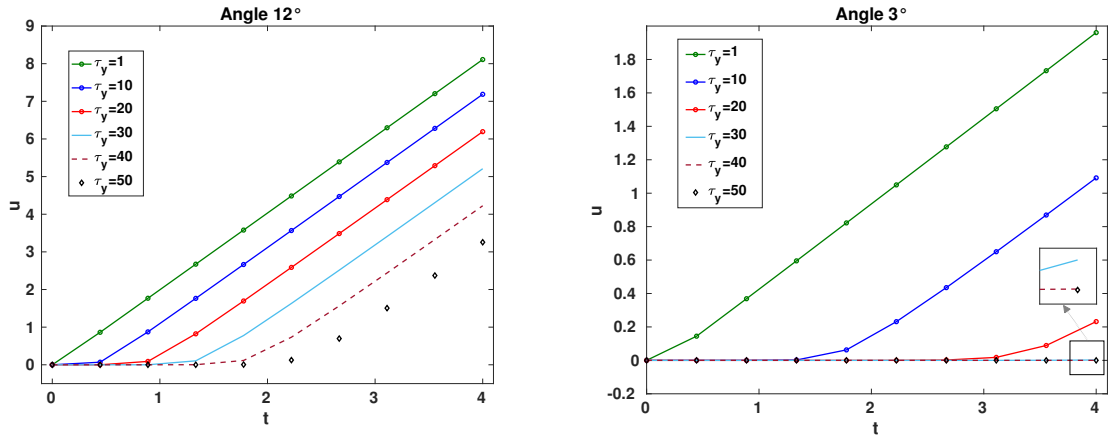

Figure 5.3: Velocity-time for a Bingham flow under the gravity force with $\theta = 12°$ (left) and $\theta = 3°$.

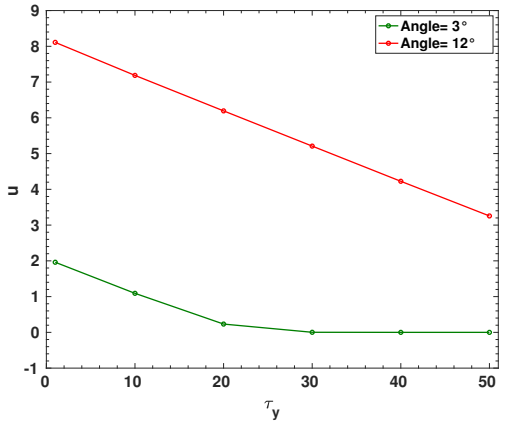

Figure 5.4: Velocity as a function of the yield stress τ_y at time $t = 4$.

5.3 Two-dimensional compressible Bingham flow

In this section, we apply FVC method with the diffusion control parameter α to solve the compressible 2D Bingham equation on a hybrid unstructured mesh.

5.3.1 Governing equation

Let Ω be a domain in $\mathbb{R}^2$ and Ω_T the open set $\Omega \times (0,T)$, where $T > 0$ is the final time. The 2D compressible Bingham equation is given by:

$$\begin{cases} \partial_t \rho + \nabla \cdot (\rho \mathbf{u}) = 0 & \text{in } \Omega_T, \\ \partial_t (\rho \mathbf{u}) + \nabla \cdot (\rho \mathbf{u} \otimes \mathbf{u}) + \boldsymbol{\nabla} p - \nabla \cdot \tau(D\mathbf{u}) = \rho f & \text{in } \Omega_T, \\ \mathbf{u}(\cdot, 0) = \mathbf{u}_0 \quad \text{and} \quad \rho(\cdot, 0) = \rho_0 & \text{in } \Omega, \end{cases} \tag{5.38}$$

In the given system, ρ represents the fluid density, $\mathbf{u} = (u, v)^t$ is the velocity vector, p stands for the pressure given as as function of the density, and τ is the Bingham stress tensor where the strain tensor (shear tensor) is defined as $Du = \frac{1}{2}(\nabla u + \nabla u^t)$, and $f = (f_x, f_y) : \Omega_T \to \mathbb{R}^2$ represents external forces.

The Bingham stress–strain constitutive law is defined as

$$\begin{cases} \tau(D\mathbf{u}) = \left(2\mu + \frac{\tau_y}{|D\mathbf{u}|}\right) D\mathbf{u} & \text{if } |\tau| > \tau_y, \\ \\ D\mathbf{u} = 0 & \text{if } |\tau| \leq \tau_y. \end{cases} \tag{5.39}$$

Here, μ is the viscosity, τ_y is the yield stress and $|A|^2 = A : A$, where the inner product is defined as $A : B = \sum_{i,j} A_{ij} B_{ij}$.

As previously discussed in chapter 1, the peculiarity of the Bingham stress tensor stems from its implicit nature, requiring the introduction of a regularization tensor. To address this, we adopt the Bercovier and Engelman regularization [17]:

$$\tau_\varepsilon(D\mathbf{u}) = \left(2\mu + \frac{\tau_y}{\sqrt{\varepsilon^2 + |\ D\mathbf{u}\ |^2}}\right) D\mathbf{u} \tag{5.40}$$

Using this regularization we get the following problem:

$$\partial_t \mathbf{W} + \nabla \cdot \mathbf{Fc}(\mathbf{W}) - \nabla \cdot \mathbf{Fd}(\nabla \mathbf{W}) = \mathbf{Q}(\mathbf{W}), \tag{5.41}$$

where

$$\mathbf{W} = \begin{pmatrix} \rho \\ \rho u \\ \rho v \end{pmatrix}, \qquad \mathbf{Fc}(\mathbf{W}) = \begin{pmatrix} \rho u & \rho v \\ \rho u^2 + p & \rho uv \\ \rho uv & \rho v^2 + p \end{pmatrix},$$

$$\mathbf{Fd}(\nabla \mathbf{W}) = \left(2\mu + \frac{\tau_y}{\sqrt{\varepsilon^2 + |\ D\mathbf{u}\ |^2}}\right) \begin{pmatrix} 0 & 0 \\ \partial_x u & \frac{1}{2}(\partial_y u + \partial_x v) \\ \frac{1}{2}(\partial_y u + \partial_x v) & \partial_y v \end{pmatrix},$$

and

$$\mathbf{Q}(\mathbf{W}) = \begin{pmatrix} 0 \\ \rho f_x \\ \rho f_y \end{pmatrix},$$

5.3.2 Discretisation and numerical method

To solve the problem (5.41), we applied a splitting strategy, which involves solving the following hyperbolic problem in the first stage:

$$\begin{cases} \dfrac{\partial \mathbf{W}}{\partial t} + \nabla \cdot \mathbf{Fc}(\mathbf{W}) = 0 \\ \\ \mathbf{W}\left(x, y, t^n\right) = \mathbf{W}^n(x, y), \end{cases} \tag{5.42}$$

then, we get $\mathbf{W}\left(x, y, t^{n+1/2}\right)$ from $\mathbf{W}\left(x, y, t^n\right)$. The second step consists of solving the following equation:

$$\begin{cases} \dfrac{\partial \mathbf{W}}{\partial t} - \nabla \cdot \mathbf{Fd}(\nabla \mathbf{W}) = \mathbf{Q}(\mathbf{W}) \\ \\ \mathbf{W}\left(x, y, t^n\right) = \mathbf{W}^{n+1/2}(x, y), \end{cases} \tag{5.43}$$

where $t^n = n\Delta t$, with Δt is the time step. The process of selecting this time step will be examined in more detail later in this chapter.

For the spatial discretization, we use a primal-Diamond mesh, a strategy that has proven its effectiveness in the case of the compressible Navier Stokes equation. As mentioned in the introduction, one of the aims of this thesis is to propose a finite volume method that reduces numerical diffusion. The following sub-section will therefore explain how the proposed FVC method can be applied to problem (5.42).

5.3.2.1 Finite volume characteristic method for convective flux

In this section, we formulate the FVC scheme with a diffusion control parameter to solve equation (5.42). As previously indicated, we employ a hybrid mesh, which is a mixture of structured and unstructured cells. For a better understanding of the method, the reader is encouraged to read the previous chapter. Suppose that the computational domain Ω is divided into a finite number of control volumes $\Omega = (\Omega_i)_{i \in I}$, with I a finite set of indices.
Integrating equation (5.42) over a control volume Ω_i, gives the following integral system

$$\frac{d}{dt} \int_{\Omega_i} \mathbf{W} dV + \int_{\partial \Omega_i} \mathbf{Fc}(\mathbf{W}) \cdot \mathbf{n} \, d\sigma = 0, \tag{5.44}$$

where $\mathbf{n}$ is the normal vector to the edge $\partial \Omega_i$ of the cell Ω_i in the outward direction. According to the framework of the finite volume method, the semi-discrete equation associated with (5.42) is defined as

$$\frac{d\mathbf{W}_i}{dt} = -\frac{1}{|\Omega_i|} \sum_{j \in N_i} |\gamma_{ij}| \mathbf{\Phi}(\mathbf{W}_{ij}, \mathbf{n}_{ij}), \tag{5.45}$$

where

$$\mathbf{W}_i = \frac{1}{|\Omega_i|} \int_{V_i} \mathbf{W} dV, \quad \text{and} \quad \mathbf{\Phi}(\mathbf{W}_{ij}, \mathbf{n}_{ij}) \simeq \frac{1}{|\gamma_{ij}|} \int_{\gamma_{ij}} \mathbf{Fc}(\mathbf{W}) \cdot \mathbf{n}_{ij} d\sigma, \tag{5.46}$$

$\mathbf{W}_{ij}$ is the intermediate state and at the interface γ_{ij} between cells Ω_i and Ω_j and $\mathbf{\Phi}(\mathbf{W}_{ij}, \mathbf{n}_{ij})$ refer to and the numerical flux at the interface γ_{ij}. $\mathbf{n}_{ij}$ is the unit normal to γ_{ij}, outward to Ω_i, and N_i is the set of neighboring cells of the cell Ω_i.

The spatial discretization is complete when a numerical construction of the flux $\mathbf{\Phi}(\mathbf{W}_{ij}, \mathbf{n}_{ij})$ is chosen. In the FVC method, this construction is achieved through the numerical flux, and we have $\mathbf{\Phi}(\mathbf{W}_{ij}, \mathbf{n}_{ij}) = \mathbf{Fc}(\mathbf{W}_{ij}) \cdot \mathbf{n}_{ij}$.
To construct the intermediate state $\mathbf{W}_{ij}$, we start by building the projected velocity model. The equation (5.42), can be writing as follow

$$\frac{\partial}{\partial t}\int_{\Omega_i} \rho \, \mathrm{d}V + \int_{\partial\Omega_i} \rho u_\eta \mathrm{d}\sigma = 0, \tag{5.47}$$

$$\frac{\partial}{\partial t}\int_{\Omega_i} \rho u \, \mathrm{d}V + \int_{\partial\Omega_i} (\rho u u_\eta + p n_x) \, \mathrm{d}\sigma = 0, \tag{5.48}$$

$$\frac{\partial}{\partial t}\int_{\Omega_i} \rho v \, \mathrm{d}V + \int_{\partial\Omega_i} (\rho v u_\eta + p n_y) \, \mathrm{d}\sigma = 0, \tag{5.49}$$

where $\mathbf{n} = (n_x, n_y)^T$ represents the normal vector, and $\tau = (-n_y, n_x)^T$ denotes the tangential vector.. $u_\eta = \mathbf{u} \cdot \mathbf{n}$ is the normal velocity and $u_\tau = \mathbf{u} \cdot \tau$ is the tangential velocity.
Using the fact that Euler equation is invariant by rotation, i.e. $T\mathbf{Fc} \cdot \mathbf{n} = \mathbf{Fc}(T\mathbf{W})$, with

$$T = \begin{pmatrix} 1 & 0 & 0 \\ 0 & n_x & n_y \\ 0 & -n_y & n_x \end{pmatrix}, \tag{5.50}$$

we get the following equations

$$\left(\frac{\partial}{\partial t}\int_{\Omega_i} \rho u \, \mathrm{d}V\right) n_x + \left(\frac{\partial}{\partial t}\int_{\Omega_i} \rho v \, \mathrm{d}V\right) n_y = \frac{\partial}{\partial t}\int_{\Omega_i} \rho u_\eta \mathrm{d}V = -\int_{\partial\Omega_i} \left(\rho u_\eta^2 + p\right) \mathrm{d}\sigma, \tag{5.51}$$

and

$$-\left(\frac{\partial}{\partial t}\int_{\Omega_i} \rho u \, \mathrm{d}V\right) n_y + \left(\frac{\partial}{\partial t}\int_{\Omega_i} \rho v \, \mathrm{d}V\right) n_x = \frac{\partial}{\partial t}\int_{\Omega_i} \rho u_\tau \mathrm{d}V = -\int_{\partial\Omega_i} \rho u_\eta u_\tau \mathrm{d}\sigma\cdot \tag{5.52}$$

Consequently, we get the following system

$$\begin{cases} \dfrac{\partial \rho}{\partial t} + \dfrac{\partial \rho u_\eta}{\partial \eta} = 0, \\ \dfrac{\partial \rho u_\eta}{\partial t} + \dfrac{\partial}{\partial \eta}\left(\rho u_\eta^2 + p\right) = 0, \\ \dfrac{\partial \rho u_\tau}{\partial t} + \dfrac{\partial}{\partial \eta}\left(\rho u_\eta u_\tau\right) = 0. \end{cases} \tag{5.53}$$

The projected velocity model associated with the equation (5.42) is

$$\frac{\partial \mathbf{U}}{\partial t}(t, X) + u_\eta(t, X)\frac{\partial \mathbf{U}}{\partial \eta}(t, X) = \mathbf{S}(\mathbf{U}(t, X)), \tag{5.54}$$

where

$$T\mathbf{W} = \mathbf{U} = \begin{pmatrix} \rho \\ \rho u_\eta \\ \rho u_\tau \end{pmatrix}, \qquad \mathbf{S}(\mathbf{U}) = \begin{pmatrix} -\rho \partial_\eta u_\eta \\ -\rho u_\eta \partial_\eta u_\eta - \partial_\eta p \\ -\rho u_\tau \partial_\eta u_\eta \end{pmatrix}. \tag{5.55}$$

The characteristic curves associated with (5.54) are the solutions of the following ODE.

$$\begin{cases} \dfrac{dX^c(t)}{dt} = u_\eta(t, X^c(t))\mathbf{n}, \quad t \in [t_n, t_n + \alpha_{ij}^n \Delta t], \\ X^c(t_n + \alpha_{ij}^n \Delta t) = X_\star. \end{cases} \tag{5.56}$$

The local diffusion control parameter is given by $\alpha_{ij}^n = \max(\alpha_i^n, \alpha_j^n)$ where α_i^n is chosen as follow

$$\alpha_i^n = \bar{\alpha}_i^n + \left(\frac{1}{2} - \bar{\alpha}_i^n\right)\psi_i \tag{5.57}$$

where

$$\bar{\alpha}_i^n = \max_{k \in N(i)} \left(\frac{|\gamma_{ik}|}{2\Delta t S_{ik}}\right), \quad \text{and} \quad S_{ik} = \max_l \left(\max\left(\left|\lambda_i^l\right|, \left|\lambda_k^l\right|\right)\right) \tag{5.58}$$

here λ_i^l is the l^{th} eigenvalue of normal flux, and ψ_i is the Barth-Jespersen limiter function [12]. The solution of (5.56) can be determined by numerical integration:

$$X^c(t_n) = X_\star - \int_{t_n}^{t_n + \alpha^n \Delta t} u_\eta\left(s, X^c(s)\right)\mathbf{n} ds. \tag{5.59}$$

By using a root-finding algorithm, we find characteristic curves $X^c(t_n)$. After the determination of the characteristic curves, the advection equation (5.54) can be solved using

$$\mathbf{U}(t_n + \alpha_{ij}^n \Delta t, X_\star) = \mathbf{U}(t_n, X^c(t_n)) + \int_{t_n}^{t_n + \alpha_{ij}^n \Delta t} \mathbf{S}(\mathbf{U}(s, X^c(s)))\, ds. \tag{5.60}$$

The solution $\mathbf{U}$ at the characteristic feet is computed using a local least squares interpolation. The normal derivative terms in $\mathbf{S}$ are evaluated using the diamond scheme. Now, we can deduce the solution $\mathbf{W}_{ij}^n$ at the interface γ_{ij} using the transformation T^{-1}

$$\mathbf{W}_{ij}^n = T^{-1}\mathbf{U}_{ij}^n = \begin{pmatrix} 1 & 0 & 0 \\ 0 & n_x x & -n_y \\ 0 & n_y & n_x \end{pmatrix} \begin{pmatrix} \rho \\ \rho u_\eta \\ \rho u_\tau \end{pmatrix}.$$

Finlay, the fully-discrete formulation of the equation (5.42) is given by

$$\mathbf{W}_i^{n+1/2} = \mathbf{W}_i^n - \frac{\Delta t}{|\Omega_i|} \sum_{j \in N_i} |\gamma_{ij}| \mathbf{Fc}(\mathbf{W}_{ij}^n) \cdot \mathbf{n}_{ij}. \tag{5.61}$$

5.3.2.2 Diamond scheme for the viscoplastic flux

In this section, we use the diamond scheme to solve equation (5.43), This approach has been used for the compressible Navier-Stokes equation (see chapter 4).
We integrate the equation (5.43), and we get

$$\frac{d}{dt}\int_{\Omega_i}\mathbf{W}dV-\int_{\partial\Omega_i}\mathbf{Fd}(\nabla\mathbf{W})\cdot\mathbf{n}\;d\sigma=\int_{\Omega_i}\mathbf{Q}(\mathbf{W})dV, \tag{5.62}$$

the semi-discrete equation linked to (5.43) using the finite volume approach is given by

$$\frac{d\mathbf{W}_i}{dt}=\frac{1}{|\Omega_i|}\sum_{j\in N_i}|\gamma_{ij}|\mathbf{\Psi}(\nabla\mathbf{W}_{ij},\mathbf{n}_{ij})+\mathbf{Q}(\mathbf{W}_i) \tag{5.63}$$

$\nabla\mathbf{W}_{ij}$ is the gradient of $\mathbf{W}$ of at the interface γ_{ij} and $\mathbf{\Psi}(\nabla\mathbf{W}_{ij},\mathbf{n}_{ij})$ is an approximation of $\mathbf{Fd}(\nabla\mathbf{W})\cdot\mathbf{n}$ at the interface γ_{ij}. To construct the flux $\mathbf{\Psi}$, we employ the physical flux, wich implies

$$\mathbf{\Psi}\left(\mathbf{W}_{ij},\mathbf{n}_{ij}\right)=\mathbf{Fd}\left(\mathbf{W}_{ij}\right)\cdot\mathbf{n}_{ij}=\left(2\mu+\frac{\tau_y}{\sqrt{\varepsilon^2+\mid D\mathbf{u}_{ij}\mid^2}}\right)\begin{pmatrix}\vec{0}\\ D\mathbf{u}_{ij}\end{pmatrix}\cdot\mathbf{n}_{ij} \tag{5.64}$$

This discretization will be complete once we build the tensor $D\mathbf{u}_{ij}=\frac{1}{2}(\nabla\mathbf{u}_{ij}+\nabla\mathbf{u}_{ij}^t)$ on the interfaces. We propose to construct the gradient of the velocity using the diamond scheme, and we have:

$$\nabla\mathbf{u}_{ij}=\begin{pmatrix}{}^t(\nabla u_{ij})\\ {}^t(\nabla v_{ij})\end{pmatrix}=\frac{1}{2|\mathcal{D}_{ij}|}\begin{pmatrix}(u_S-u_N)\,{}^tn_{LR}\,|\gamma_{LR}|+(u_j-u_i)\,{}^tn_{ij}\,|\gamma_{ij}|\\ (v_S-v_N)\,{}^tn_{LR}\,|\gamma_{LR}|+(v_j-v_i)\,{}^tn_{ij}\,|\gamma_{ij}|\end{pmatrix}, \tag{5.65}$$

where the values of $\mathbf{u}=(u,v)$ at the points S and N are represented, respectively, by the variables $\mathbf{u}_S=(u_S,v_S)$ and $\mathbf{u}_N=(u_N,v_N)$ (see Figure 4.4) and they are computed using the least squares method. The fully-discrete formulation of the equation (5.43) is given by

$$\mathbf{W}_i^{n+1}=\mathbf{W}_i^{n+1/2}+\frac{\Delta t}{|\Omega_i|}\sum_{j\in N_i}|\gamma_{ij}|\mathbf{\Psi}(\nabla\mathbf{W}_{ij}^{n+1/2},\mathbf{n}_{ij})+\Delta t\mathbf{Q}(\mathbf{W}_i^{n+1/2}) \tag{5.66}$$

5.3.3 Algorithm

In summary, below is the algorithm of the FVC-Regularization method with the local diffusion parameter α_{ij}^n for compressible Bingham flow

Algorithm 4 FVC-Regularization method for 2D compressible Bingham flow

$\mathbf{W} = (\rho, \rho u, \rho v)$;
Initialize conditions;
for each time iteration **do**
  Compute the time step Δt;
  Compute α_{ij}^n for the interface γ_{ik}
  Compute $X^c(t_n)$;
  Compute the projected solution $\mathbf{U}_{ij}^n$ on γ_{ij};
  Compute the discrete gradients $\nabla \mathbf{u}_{ij}$;
  Compute the solution $\mathbf{W}^{n+1}$;
  Update the solution: $\mathbf{W}^{n+1} \leftarrow \mathbf{W}^n$;
  Apply boundary conditions;
end for

5.3.4 Numerical results

As the approach proposed in this chapter is explicit, the time step Δt is limited by the following CFL condition

$$\Delta t = Cr \frac{1}{\sqrt{\frac{1}{\Delta t_1^2} + \frac{1}{\Delta t_2^2}}}, \tag{5.67}$$

with

$$\Delta t_1 = \min_{i,j \in I} \left(\frac{\gamma_{ij}}{\sqrt{2\alpha_{ij}^n \Lambda_{ij}^n}} \right), \qquad \Delta t_2 = \min_{i,j \in I} \left(\frac{\gamma_{ij}^2}{\max\limits_{i \in I} \left(\frac{\mu_{b,i}}{\rho_i} \right)} \right), \tag{5.68}$$

where Cr is the Courant number and $\Lambda_i = \max_k(|\lambda_i^k|)$ is the spectral radius of the barotropic Euler equations (5.42) and $\mu_{b,i} = \left(2\mu + \frac{\tau_y}{\sqrt{\varepsilon^2 + \mid D\mathbf{u}_i \mid^2}} \right)$ is the Bingham viscosity on Ω_i. This formula is inspired by a work concerning the Navier-Stokes equation [49].

5.3.4.1 Compressible isothermal Bingham flow in pipelines

In many studies, researchers often overlook the effects of compressibility, focusing primarily on incompressible flow regimes. However, in this work, we specifically address the case of weakly compressible Bingham fluids. By accounting for the impact of compressibility along with the viscoplastic behavior of the fluid, we aim to provide a more comprehensive understanding of flow dynamics, particularly in scenarios where these two factors play significant roles. This approach allows us to explore nuanced interactions between fluid compressibility and viscoplasticity, shedding light on phenomena such as plug zone formation, as is shown in Figure 5.5, in the context of weakly compressible flows.

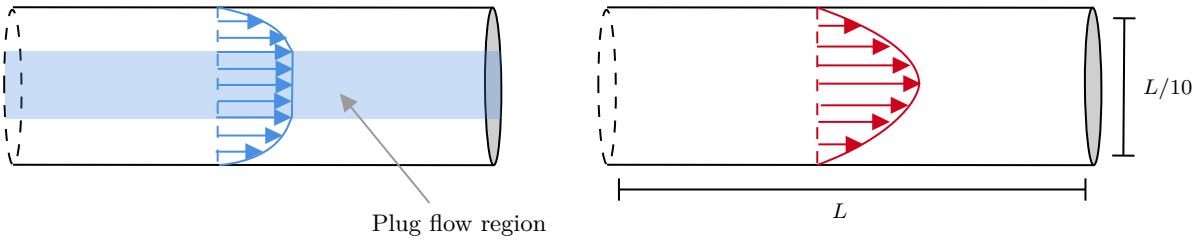

Figure 5.5: Velocity profile of a Bingham flow (left) and Newtonian flow (right).

In this work, we consider a fluid with an isothermal compressibility β constant, i.e.

$$\beta = \frac{1}{\rho}\left(\frac{\partial \rho}{\partial p}\right), \tag{5.69}$$

which gives the following equation of state:

$$p = \tilde{p} + \frac{1}{\beta}\ln\left(\frac{\rho}{\tilde{\rho}}\right), \tag{5.70}$$

where $\tilde{p}$ and $\tilde{\rho}$, are the density and the pressure at the reference state, respectively. In this section we take $\tilde{p} = 0$, $\tilde{\rho} = 1$, $L = 1$, and $\beta = 10^{-3}$. In the present study, Reynolds number Re and Bingham number Bn are used. These two numbers are defined as

$$Re = \frac{\tilde{\rho} u_r L}{\mu}, \quad \text{and} \quad Bn = \frac{\tau_y L}{\mu u_r}, \tag{5.71}$$

where u_r denotes a reference axial velocity, assumed to be equal to 1 in this section, the initial condition is defined as $(u^0, v^0, p^0) = (1, 0., \tilde{p})$. The numerical results presented in this section were calculated with a Cartesian mesh composed of 20×200 cells, and $Cr = 0.1$, and the regularization parameter ε used in 5.40 is set to 10^{-2}.

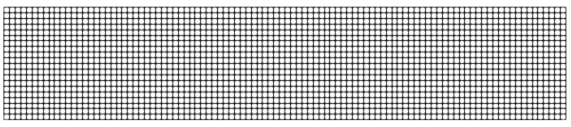

Figure 5.6: Cartesian mesh of the pipe with 4000 cells.

In Figure 5.7, axial velocity is shown for laminar Bingham flow. In the first line, the evolution of axial velocity is shown for $Bn = 0$, corresponding to a Newtonian fluid. Comparing this line with the second, where $Bn = 2.5$, we notice that the fluid behaves differently at the center of the pipeline, where velocity appears constant, indicating a plug zone. This phenomenon becomes clearer as the Bingham number increases.

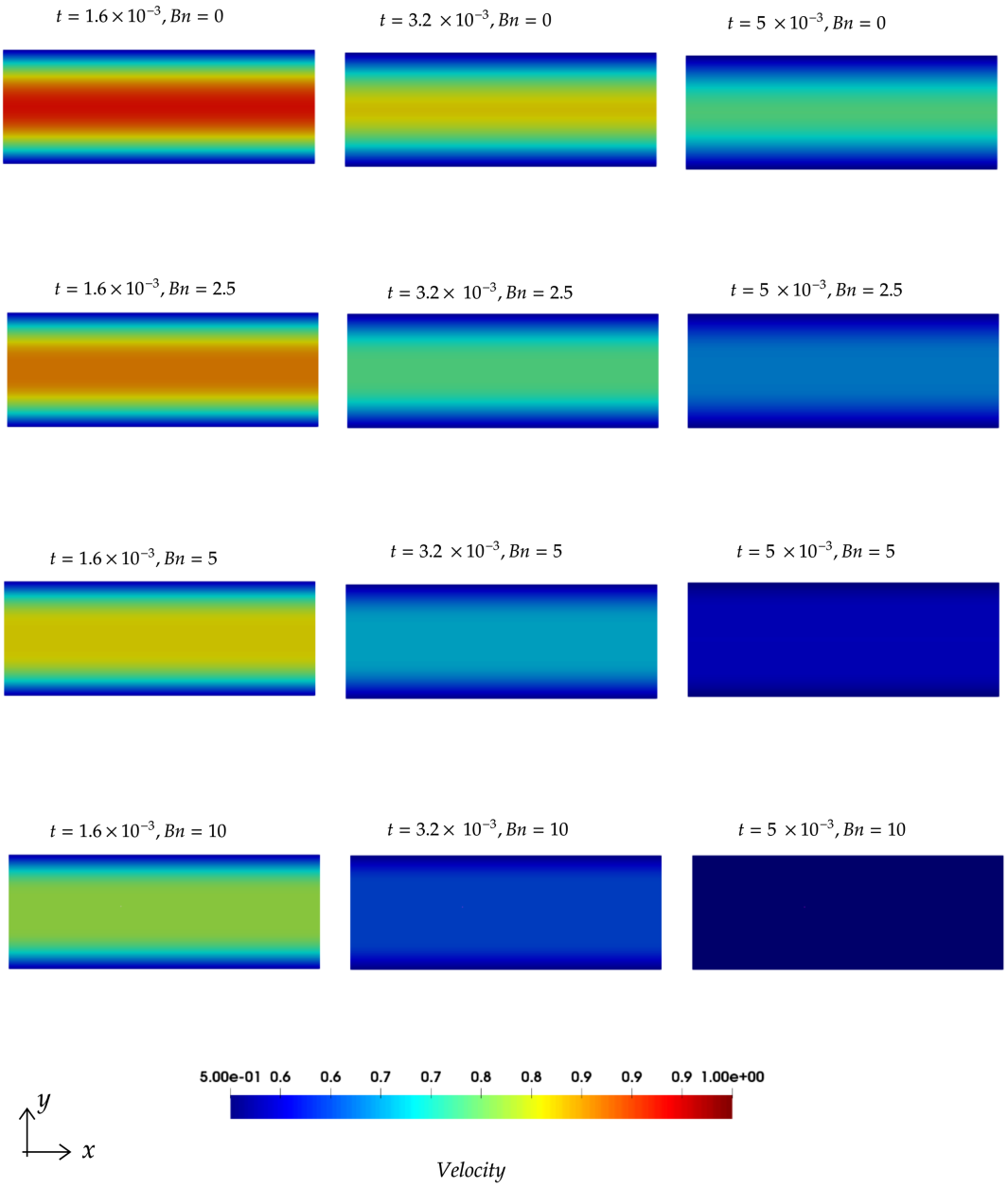

Figure 5.7: Evolution of the axial velocity u of laminar flow in a pipe with $Re = 500$ for different values of Bn.

The plug zone may be difficult to distinguish in Figure 5.7, which is why the axial velocity profile in the vertical direction is shown in Figure 5.8. In this figure, the formation of plug zones is more clearly visible and we can see that for Bingham flows, the velocity is constant at the center and behaves almost like Newtonian fluids near the pipeline wall. Moreover, the size of this zone increases with time, which is justified by the fact that shear stresses decrease with time.

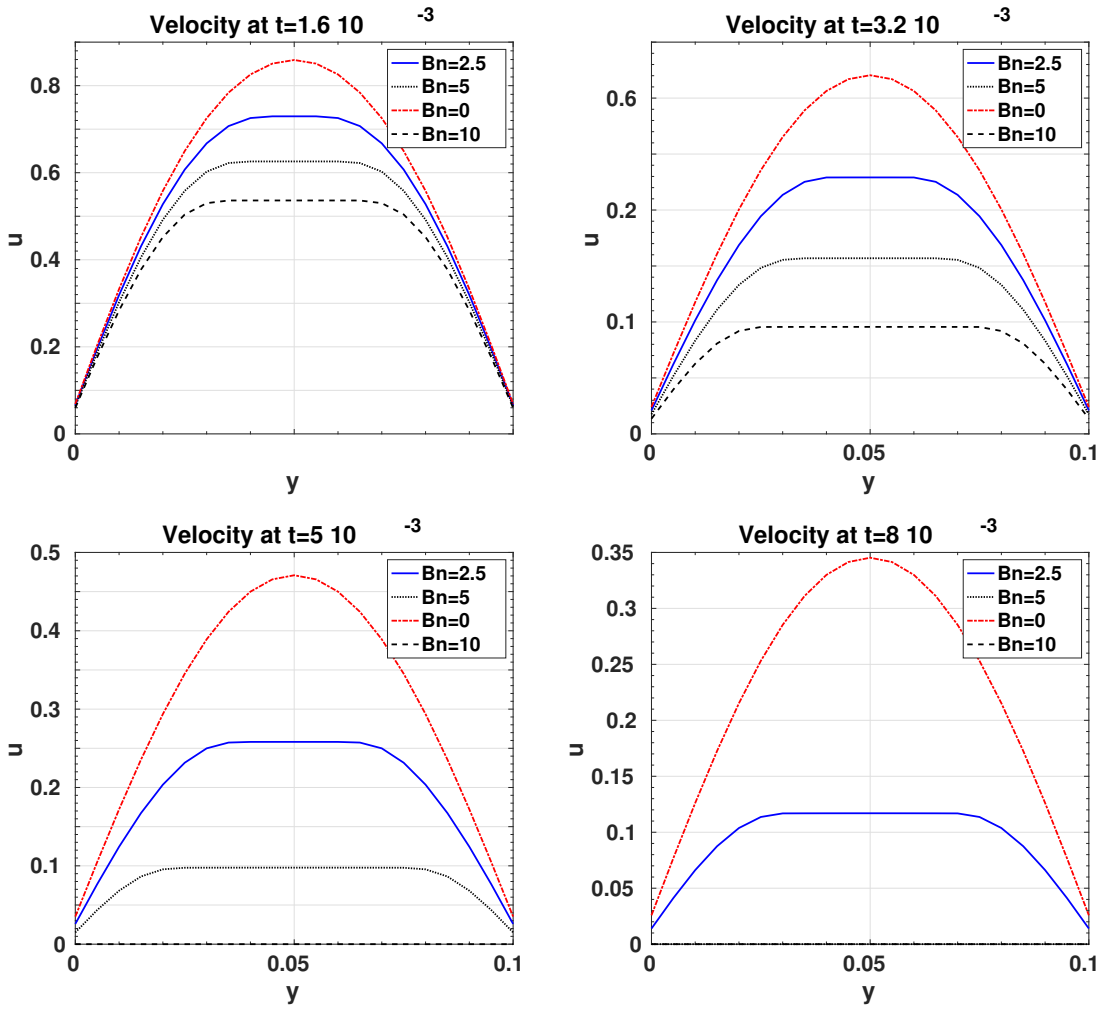

FIGURE 5.8: Axial velocity profiles calculated For $Re = 500$ at time $t = 1.6 \times 10^{-3}$ (left-top), $t = 3.2 \times 10^{-3}$ (right-top), $t = 5 \times 10^{-3}$ (left-bottom), and $t = 1.6 \times 10^{-3}$ (right-bottom).

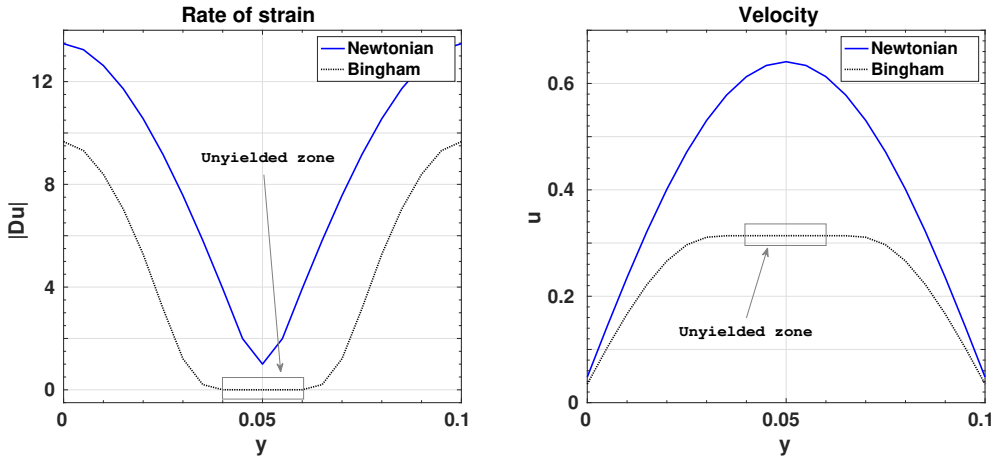

FIGURE 5.9: Shear rate $|D\mathbf{u}|$ (left) and axial velocity $u(y)$ (right) for $Bn = 2.5$ and $Bn = 0$.

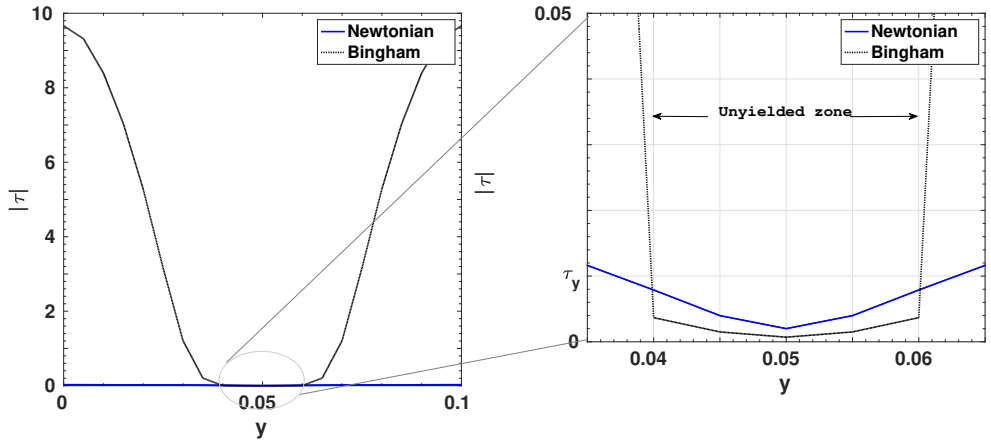

Figure 5.10: Shear stress $|\tau|$ with a zoom on the unyielded zone for $Bn = 2.5$ and $Bn = 0$.

One of the significant physical indicators to identify these plug zones, also known as unyielded zones, is the shear rate $|D\mathbf{u}|$. As mentioned in the introduction of this thesis, Bingham fluids can behave like solids. This is reflected in having a zero shear rate, even when the fluid is subjected to a non-zero shear stress. This physical behavior was obtained using our FVC approach, as shown in Figures 5.9 and 5.10. The presence of a yielded zone, where $D\mathbf{u} = 0$ and $|\tau| \leq \tau_y$, indicates that the velocity is not zero but constant. This allows us to envision a flow where the fluid behaves like a solid, moving in blocks at the center of the pipeline.

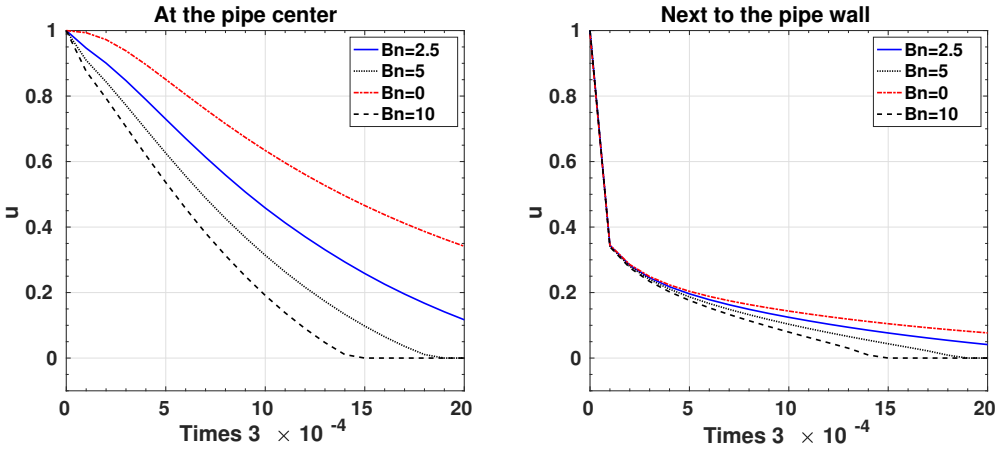

Figure 5.11: Evolution of the axial velocity u in the pipe center $y = L/20$ (left) and next to the pipe wall $y = L/100$ (right).

We now study the impact of pipe walls on the behavior of a Bingham flow. For this purpose, we present, in Figure 5.11, a comparison between the axial velocity u at the center of the pipe $y = L/20$ and next to the wall $y = L/100$. As shown in this figure, the difference between Bingham flow and Newtonian flow is most noticeable at the center of the pipeline, whereas this difference becomes smaller near the wall. This is justified by the fact that at the center of the pipeline, the shear stress is smaller than the yield stress tau_y (5.10), which gives rise to the formation of the plug zone. However, the shear stress is very large near the walls, so the

fluid behaves like a non-Newtonian liquid, and when the shear rate is very low (initially), the Bingham fluid behaves like a Newtonian liquid.

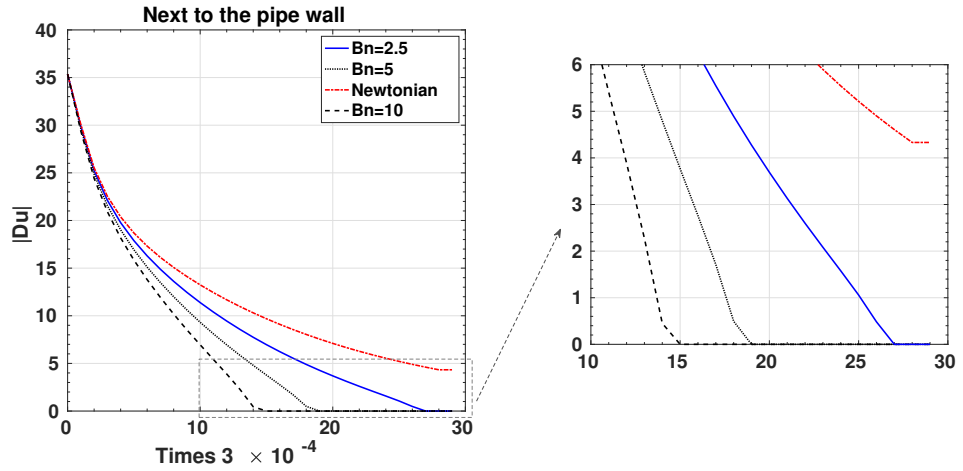

FIGURE 5.12: Evolution of the shear rate $|Du|$ next to the pipe wall $y = L/100$.

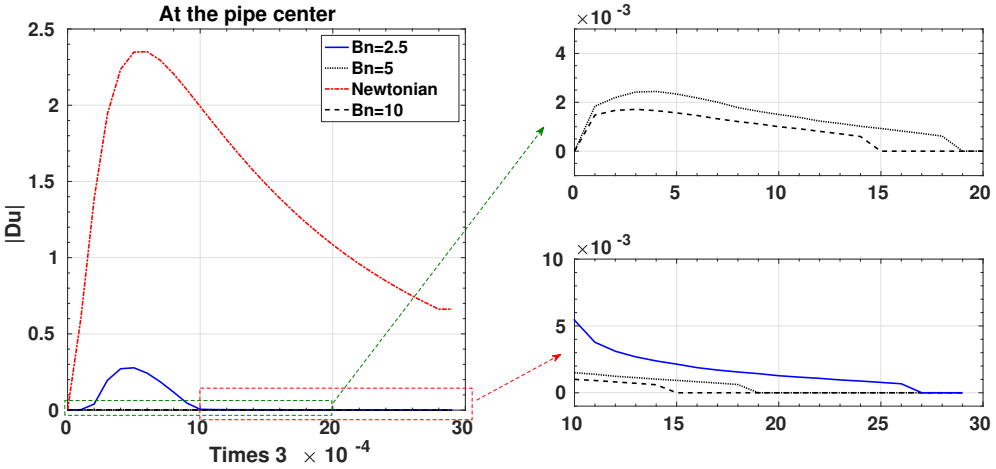

FIGURE 5.13: Evolution of the shear rate $|Du|$ in the pipe center $y = L/20$.

This test case demonstrates the capability of the FVC method to simulate the behavior of a Bingham flow with all its complexities. It also shows that plug zones are present in the case of weakly compressible model, which may be more realistic than an incompressible model.

5.3.4.2 Flow in inclined pipe

We consider a pipeline inclined by an angle θ, as shown in Figure 5.14, neglecting friction and the vertical component of the gravitational force, i.e. $\mathbf{Q}(\mathbf{W}) = (0, \rho g \sin(\theta), 0)^T$. We use a non-slip boundary conditions and $(\rho_0, \mathbf{u}_0) = (1, \mathbf{0})$.

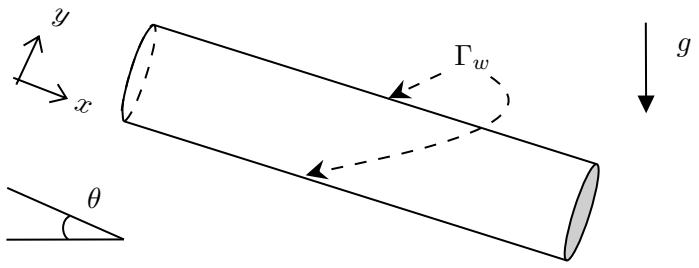

Figure 5.14: Geometry of a two-dimensional inclined pipe.

Figure 5.15 show the evolution of flow in a pipe inclined at an angle of 15 degrees. the behavior of a Bingham fluid is well illustrated by the presentation of viscosity, where it can be seen that viscosity is greater in the central region and decreases towards the walls Γ_w, where deformation rate $|D\mathbf{u}|$ is higher.

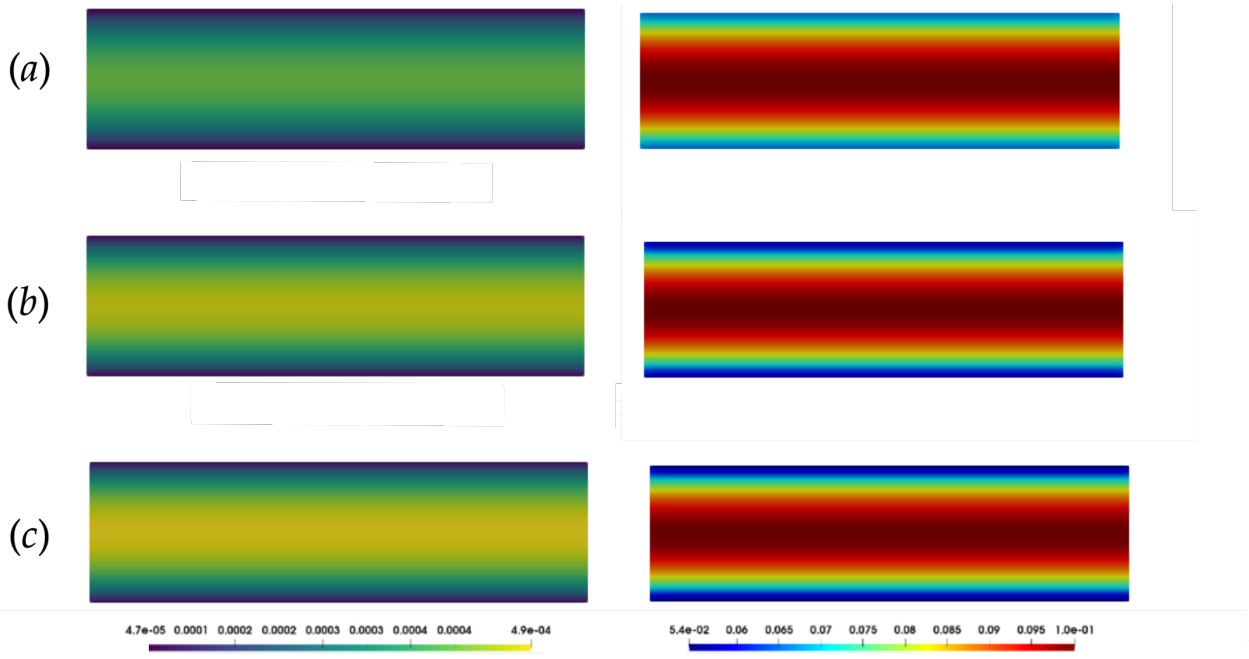

Figure 5.15: Velocity distribution $\mathbf{u}$ (left) and Bingham viscosity μ_B (right) with $\mu = 10^{-3}$, $\tau_y = 10^{-3}$ and $\theta = 15°$ at $t = 3.10^{-3}$ (a), $t = 6.10^{-3}$ (b), and $t = 9.10^{-3}$ (c).

To better visualize the results, Figure 5.16 is provided, each displaying a cross-sectional representation of velocity and viscosity along the y-direction at two distinct time points.

The final figure, Figure 5.17, showcases a comparative examination of how the velocity profile varies with changes in the yield stress. This analysis contrasts the results obtained from the one-dimensional (1D) scenario, providing a multidimensional perspective on the impact of yield stress on fluid behavior.

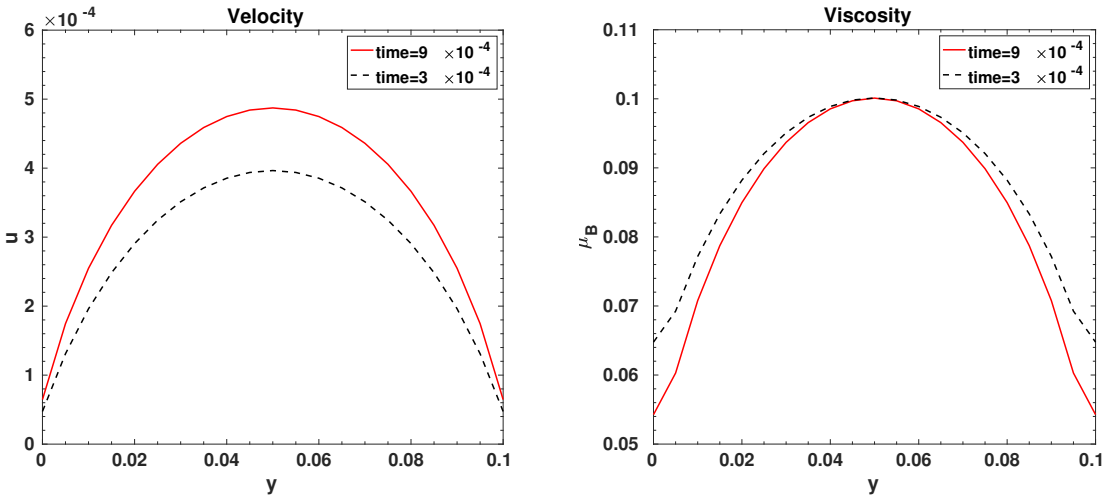

FIGURE 5.16: Cross-section of velocity distribution $\mathbf{u}$ (left) and Bingham viscosity (right) along the y-direction with $\mu = 10^{-4}$, $\tau_y = 10^{-3}$ and $\theta = 15°$.

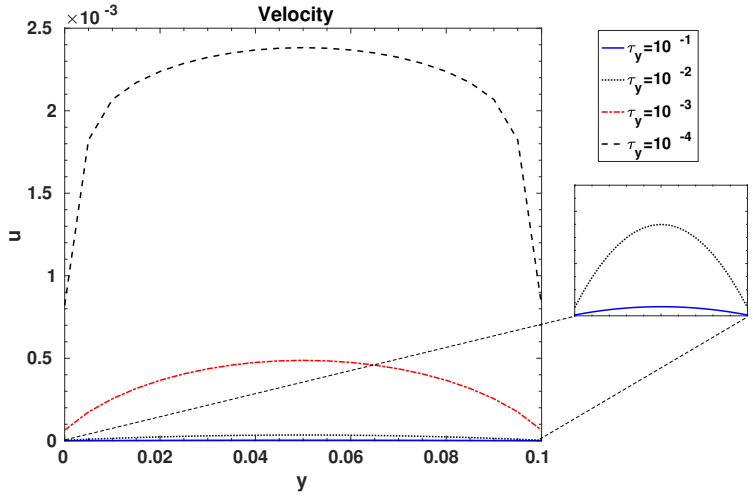

FIGURE 5.17: Cross-section of the velocity along the y-direction with $\mu = 10^{-4}$ and $\theta = 15°$ at $t = 10^{-3}$.

5.4 Conclusion

In this chapter, we have presented a splitting algorithm that addresses the challenges posed by compressible Bingham problems using the FVC method. Numerical results for the 1D case have shown that the FVC method proposed in this thesis is more accurate than the Roe scheme, and its rapidity makes it an effective approach for the numerical simulation of Bingham flows. The main result of this chapter is the simulation of the unyielded zones present in the case of 2D Bingham flow, demonstrating the solid behavior of Bingham fluids above the yield stress τ_y, and examining the impact of the wall on the behavior of a Bingham. This development is remarkable because it represents a major advance in the simulation of weak

compressible viscoplastic fluids, and opens the door to many future developments, including the comparison of compressible and incompressible cases and the application of our method to a non-isothermal model, for example, [48]. Above all, it is a very important step for us to move from an explicit solver to a semi-implicit solver, which will enable us to test more test cases without thinking about the time step which can be very small in some cases.

Chapter 6

Conclusion and perspectives

In this thesis, we have taken a comprehensive approach to studying viscoplastic fluids and achieved both theoretical advancements and numerical analysis innovations. On the theoretical side, we have demonstrated the existence of weak solutions to the incompressible Bingham Navier-Stokes equation. The numerical part of this thesis aimed to overcome the issue of numerical dissipation, which is one of the main obstacles to accurately simulating all physical phenomena. We accomplished this by developing a finite volume method with a control diffusion parameter for one and two dimensional compressible Bingham problems.

In chapter chapter 2, we constructed an approximate problem using the bi-viscosity model, which behaves like a Newtonian fluid under weak stress and like a non-Newtonian fluid when the stress rate is greater than the yield stress. After this approximation, we built a weak solution to the problem in question by passing to the limit.
The second contribution, chapter 3, of this thesis is the development of an accurate finite volume method for solving one-dimensional hyperbolic problems. The proposed method has been tested using several benchmarks; the results show the high accuracy of the method and its ability to capture contact discontinuities. Moreover, the method is fast and highly accurate. Then, in chapter 4, we have extended this approach to the two-dimensional compressible Navier-Stokes equation using the FVC-diamond strategy. In the last work on this thesis, we introduced a splitting algorithm that takes care of handling the challenges presented by the FVC method and the diamond method. The numerical results presented in this chapter confirm the effectiveness of our methodology and pave the way for its practical implementation in real industrial scenarios.

All these analytical and numerical results encourage us to continue working on these aspects, and give us good directions for future works. Some of this works are already in progress, such as the use of the FVC method to simulate incompressible flows ($Mach \leq 0.3$) using a weak compressibility approach. Another work in progress, in collaboration, aims to use a machine learning model to reduce numerical diffusion by choosing a finite volume scheme adapted to each interface. Future work also aims to combine the FVC method with the work carried out as part of the ADAPT project, which focuses on dynamic mesh adaptation.
A natural extension of this work is to generalize these numerical results, not the analytical ones, to the three-dimensional case.

List of Figures

List of Tables

List of Algorithms

Bibliography

[1] A. Aberqi, W. Aboussi, F. Benkhaldoun, J. Bennouna, and A. Bradji. Homogeneous incompressible bingham viscoplastic as a limit of bi-viscosity fluids. *Journal of Elliptic and Parabolic Equations*, 9(2):705–724, 2023.

[2] R. Abgrall. A combination of residual distribution and the active flux formulations or a new class of schemes that can combine several writings of the same hyperbolic problem: application to the 1d Euler equations. *Communications on Applied Mathematics and Computation*, pages 1–33, 2022.

[3] R. Abgrall, P. Bacigaluppi, and S. Tokareva. High-order residual distribution scheme for the time-dependent Euler equations of fluid dynamics. *Computers & Mathematics with Applications*, 78(2):274–297, 2019.

[4] W. Aboussi, M. Ziggaf, I. Kissami, and M. Boubekeur. A finite volume scheme with a diffusion control parameter on unstructured hybrid mesh: application to two-dimensional euler equations. In *International Conference on Finite Volumes for Complex Applications*, pages 3–12. Springer, 2023.

[5] W. Aboussi, M. Ziggaf, I. Kissami, and M. Boubekeur. A highly efficient finite volume method with a diffusion control parameter for hyperbolic problems. *Mathematics and Computers in Simulation*, 213:177–193, 2023.

[6] A. Ahmadi and I. Karimfazli. A quantitative evaluation of viscosity regularization in predicting transient flows of viscoplastic fluids. *Journal of Non-Newtonian Fluid Mechanics*, 287:104429, 2021.

[7] A. Al-Ghosoun, M. Herty, and M. Seaid. A new numerical treatment of moving wet/dry fronts in dam-break flows. *Journal of applied mathematics and computing*, 59(1):489–516, 2019.

[8] B. Al Taki. Well-posedness for a class of compressible non-newtonian fluids equations. *Journal of Differential Equations*, 349:138–175, 2023.

[9] M. Allouche, I. Frigaard, and G. Sona. Static wall layers in the displacement of two visco-plastic fluids in a plane channel. *Journal of Fluid Mechanics*, 424:243–277, 2000.

[10] P. Arminjon and A. Madrane. Staggered mixed finite volume/finite element method for the navier-stokes equations. *AIAA journal*, 37(12):1558–1571, 1999.

[11] E. Audusse, F. Benkhaldoun, S. Sari, M. Seaïd, and P. Tassi. A fast finite volume solver for multi-layered shallow water flows with mass exchange. *Journal of Computational Physics*, 272:23–45, 2014.

[12] T. Barth and P. Frederickson. Higher order solution of the euler equations on unstructured grids using quadratic reconstruction. In *28th aerospace sciences meeting*, page 13, 1990.

[13] I. Basov and V. Shelukhin. Nonhomogeneous incompressible bingham viscoplastic as a limit of nonlinear fluids. *Journal of non-newtonian fluid mechanics*, 142(1-3):95–103, 2007.

[14] F. Benkhaldoun. Analysis and validation of a new finite volume scheme for nonhomogeneous systems. *Finite Volumes for Complex Applications IV: Problems & Perspectives, Hermes Science Publications, R. Herbin, D. Kroner Eds*, pages 269–276, 2002.

[15] F. Benkhaldoun, S. Sari, and M. Seaid. Projection finite volume method for shallow water flows. *Mathematics and computers in simulation*, 118:87–101, 2015.

[16] F. Benkhaldoun and M. Seaïd. A simple finite volume method for the shallow water equations. *Journal of computational and applied mathematics*, 234(1):58–72, 2010.

[17] M. Bercovier and M. Engelman. A finite-element method for incompressible non-newtonian flows. *Journal of Computational Physics*, 36(3):313–326, 1980.

[18] C. Beverly and R. Tanner. Numerical analysis of three-dimensional bingham plastic flow. *Journal of non-newtonian fluid mechanics*, 42(1-2):85–115, 1992.

[19] bhqasx. 1d_Euler_exact.zip. *MATLAB Central File Exchange.*, 2022.

[20] E. C. Bingham. *Fluidity and plasticity*, volume 2. McGraw-Hill, New York, 1922.

[21] F. Boyer and P. Fabrie. *Mathematical Tools for the Study of the Incompressible Navier-Stokes Equations and Related Models*, volume 183. Springer Science & Business Media, New York, 2012.

[22] D. Breit. *Existence theory for generalized Newtonian fluids*. Academic Press, 2017.

[23] P. G. Ciarlet, R. Glowinski, and J. Xu. *Numerical Methods for Non-Newtonian Fluids: Special Volume*. Elsevier, 2010.

[24] G. Dakin, B. Després, and S. Jaouen. High-order staggered schemes for compressible hydrodynamics. weak consistency and numerical validation. *Journal of Computational Physics*, 376:339–364, 2019.

[25] G. M. De Oliveira, L. L. V. da Rocha, A. T. Franco, and C. O. Negrão. Numerical simulation of the start-up of bingham fluid flows in pipelines. *Journal of Non-Newtonian Fluid Mechanics*, 165(19-20):1114–1128, 2010.

[26] G. De Rham. *Variétés différentiables*. Hermann, Paris, 1973.

[27] P. Dreyfuss and N. Hungerbühler. Results on a navier-stokes system with applications to electrorheological fluid flow. *International Journal of Pure and Applied Mathematics*, 14(2):241–267, 2004.

[28] G. Duvaut and J. L. Lions. *Inequalities in mechanics and physics*, volume 219. Springer Science & Business Media, 2012.

[29] E. R. G. Eckert. *Survey on heat transfer at high speeds*, volume 54. Wright Air Development Center, Air Research and Development Command, United …, 1954.

[30] B. Einfeldt, C.-D. Munz, P. L. Roe, and B. Sjögreen. On Godunov-type methods near low densities. *Journal of computational physics*, 92(2):273–295, 1991.

[31] N. E. El Kadri E and A. Chillali. A finite element method for compressible and incompressible flows. *SN Applied Sciences*, 2:1–14, 2020.

[32] R. Eymard, T. Gallouët, and R. Herbin. Finite volume methods: handbook of numerical analysis. *PG Ciarlet and JL Lions (Eds)*, 2000.

[33] G. Galdi. *An introduction to the mathematical theory of the Navier-Stokes equations: Steady-state problems*. Springer Science & Business Media, 2011.

[34] P. Gilles and L. Rieusset. *The Navier Stokes Problem in the 21st Century*. Chapman and Hall/CRC, 2018.

[35] A. Harten. High resolution schemes for hyperbolic conservation laws. *Journal of computational physics*, 135(2):260–278, 1997.

[36] A. Harten, P. D. Lax, and B. v. Leer. On upstream differencing and Godunov-type schemes for hyperbolic conservation laws. *SIAM review*, 25(1):35–61, 1983.

[37] N. J. Higham. *Accuracy and stability of numerical algorithms*. SIAM, 2002.

[38] S. Hosseini, M. Manzari, and S. Hannani. A fully explicit three-step sph algorithm for simulation of non-newtonian fluid flow. *International Journal of Numerical Methods for Heat & Fluid Flow*, 2007.

[39] F. Irgens. *Rheology and non-newtonian fluids*, volume 1. Springer, 2014.

[40] H. Jasak and A. Gosman. Automatic resolution control for the finite-volume method, part 2: Adaptive mesh refinement and coarsening. *Numerical Heat Transfer: Part B: Fundamentals*, 38(3):257–271, 2000.

[41] P. Kalita, A. K. Dass, and A. Sarma. Effects of numerical diffusion on the computation of viscous supersonic flow over a flat plate. *International Journal of Applied and Computational Mathematics*, 2:663–678, 2016.

[42] S. Karni. Multicomponent flow calculations by a consistent primitive algorithm. *Journal of Computational Physics*, 112(1):31–43, 1994.

[43] J. M. Krishnan, A. P. Deshpande, and P. S. Kumar. *Rheology of complex fluids*. Springer, 2010.

[44] L. Kumar, K. Paso, and J. Sjöblom. Numerical study of flow restart in the pipeline filled with weakly compressible waxy crude oil in non-isothermal condition. *Journal of Non-Newtonian Fluid Mechanics*, 223:9–19, 2015.

[45] P. D. Lax. Weak solutions of nonlinear hyperbolic equations and their numerical computation. *Communications on pure and applied mathematics*, 7(1):159–193, 1954.

[46] P. Li and Z. Gao. Simple high order well-balanced finite difference weno schemes for the Euler equations under gravitational fields. *Journal of Computational Physics*, 437:110341, 2021.

[47] J.-L. Lions. *Quelques méthodes de résolution de problemes aux limites non linéaires*. Dunod, Paris, 1969.

[48] A. Mackay and T. Phillips. Computational modelling of compressible nonisothermal viscoelastic fluids. *Computers & Fluids*, 272:106189, 2024.

[49] C.-D. Munz. A discontinuous galerkin scheme based on a space-time expansion ii. viscous flow equations in multi dimensions. *Journal of Scientific Computing*, 34:260–286, 2008.

[50] S. Muzaferija and D. Gosman. Finite-volume CFD procedure and adaptive error control strategy for grids of arbitrary topology. *Journal of computational physics*, 138(2):766–787, 1997.

[51] D. H. Nguyen. *Analysis and approximation of compressible viscoplastic models with general nonlinearity for granular flows*. PhD thesis, Université Gustave Eiffel, 2020.

[52] G. M. Oliveira, C. O. Negrão, and A. T. Franco. Pressure transmission in bingham fluids compressed within a closed pipe. *Journal of Non-Newtonian Fluid Mechanics*, 169:121–125, 2012.

[53] T. C. Papanastasiou. Flows of materials with yield. *Journal of rheology*, 31(5):385–404, 1987.

[54] W. Prager. *Mécanique des solides isotropes au delà du domaine élastique*, volume 87. Gauthier-Villars, Paris, 1937.

[55] W. Prager. On slow visco-plastic flow. *Studies in mathematics and mechanics*, pages 208–216, 1954.

[56] J. C. Robinson and C. Pierre. Infinite-dimensional dynamical systems: An introduction to dissipative parabolic pdes and the theory of global attractors. cambridge texts in applied mathematics. *Appl. Mech. Rev.*, 56(4):B54–B55, 2003.

[57] P. L. Roe. Approximate riemann solvers, parameter vectors, and difference schemes. *Journal of computational physics*, 43(2):357–372, 1981.

[58] P. L. Roe. Characteristic-based schemes for the Euler equations. *Annual review of fluid mechanics*, 18(1):337–365, 1986.

[59] T. Roubíček. *Nonlinear partial differential equations with applications*, volume 153. Springer Science & Business Media, 2013.

[60] V. V. Rusanov. The calculation of the interaction of non-stationary shock waves with barriers. *Zhurnal Vychislitel'noi Matematiki i Matematicheskoi Fiziki*, 1(2):267–279, 1961.

[61] V. Shelukhin. Bingham viscoplastic as a limit of non-newtonian fluids. *Journal of Mathematical Fluid Mechanics*, 4(2):109–127, 2002.

[62] J. Simon. Démonstration constructive d'un théoreme de g. de rham. *CR Acad. Sci. Paris Sér. I Math*, 316(11):1167–1172, 1993.

[63] G. A. Sod. *Numerical methods in fluid dynamics: initial and initial boundary-value problems*, volume 1. Cambridge University Press, 1985.

[64] E. Toro. Primitive, conservative and adaptive schemes for hyperbolic conservation laws. In *Numerical methods for wave propagation*, pages 323–385. Springer, Dordrecht, 1998.

[65] E. F. Toro. *Riemann solvers and numerical methods for fluid dynamics: a practical introduction*. Springer Science & Business Media, New York, 2013.

[66] E. F. Toro, M. Celant, Q. Zhang, C. Contarino, N. Agarwal, A. Linninger, and L. O. Müller. Cerebrospinal fluid dynamics coupled to the global circulation in holistic setting: mathematical models, numerical methods and applications. *International Journal for Numerical Methods in Biomedical Engineering*, 38(1), 2022.

[67] E. F. Toro, A. Hidalgo, and M. Dumbser. Force schemes on unstructured meshes I: Conservative hyperbolic systems. *Journal of Computational Physics*, 228(9):3368–3389, 2009.

[68] E. F. Toro, M. Spruce, and W. Speares. Restoration of the contact surface in the hll-riemann solver. *Shock waves*, 4(1):25–34, 1994.

[69] B. van Leer and K. G. Powell. Introduction to computational fluid dynamics. *Encyclopedia of Aerospace Engineering*, 2010.

[70] Z. Wang, T. Hopfes, M. Giglmaier, and N. A. Adams. Effect of mach number on droplet aerobreakup in shear stripping regime. *Experiments in Fluids*, 61(9):1–17, 2020.

[71] M. Ziggaf, M. Boubekeur, F. Benkhaldoun, I. El Mahi, and I. Kissami. The FVC scheme on unstructured meshes for the two-dimensional shallow water equations. In *International Conference on Finite Volumes for Complex Applications*, pages 455–465. Springer, 2020.

[72] M. Ziggaf, I. Kissami, M. Boubekeur, and F. Benkhaldoun. A well-balanced FVC scheme for 2d shallow water flows on unstructured triangular meshes. *Adv. Appl. Math. Mech*, 2023.

Abstract

In this thesis, we propose a mathematical and numerical analysis of viscoplastic flows, with a particular focus on Bingham fluids. Bingham fluids, a type of viscoplastic fluid, behave like solids at low stress and like nonlinear fluids above yield stress.

The first work of this thesis is focused on the mathematical analysis of the Navier-Stokes Bingham equation. We have established the existence and uniqueness of a weak solution. In this work, we propose to build a weak solution using a bi-viscosity fluid as an approximation. In particular, we proved that the bi-viscosity tensor converges weakly to the Bingham tensor.

This thesis proposes an efficient finite volume method for simulating viscoplastic flows. Firstly, a Finite Volume Characteristic (FVC) method for one-dimensional hyperbolic systems is introduced. This method is extended to two-dimensional problems on an unstructured hybrid mesh. FVC integrates a numerical diffusion controller to better capture the various physical phenomena. The final work of the thesis concerns the simulation of compressible Bingham flows on an unstructured hybrid mesh. A splitting algorithm is proposed, integrating the FVC method for a numerical diffusion controller to accurately simulate compressible Bingham equations.

Overall, this thesis represents a significant advance in viscoplastic fluid analysis and simulation, offering valuable insights and innovative numerical approaches to the complex challenges of viscoplastic fluid dynamics.

Keywords

Incompressible Bingham fluid, Non-Newtonian fluid approximation, weak solution, Navier-Stokes equation, Bingham viscoplastic, existence of solutions, Compressible Euler equations, Method of characteristics, Finite volume method, Conservation laws, Compressible Navier Stokes equations, Weak compressible Bingham flows, Boundary layers, Flat plate, Numerical diffusion.